Molecular recognition of the plant-type Ferredoxin and Pectocin M1 through Ferredoxin uptake system (Fus)

（フェレドキシン取り込みシステムを通じた

植物型フェレドキシンおよびPectocin M1の分子認識機構）

A Doctoral Thesis

By

Nawee Jantarit

Submitted to Graduate School of Science

Osaka University

August, 2024

Molecular recognition of the plant-type Ferredoxin and Pectocin M1 through Ferredoxin uptake system (Fus)

（フェレドキシン取り込みシステムを通じた

植物型フェレドキシンおよびPectocin M1の分子認識機構）

A Doctoral Thesis

By

Nawee Jantarit

Submitted to Graduate School of Science

Osaka University

August, 2024

Acknowledgements

This study has been carried out under supervision of Professor Genji Kurisu of Institute for Protein Research, Osaka University. I would like to express my sincere gratitude to him for his invaluable guidance and support throughout my PhD thesis. His expertise and encouragement have been instrumental in shaping my research journey. I am also deeply thankful to Assoc. Prof. Hideaki Tanaka for his dedicated mentorship in the determination and refinement of X-ray crystal structures of proteins, which significantly enhanced the quality of my work.

Furthermore, I extend my appreciation to Professor Young-Ho Lee and Dr. Yuxi Lin of Korea Basic Science Institute for their collaboration and expertise in conducting ITC measurements of FusB and pectocin M1. Their contributions have enriched the scientific depth of my research. I also would like to thank Ms. Yuko Misumi for her kind suggestions regarding protein purification and crystallization.

I would like to acknowledge with deep appreciation the invaluable advice and support throughout my doctoral degree from Assist. Prof. Akihiro Kawamoto, Assist. Prof. Hiroyasu Koteishi, Assoc. Prof. Takanori Nakane, and Assoc. Prof. Jian Yu. Their mentorship and expertise have been pivotal in shaping my research and academic journey.

I am deeply grateful to Professor Atsushi Nakagawa and Professor Takayuki Kato of the Institute for Protein Research, Osaka University, for their invaluable review of my doctoral thesis and their constructive advice. Their expertise and insights have significantly strengthened the scholarly rigor and clarity of this work.

I extend my heartfelt thanks to all members of Kurisu's lab for their generous assistance and support, and warm friendships during my stay in Japan, away from my home in Thailand. In addition, I would like to express my thanks to my beloved friends and Thai seniors at Osaka University for their encouragement and support throughout my doctoral journey. Lastly, I am deeply grateful to my family for their enduring support throughout my academic journey

---

Nawee Jantarit

Department of Macromolecular Science

Graduate School of Science

Osaka University

August, 2024

Table of contents

Abbreviations

ACD	Ammonium citrate dibasic
AtFd2	*Arabidopsis thaliana* ferredoxin 2
CrFd	*Chlamydomonas reinhardtii* ferredoxin
CSP	Chemical shift perturbation
DDM	*N*-Dodecyl-β-D-maltoside
Fd	Ferredoxin
Fus	Ferredoxin uptake system
$FusB_D$	Homo-dimeric FusB
$FusB_M$	Monomeric FusB
FNR	Ferredoxin-$NADP^+$ reductase
IUTD	Intrinsically unstructured translocation domain
LDAO	*N*,*N*-Dimethyl-*n*-dodecylamine *N*-oxide
ZmFd	Zea mays ferredoxin
PAGE	polyacrylamide gel electrophoresis
PEG	Polyethylene glycol
PM	Pectocin M bacteriocins
PM1	Pectocin M1
$PM1_{full}$	Full-length PM1
$PM1_{fd}$	Ferredoxin domain of PM1
PM2	Pectocin M2
PMF	Proton motive force
SiR	Sulfite reductase
TBDR	TonB-dependent receptor

Chapter 1

Introduction

1.1 *Pectobacterium* ssp.

Pectobacterium spp. are a group of Gram-negative, plant-pathogenic bacteria belonging to the family Enterobacteriaceae[1]. Initially categorized under the genus Erwinia, *Pectobacterium* has been reclassified through phylogenetic and molecular studies[2,3]. *Pectobacterium carotovorum* ranks among the top 10 bacterial plant pathogens due to its significant destructive effects on agriculture throughout cultivation, storage, and transportation stages[2]. This leads to considerable economic losses and poses a threat to food security and sustainability by causing substantial reductions in crop yields. *Pectobacterium* spp., including species such as *P. carotovorum* and *P. atrosepticum*, are well-known plant pathogens that cause soft rot disease in numerous economically significant crops globally, such as potatoes, tomatoes, and carrots[4,5].

Soft rot disease causes significant economic losses both before and after harvest, primarily because the bacteria rapidly break down plant cell walls and extract essential nutrients from host tissues[6,7]. To achieve this, *Pectobacterium* spp. utilize a variety of virulence factors, particularly cell wall-degrading enzymes (CWDEs) like pectinases, cellulases, and proteases to degrade components of plant cell walls[4,8]. These enzymes, along with additional virulence factors, are employed to macerate host tissue and promote host cell

death, thereby providing nutrients for the pathogens[8]. The expression of CWDEs is regulated by environmental cues[5], including nutrient availability, underscoring their role in nutrient acquisition strategies under varying conditions[9]. Under conditions of nutrient deficiency, plants often experience physiological stress, which weakens their defenses against pathogens[10]. *Pectobacterium* spp. exploit these weakened defenses to invade and proliferate within plant tissues, thereby increasing disease severity[5,11].

Gram-negative bacteria, including *Pectobacterium* ssp., have developed a specialized TonB-dependent system composed of the TonB-dependent receptors (TBDR) and the Ton complexes (TonB/ExbB/ExbD). This system is responsible for recognizing and importing iron-containing molecules, such as siderophores and host iron-containing proteins, to acquire iron essential for cellular metabolism, as depicted in **Fig. 1.1**. Iron limiting conditions can also trigger the production of siderophores by *Pectobacterium* spp. [12], enhancing their ability to scavenge iron from the host environment and thereby promoting virulence[13]. Notably, *Pectobacterium* ssp. have developed specialized system for pirating and importing iron-containing proteins such as ferredoxin and ferredoxin-containing bacteriocins[14].

Effective management of soft rot disease caused by *Pectobacterium* spp. requires a multifaceted approach integrating cultural, biological, and genetic strategies. Agronomic practices that optimize nutrient availability and uptake in crops can help reduce plant susceptibility to *Pectobacterium* infection. This includes balanced fertilization practices tailored to the specific nutrient requirements of crops, which can bolster plant defenses and minimize nutrient stress in plants predisposed to infection[15]. In addition, various control methods such as copper-based pesticides[16–18], antibiotics[19] have been developed to prevent

the agricultural products from the infection of this bacteria. However, many bacterial pathogens have evolved resistance to the copper-based pesticides and bactericides[20]. Hence, there is a need for new approaches in managing bacterial diseases. Special focus has been directed toward biologically derived methods such as bacteriocins, bacteriophages, and antagonistic bacteria due to safer and environmentally friendly biological strategies, and promising methods for disease suppression by competing with *Pectobacterium* spp. for nutrients or directly inhibiting their growth[6,14,21–23]. Additionally, exploiting genetic resistance through breeding programs to develop cultivars with enhanced tolerance or resistance to *Pectobacterium* spp. is crucial for sustainable long-term disease management[5]. Nevertheless, as of now, no conclusive biocontrol strategy has been effectively applied in practical agricultural fields.

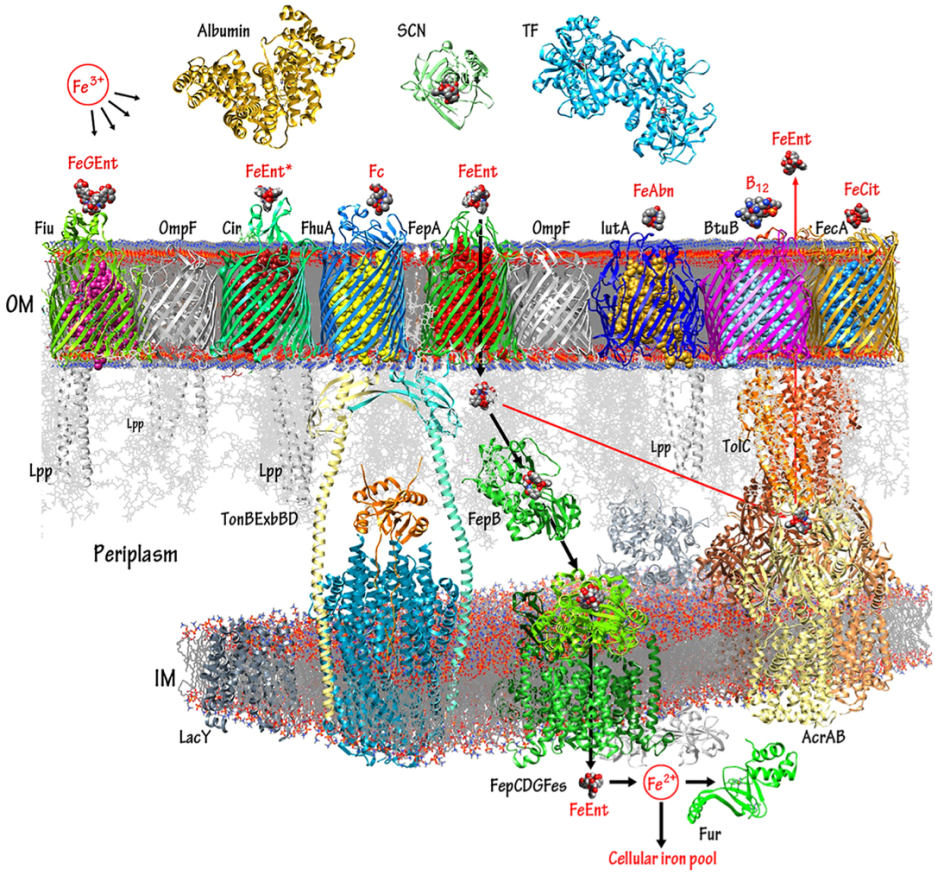

Figure 1.1 Transport of iron-containing molecules through TonB-dependent pathways in Gram-negative bacteria[24]**.** The schematic diagram of the proteins that participate in metal flux are portrayed in colors; other cell envelope components are shown in shades of gray. Bacteria and fungi secrete siderophores that chelate extracellular iron. In human and animal hosts, the innate immune system proteins albumin, SCN, and TF antagonize bacterial iron acquisition, by adsorbing siderophores, ferric siderophores, or free iron from blood, serum, lymph, and other fluids. Nevertheless, high affinity bacterial OM LGP bind specific ferric siderophores (or vitamin B_{12}) and actively transport them into the periplasm.

1.2 Ferredoxin

Ferredoxin (Fd) is a small iron-sulfur protein, roughly 10 kDa in size, with FeS clusters at its redox center, functioning as an electron carrier in various cellular redox reactions[25–27]. It is ubiquitously distributed across the domains of life, encompassing bacteria, archaea, and eukaryotes[25,26]. Ferredoxins are characterized by their iron-sulfur clusters, which are essential for their electron transfer capabilities. These clusters can vary, with the most common types being [1Fe-0S], [2Fe-2S], [3Fe-4S], and [4Fe-4S][27]. The structure of ferredoxin typically includes a polypeptide chain that coordinates the iron-sulfur cluster through cysteine residues. In cyanobacteria, algae, and higher plants, ferredoxins contain a highly conserved amino acid motif ($CX_4CX_2CX_nC$) that is crucial for the proper assembly of the [2Fe-2S] cluster, enabling the formation of the intact protein from its apo form as shown in **Fig 1.2A**[28]. This configuration allows the plant-type ferredoxin to undergo reversible oxidation and reduction, making it an efficient electron carrier[29].

It is intriguing that ferredoxin plays a central role in several cellular processes, especially given its relatively conserved structure. In photosynthesis, ferredoxin facilitates the transfer of electrons from photosystem I to ferredoxin-$NADP^+$ reductase (FNR), enabling the production of NADPH[30]. In assimilation of sulfur, sulfite reductase (SiR) catalyzes the reduction of sulfite to sulfide using electrons donated from ferredoxin[25]. Furthermore, ferredoxin involves in other fundamental metabolic processes such as, nitrogen fixation, and assimilation of hydrogen and sulfur[25,26,31]. It is fascinating to observe how ferredoxin can interact with and function alongside such a wide range of its redox partner proteins as shown in **Fig. 1.2B**. For instance, the crystal structures of ferredoxin complexes with its redox

partners, FNR[32] and SiR[33], revealed that ferredoxin presents distinct interfaces for interacting with these proteins while sharing only a few key amino acid residues in binding to them. Moreover, the energy-driven complex formation of these complexes is totally different that the FNR:Fd binding is an endothermic reaction, driven primarily by entropy[34], while the SiR:Fd binding is an exothermic reaction, driven mainly by enthalpy[35]. These differences are likely important for their enzymatic reactions[34]. In addition, despite the overall structure of ferredoxin remains highly conserved from primitive cyanobacteria to higher plants, its structural variation and overall flexibility likely facilitate interactions with each electron transfer partner[36].

Besides the functioning as electron carrier in various redox reaction in the cellular redox reactions, the under iron-limiting conditions, plant-type ferredoxins, which contain an iron-sulfur cluster, are also targeted as an iron source for the survival of phytopathogenic *Pectobacterium* ssp. To achieve this, *Pectobacterium* ssp. have evolved a specialized system for pirating iron from ferredoxin of the host through a ferredoxin uptake system, wherein a TonB-dependent receptor, coupled with the Ton complex, plays a central role in binding, importing ferredoxin, and ultimately extracting iron into these phytopathogenic bacteria[14,37,38]. The details of this system are described below.

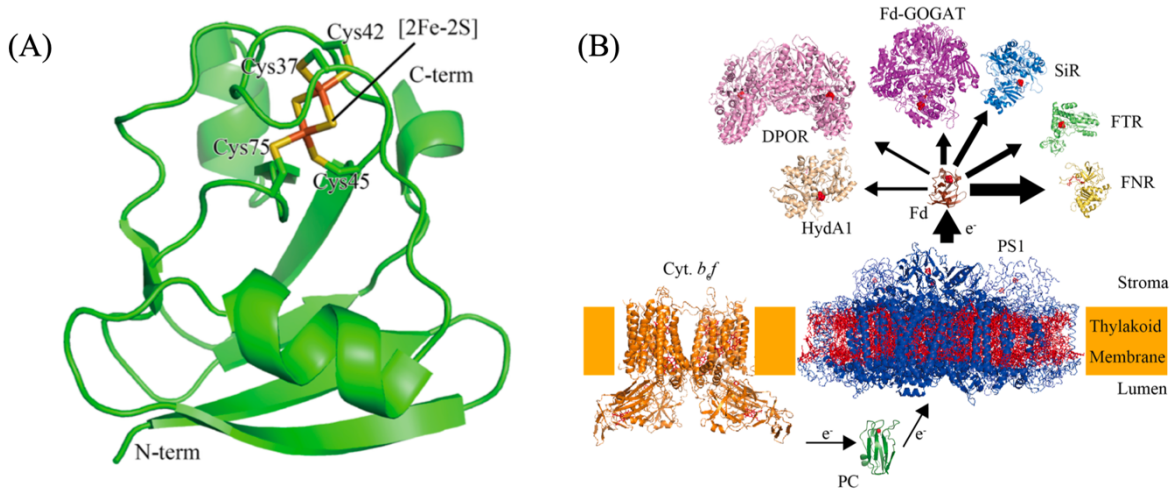

Figure 1.2 Photosynthetic Redox Enzymes around Ferredoxin[27]. **(A)** X-ray structure of plant-type Fd (PDI ID: 1WRI). **(B)** Schematic shows that photosystem I (PS1) is an integral membrane protein complex that utilizes light energy to facilitate electron transfer from plastocyanin (PC) to ferredoxin (Fd). The thickness of the arrows represents the degree of electron transfer, indicating that ferredoxin does not distribute electrons equally among these enzymes.

1.3 Ferredoxin-containing bacteriocins produced by *Pectobacterium* ssp.

Bacteriocins are antimicrobial proteins or peptides produced by both Gram-positive and Gram-negative bacteria, which are naturally resistant to their own bacteriocins[39]. A diverse and heterogeneous group of bacteriocins has been discovered, typically exhibiting narrow antimicrobial spectra to outcompete other microorganisms for limited environmental nutrients[40,41]. Within Gram-negative bacteria, the Enterobacteriaceae family, which includes *Escherichia coli* and *Pectobacterium* species, are prominent producers of bacteriocins. *E.*

coli can produce a wide range of bacteriocins known as colicins, which are categorized into two groups, group A and B, based on the translocation systems they utilize to penetrate susceptible cells[42]. Group A colicins, including A, E1 to E9, K, L, N, S4, U, and Y, are imported using the Tol system, whereas Group B colicins, including B, D, H, Ia, Ib, M, 5, and 10, are imported via the Ton system[42].

P. carotovorum produces bacteriocins called pectocin M (PMs), which aid in elimination of closely related bacteria[23]. PMs from *P. carotovorum* high growth inhibition against the closely related species *P. atrosepticum* LMG 2386[21]. Although bacteriocins possess narrow antimicrobial spectra, bacteriocin PMs, when expressed within the periplasm of *E. coli*, also exert their lethal effects by degrading lipid II, ultimately causing cell lysis[22].

PMs contain three distinct domains including an N-terminal ferredoxin-like domain and a C-terminal catalytic domain, interconnected by an α-helix as shown in **Fig. 1.3A**[21]. The architecture of these three domains was shown in **Fig.1.3B**. The ferredoxin-like domains share high sequence similarity > 60% with plant-type ferredoxin, allowing PMs to parasite TBDR FusA receptor and exploit the ferredoxin uptake system (Fus) to exert their lethal effects on susceptible cells[14]. The ferredoxin domain has the globular shape and contains the [2Fe-2S] cluster[21]. The catalytic domain adopts an elongated structure featuring a mixed α-helix/β-sheet with the most apparent structural arrangement of a half, open β-sheet formed by β6, β7, β8, and β11, aligning with the structural features commonly observed in M-class bacteriocins[21,43–45]. Divalent metal ion cofactors of Mg^{2+}, Ca^{2+}, or Mn^{2+}, are required for catalytic activity of M-class bacteriocins[22,43,45]. In recently determined crystal structures of M-class bacteriocins including PM2[21], pyocin M (PaeM)[43], and syringacin M (SyrM)[45], a

robust F_{obs}-F_{calc} electron density maps were identified near the catalytic aspartic acid residue in the active site of the catalytic domain. The electron density maps were attributed to divalent metal ion cofactors (Mg^{2+} for SyrM and Ca^{2+} for PaeM), while in PM2, a water molecule was well-fitted to the density map. PM1 adopts Mg^{2+} ion as its cofactor for degrading lipid-II precursor[22]. These indicates diverse metal cofactors for the catalytic activity among M-class bacteriocins.

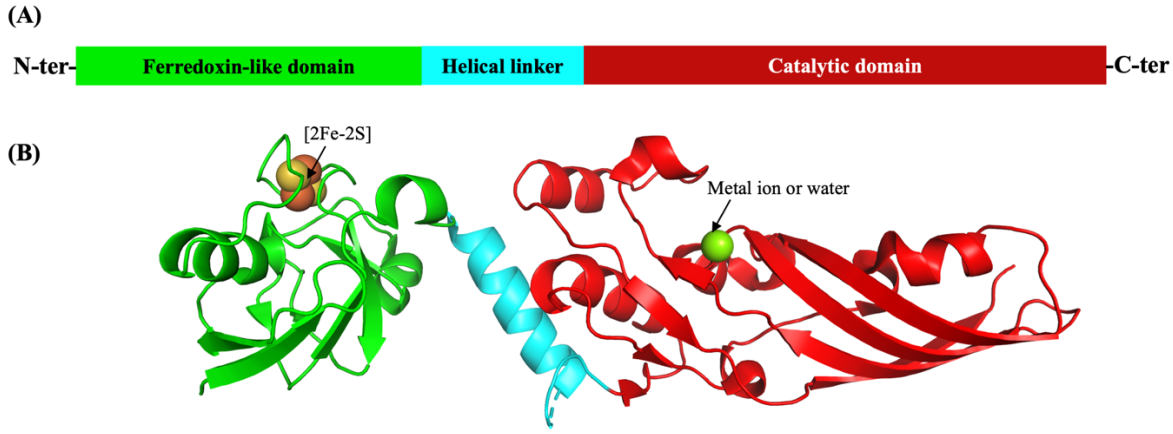

Figure 1.3 Domain arrangement and architecture of Pectocin M from *Pectobacterium* ssp. (A) Three distinct domains of pectocin M, including the ferredoxin-like domain (green), helical linker (cyan), and catalytic domain (red). **(B)** The crystal structure of pectocin M2 (PDB ID: 4n58)[21] presented as a cartoon model, with each domain colored as in **(A)**. The [2Fe-2S] cluster and cofactor were shown in sphere model.

1.4 Uptake System of ferredoxin and ferredoxin-containing bacteriocins *via* ferredoxin uptake system in *Pectobacterium* ssp.

1.4.1 Ferredoxin uptake system in *Pectobacterium* ssp.

Like other gram-negative bacteria, *Pectobacterium* ssp. possess Ton system to acquire iron by importing iron-containing molecules into the cells[12]. In iron-limiting conditions, one of iron-containing proteins targeted by this system is ferredoxin[14]. The proteins in ferredoxin uptake system (Fus) expressed by putative Fus operon in *Pectobacterium* ssp. contains four proteins including FusA, FusB, FusC, and FusD that facilitate the transport of ferredoxin from host during inflection and under iron-limiting conditions as shown **Fig. 1.4**[14,37,38]. Even though rearrangement of the genes in the operon expressing proteins in the Fus system in *Pectobacterium* ssp. compared with other bacteria is observed, these genes remain in the same cluster, suggesting a crucial role of Fus proteins in acquiring iron from small host iron-containing proteins.

The crystal structure of FusA, an outer membrane TonB-dependent receptor in Fus system of *Pectobacterium* ssp., reveals that it possesses a plug domain at the N-terminus and a C-terminal transmembrane domain consisting of 22 antiparallel β-strands, which are characteristic structure of TBDR[14]. The deletion of the gene encoding FusA resulted in a lack of ferredoxin uptake activity in *Pectobacterium* ssp., confirming the important role of FusA in importing ferredoxin within the Fus system[14]. NMR-driven docking of ferredoxin to FusA revealed that the extracellular loops and plug domain of FusA form extensive interactions with ferredoxin. These docking models suggest the conformational changes in both the

extracellular loops of FusA and the ferredoxin molecules in the productive complex, which possibly occurs upon ferredoxin binding. and import by FusA[14].

During ferredoxin uptake, deletion of the gene encoding FusB protein results in a lack of ferredoxin uptake ability in *Pectobacterium* ssp. This implies that the TonB-like FusB protein is essential for the translocation of ferredoxin across the outer membrane of susceptible bacteria, indicating that ferredoxin uptake relies on energy derived from the proton motive force (PMF) through the FusB/ExbB/ExbD machinery[37]. Normally, TonB proteins play an important role in facilitating the dislocation of plug domain of TBDR to allow the substrate across the lumen of TBDR. Recently, direct interactions of TonB proteins with atypical large substrates such as colicin M and pyocin have been reported, suggesting that bacteria may have evolved this additional function of TonB proteins to facilitate the uptake of these unusual substrates through the Ton system[42,46,47]. Similarly, FusB directly forms a stable complex with intact ferredoxin substrates[37] and the ferredoxin domains of bacteriocins. This additional function of FusB may facilitate the traversal of these proteins in their intact forms through the FusA channel. Recently, the crystal structure of FusB (PDB ID: 7zc8) has been determined as a homodimer, stabilized by intermolecular contacts of symmetric antiparallel β-strands at the N-terminus. The biological functions of dimeric and monomeric TonB have been elucidated[24,48]. The dimeric C-terminal TonB interacts with peptidoglycan and TonB-independent outer membrane receptors like OmpA, allowing its localization near the periplasmic interface of the outer membrane to locate ligand-bound receptor proteins[48,49]. However, it is evident that the homodimeric form of TonB does not bind to transporters[48,50–52]. Instead, this function is performed by the monomeric form, where

the C-terminus interacts with the TonB box sequence of TBDR to form an interprotein β-sheet through strand exchange[53–56]. These findings raise doubts about the oligomeric state of FusB in its additional function of binding to ferredoxin. Moreover, the structure-based mechanism of Fus system underlying the interaction of FusB and ferredoxin remains unknown due to lack of complex structure of FusB and ferredoxin.

FusC, belonging to the M16 family of protease, is responsible for enzymatically degrading ferredoxin in the periplasm to release iron from the [2Fe-2S] cluster. M16 proteases possess characteristic features, including a Zn^{2+}-dependence enzyme in a conserved homodimeric form, and the electrostatic-driven interactions for capturing substrates[38]. Binding to ferredoxin by FusC induces the conformational changes of FusC but remains in the elongated forms in the solution[38]. The crystal structure of the co-crystallized inactive FusC mutant and ferredoxin revealed that the active site of the homodimeric FusC for binding ferredoxin is found in the center, where two alternative binding modes of ferredoxin were found[38]. The released iron from degrading ferredoxin is then transported into cytoplasm by through ABC transporter FusD[38].

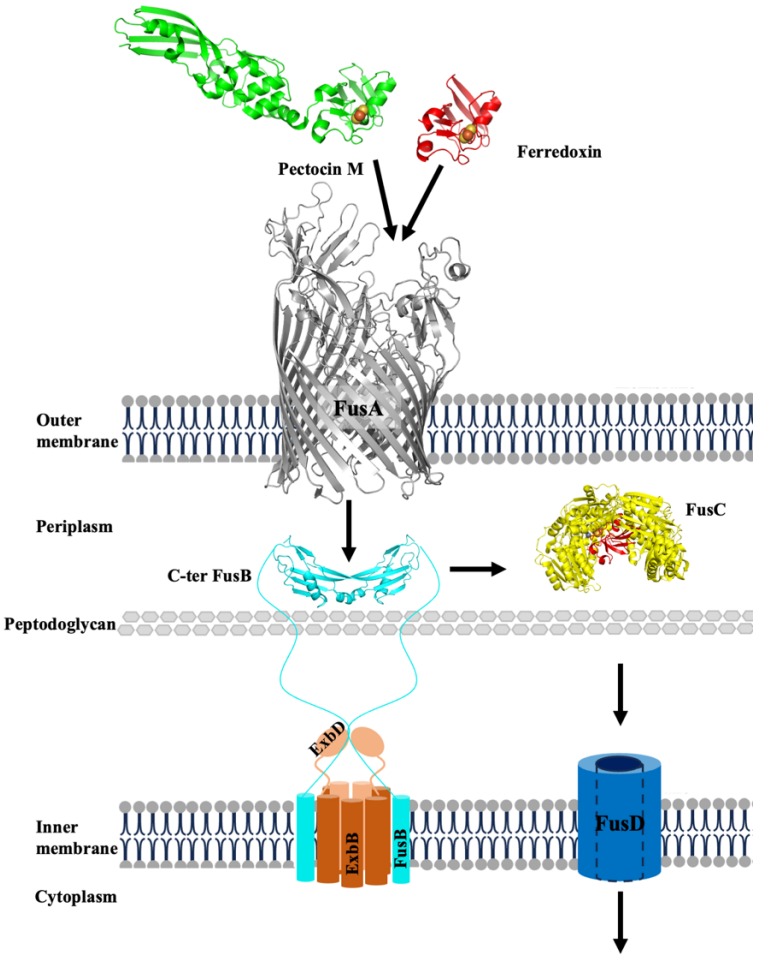

Figure 1.4 Localization of Fus proteins expressed by putative Fus operon responsible for ferredoxin uptake system in *Pectobacterium* ssp. The crystal structures of Fus proteins and their localization in the cell are schematically drawn. The crystal structures of Fus proteins, ferredoxin and pectocin M are shown as cartoon models with FusA (PDB ID: 4zgv) in grey, FusB (PDB ID: 4 in cyan, and FusC (PDB ID: 6brs) in yellow, ferredoxin (PDB ID: 4zho) in red, and pectocin M2 (PDB ID 4n58). The import pathways of ferredoxin and pectocin M are directed by the black arrows. FusD model is colored in blue. The [2Fe-2S] cluster represents in a sphere model.

1.4.2 Molecular mechanism of ferredoxin uptake *via* Fus system

Pectobacterium ssp. inhabiting iron-limiting environments have developed specialized outer membrane receptor FusA belonging to the TBDR family for facilitating the uptake of ferredoxin and pectocin M[14]. In addition to the FusA receptor, the Ton complex, including the TonB-like FusB, ExbB, and ExbD, anchored in the inner membrane, is required to provide energy transduced from the PMF necessary to facilitate ferredoxin entry into susceptible cells[37]. The next step involves the digestion of ferredoxin by the homodimeric FusC in the periplasm, resulting in release of iron from the ferredoxin[38]. This is followed by the import of iron into the cytoplasm for cellular use through FusD transporter[14].

Currently available molecular mechanism of ferredoxin uptake *via* the Fus system in *Pectobacterium ssp*. is detailed in **Fig. 1.5.** In this model, (1) in the resting state without the ferredoxin substrate, the lumen of FusA is occluded by a plug domain to prevent nonspecific substrate influx. FusB is located in the periplasmic space, where it interacts with peptidoglycan and TonB-independent outer membrane receptors, positioning itself near the periplasmic interface of the outer membrane bilayer[48,49]. This placement allows FusB to effectively locate ligand-bound receptor proteins. Once ferredoxin reaches the extracellular loops and plug domain of FusA, binding occurs on the side opposite the iron-sulfur cluster of ferredoxin[14]. (2) These interactions result in the release of the TonB box sequence from the FusA plug domain into the periplasmic space, (3) where it is then bound by FusB. (4) This binding leads to the dislocation of the plug domain into the periplasmic space, energized by PMF transduced from the ExbB/ExbD complex. Due to the comparable dimensions of the FusA lumen and the globular ferredoxin, intact ferredoxin diffusion across

the FusA lumen and into the periplasm is unlikely to occur easily[14]. However, the molecular mechanism by which ferredoxin traverses across the FusA lumen in this system remains unclear. One reliable hypothesis is that (5) the insertion of FusB into FusA lumen allows the direct interaction between FusB and ferredoxin, (6) which facilitates pulling ferredoxin through the FusA lumen into the periplasm energized by PMF produced by ExbBD complex. Ferredoxin is released in the periplasm, (7) which allow the plug domain to re-enter the FusA lumen and, (8) then return FusA and FusB to their resting states. (9)The released ferredoxin is then captured by the homo-dimeric FusC. Finally, ferredoxin is proteolytically digested by FusC to extract iron , followed by the transport of iron into the cytoplasm through FusD for cellular use.

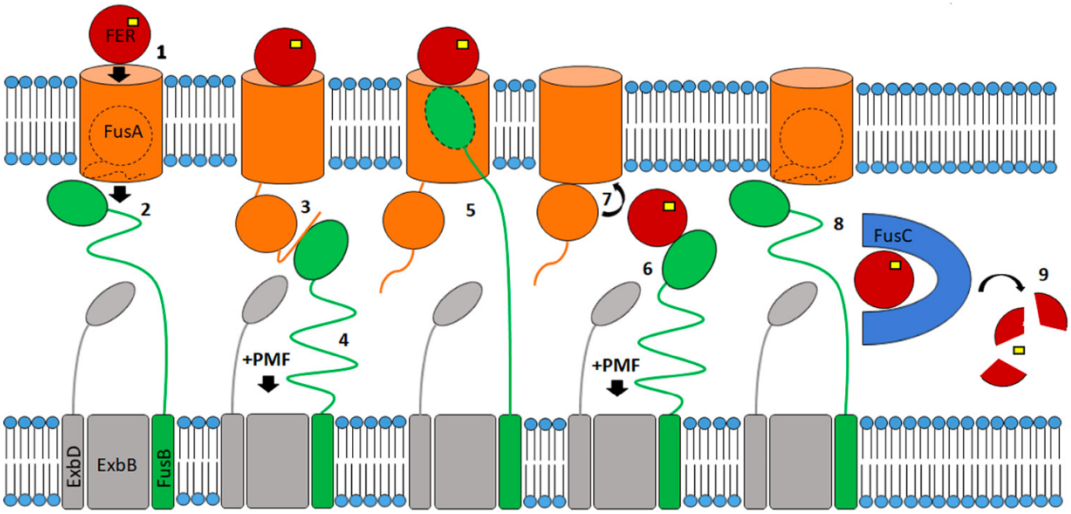

Figure 1.5 Proposed molecular mechanism of ferredoxin uptake *via* ferredoxin uptake system in *Pectobacterium* ssp.[37]. Ferredoxin is colored in red, FusA in orange, FusB in green, FusC in blue, and ExbB/ExbD complex in grey. The [2Fe-2S] cluster is shown as a yellow square.

1.4.3 Molecular mechanism of Pectocin M uptake *via* Fus system

Normally, M-class bacteriocins such as ColM, PaeM, SyrM, PyoS2 typically contain an intrinsically unstructured translocation domain (IUTD), which directly binds to the TonB, facilitating the uptake of bacteriocins through energy transduction from PMF generated by the TonB-ExbB-ExbD machinery[21,43–45,57]. In this process, the unfolding of ColM, a representative of M-class bacteriocins, is likely necessary to pass through the receptor due to its larger dimension compared to the dimension of receptor pore. Subsequently, it must undergo refolding or maturation to exert its lethal action once it reaches the periplasm[42,58]. However, PMs feature a unique adaptation: their IUTD is replaced by a plant-like ferredoxin domain, a smaller globular protein than the typical IUTD[14,21,23]. In contrast to IUTD, the ferredoxin domain is a small globular protein compared with the dimensions of the plug domain that occludes to the lumen of a TonB-dependent receptor[14,21]. This is reasonable to speculate that the receptor FusA probably allows the passage of intact PMs into the periplasm. This hypothesis gains support from the discovery that the intact ferredoxin domain is able to directly interacts with a TonB-like FusB, enabling the transport of ferredoxin into the cells by utilizing energy transduction from PMF[37]. The uptake mechanism of PMs closely resembles that of ferredoxin, with distinctions due to the additional domains of PMs. Since the overall size of PMs is obviously bigger than that of ferredoxin, conformational changes of pectocin M to be an elongated shape are crucial for reorienting its domains during the binding of ferredoxin domain to extracellular loops of FusA in initial step of its uptake[21]. This structural adjustment potentially facilitates the intact

pectocin M molecules to pass through the lumen of the TonB-dependent receptor FusA and enter the periplasm.

1.5 Selection of the methods to analyze the protein-protein interactions between FusA, FusB and PM1

To understand the biological functions and the mechanisms of protein complexes, the structural studies of these complexes are very important. Several structural biology techniques such as X-ray crystallography, cryogenic electron microscopy (Cryo-EM), Nuclear magnetic resonance (NMR) have been applied to study protein-protein interactions. Among them, each technique has both advantages and disadvantages. X-ray crystallography is a technique used to determine the atomic and molecular structure of the protein in a crystalline state, providing the high-resolution structures and detailed information on atomic positions. This technique requires high-quality crystals, which might be difficult to be obtained. Additionally, it is not suitable for protein complexes with particularly flexible and dynamic systems that are challenging to be crystallized. Cryo-EM involves flash-freezing samples of target proteins and examining them at cryogenic temperatures using an electron microscope. The technique enables the observation of specimens in their near-native state without crystallization, allowing the determination of the high-resolution structure of large and complexed biomolecular assemblies and the study of conformational changes and dynamic processes. However, there are challenges such as the use of advanced instrumentation and computational resources, limitations on the small molecular size of protein samples, and difficulties in sample vitrification. To study the atomic structures of

protein complexes more precisely, combining X-ray crystallography and Cryo-EM should be adopted to provide complementary structural insights for getting a better understanding of protein complexes. Additionally, isothermal titration calorimetry (ITC) technique is adopted to measure the heat change that occurs during molecular interactions, providing direct measurements of the binding affinity, enthalpy changes, and stoichiometry of the interaction. This technique also provides a comprehensive thermodynamic profile of interactions of protein complexes without requiring any labelling on samples. Consequently, in this research, I utilized Cryo-EM, X-ray crystallography, and ITC techniques to investigate the structures and interactions of plant-type ferredoxin and pectocin M1 with Fus proteins in the ferredoxin uptake system of *Pectobacterium* ssp. These represent a novel mechanism by which *Pectobacterium* ssp. imports ferredoxin-containing proteins into the cells in iron-limiting conditions.

1.6 Objectives of this study

In iron-limiting conditions, *Pectobacterium* ssp., a phytopathogenic bacteria causing soft rot disease in crops and ornamental plants, has evolved a range of iron uptake systems to capture iron-containing substrates, such as siderophores and host proteins, on the extracellular side and mediate energy-dependent iron transport to the periplasm. Among the iron acquisition systems, I am particularly interested in the ferredoxin uptake system of *Pectobacterium* ssp. Iron acquisition from ferredoxin utilizes the Fus protein-mediated system, consisting of four proteins: the TonB-dependent receptor FusA, TonB-like FusB, M16 protease FusC, and ABC transporter FusD. These proteins work together to import

ferredoxin from the host plant cell and extract iron for parasitic cellular use. Despite the importance in biological function and agricultural impact of this iron acquisition system, its mechanism, especially interactions of FusA and FusB to ferredoxin which facilitate the translocation of ferredoxin across the FusA lumen, has not yet been studied extensively.

Pectobacterium ssp. produce bacteriocins called pectocin M (PM), which consist of a ferredoxin domain and a catalytic domain interconnected by a helical linker. These bacteriocins help *Pectobacterium* ssp. outcompete closely related bacteria for the limiting nutrients in the environment. Possessing a ferredoxin domain that shares high sequence similarity with plant-type ferredoxin allows PM to translocate into susceptible cells *via* the ferredoxin receptor FusA, with the assistance of FusB. Once inside, PM exerts its lethal effect by degrading the peptidoglycan of the bacterial cell wall using its catalytic domain. Even the interactions of FusA and FusB and pectocin M1 have been investigated, the structure-based mechanism of PM uptake through the Fus protein-mediated Fus system remains unclear.

Although the structural understanding of ferredoxin and ferredoxin-dependent enzymes accumulated consistently, the structural information between Fus proteins and ferredoxin/PMs are less characterized. Consequently, the objectives of this study are to provide a better understanding and propose a more precise mechanism for the uptake of ferredoxin and pectocin M, focusing on the interactions of FusA and FusB with these proteins within Fus system in *Pectobacterium* ssp.

Chapter 2, to developed purification methods to yield highly pure FusA suitable for cryo-EM single-particle analysis. Additionally, to explore conditions for forming

productive complexes of purified FusA with its partner proteins, *Arabidopsis thaliana* ferredoxin 2 (AtFd2) and pectocin M1.

Chapter 3, I determined the crystal structure of PM1 using X-ray crystallography and performed HADDOCK docking of $PM1_{fd}$, as determined in this work, to FusA to present a more precise model of FusA-$PM1_{fd}$ complex, which offers insights into the mechanism of intact PM uptake into cells via the outer membrane receptor FusA in the Fus system. Although the complex models of FusA and ferredoxin have been proposed before based on NMR data of only ferredoxin domain of PM1 ($PM1_{fd}$) coupled with docking simulation with FusA. However, the crystal structure of entire PM1 was not known at that time.

Chapter 4, to understand the biological function of FusB against ferredoxin and PM1 in Fus system, I solved the crystal structure of the FusB-ferredoxin complex using X-ray crystallography, which allowed me to find the intermolecular interactions between FusB and ferredoxin. Additionally, I characterized the binding interaction profile of FusB with PM1 in aqueous solution using ITC. Combining these findings provide a better understanding of the biological function and molecular mechanism of FusB in facilitating the import of ferredoxin and PM through Fus system.

Chapter 2

Optimizing Sample Preparation Conditions for Native FusA and Its Complexes with Ferredoxins for Structural Determination by Cryo-EM

2.1 Introduction

The FusA receptor is a TonB-dependent outer membrane protein in *Pectobacterium*, playing a critical role in the ferredoxin uptake system[14]. This system enables the bacteria to acquire iron from plant ferredoxin, which is essential for their pathogenicity[59]. The FusA receptor binds ferredoxin through specialized extracellular loops, facilitating its transport into the periplasm where it is processed to release iron. The structure of native FusA at the resolution of 3.2 Å has been determined by X-ray crystallography, revealing insights into its binding mechanism and interactions with plant ferredoxins and ferredoxin domain of pectocin M1[14]. However, the complex structure between FusA and plant ferredoxin or pectocin M was not available, making it difficult to investigate the specific amino acid residues responsible for binding to its protein partners. To understand the precise mechanism and specific interactions between FusA and its partners, ferredoxin or pectocin M, it is important to determine the structure of FusA receptor at higher resolution as well as the atomic structure of the complexes between FusA and ferredoxin.

Recently, cryo-electron microscopy (Cryo-EM) has emerged as a breakthrough technique in the ongoing resolution revolution, eliminating the need for crystallization of target samples[60]. This advancement has enabled the successful structural determination of

integral membrane protein complexes without requiring crystal formation. Furthermore, Cryo-EM single-particle analysis has been developed and established for determining high-resolution structures of smaller macromolecules with low molecular weights less than 200 kDa[61]. Using Cryo-EM technique to determine the high-resolution structures of FusA and its complexes with other proteins involved in ferredoxin uptake system may provide us not only a better understanding of interactions between FusA and its protein partners in the complexes, but also insights into dynamic complex formation and more precise mechanism of these proteins in ferredoxin uptake system.

In this work, I succeed to purify FusA suitable for Cryo-EM single-particle analysis. Additionally, I explored conditions for forming productive complexes of purified FusA with its partner proteins, *Arabidopsis thaliana* ferredoxin 2 (AtFd2) and pectocin M1 (PM1), by adjusting buffer compositions, detergent types, and concentrations. Furthermore, I conducted Cryo-EM data processing of the native FusA and the FusA:PM1 complex.

2.2 Materials and methods

2.2.1 Plasmid constructs and bacterial strains

To create the plasmid for recombinant FusA production, the gene encoding FusA from *Pectobacterium atrosepticum* strain SCRI1043 was identified from its complete genome (GenBank Accession ID: BX950851). The obtained gene sequence lacking the 20 amino-acid N-terminal signal sequence was synthesized and inserted into the pET28a vector with an N-terminal His6-tag and a TEV protease cleavage sequence (Genscript, Tokyo, Japan). This recombinant plasmid was used to produce FusA protein for further structural studies.

For the AtFd2 protein, the gene sequence from *Arabidopsis thaliana* was obtained from its full genome (NCBI Reference Sequence: NP_176291). This gene was synthesized and fused into the pET28a vector without any purification tags (Genscript).

The target gene sequence encoding PM1 from *P. carotovorum* was determined from the complete genome of *P. carotovorum* subsp. *carotovorum* strain PC1 (NCBI reference: NC_012917). Initially, the gene encoding PM1 was synthesized and fused into pET28a with a His6-tagged and TEV (tobacco etch virus) protease cleavage sequence at the N terminus (Genscript). Despite optimization of expression conditions, however, no protein was expressed from the plasmid. Consequently, a new recombinant plasmid lacking any purification tags was constructed by Gibson assembly method adapted from the Gibson Assembly® Master Mix Instruction Manual (New England Biolabs, MA, USA). The polymerase chain reaction primers for amplifying the full-length PM1 gene and pET28a plasmid were shown in **Table 2.1**. The Gibson assembly reaction generated as shown in **Table 2.2** was incubated in a thermocycler at 50 for 15 minutes. The reaction tube was placed on ice and then transformed into *E. coli* (DH5α)

(Invitrogen, MA, USA). One of the colonies on the transformed LB agar plate supplemented with 50 μg/mL kanamycin was cultured in LB medium containing 50 μg/mL kanamycin for plasmid extraction. The obtained plasmid was used for PM1 production.

Table 2.1 List of primers for construction of tag-free PM1 recombinant plasmid

Primer name	Sequence (3'→ 5')	Tm ℃
pET28_forward	GCCTGTAAGGATCCGAATTCGAGCTC	55
pET28_reverse	ATAGGTCGCCATGGTATATCTCCTTCTTAAAG	53
PM1_forward	TACCATGGCGACCTATAAAATCAAGG	55
PM1_reverse	CGGATCCTTACAGGCGCTGACCTC	55

Table 2.2 Compositions of Gibson Assembly reaction

Composition	Amount
Amount of vector fragment	0.03 pmol, 1 μL
Amount of insert fragment	0.09 pmol, 1 μL
Gibson Assembly Master Mix (2X)	1X, 1 μL
Milli-Q water	-
Total volume	4 μL

2.2.2 Protein expression and purification

2.2.2.1 Preparation of native FusA

The recombinant plasmid was transformed into the *E. coli* BL21(DE3) (Invitrogen) competent cell for overexpressing FusA protein. The compositions of media used in FusA production by auto-induction are shown in **Table 2.3**[62,63]. The protocol of cell culture in this work was modified from that in the literature[14]. To culture the cell in an auto-inducing system, firstly,

the single colony of the cell was picked from the transformation plate and then, precultured in a non-inducing medium, MDG medium, with a supplement of 100 μg/mL kanamycin at 37 ℃ for 16 hours. 100 μl of the precultured medium was added to 100 mL of an auto-inducing medium, ZYM-5052 media, with a supplement of 100 μg/mL kanamycin. The cells were cultured at 30 ℃ for 36 hours to obtain an optical density at a wavelength of 600 nm (OD_{600}) about 5.5-6.5. The cell culture was centrifuged at 6000 rpm, 4 ℃ for 15 minutes.

The resultant pellet was resuspended in lysis buffer containing 50 mM Tris-HCl pH 7.9, 0.1 mg/mL lysozyme, and 1 mM PMSF. The resuspended cells were lysed by sonication (output = 3, duty = 40%, number of cycles = 4 with 5 min for sonication and 5 min for cooling). Then, the pellet was separated by centrifugation at 18,000 g, 4 ℃ for 25 minutes. The obtained pellet containing FusA was washed with a buffer containing 50 mM Tris-HCl pH 7.9, and 1.5% w/v N,N-dimethyl-n-dodecylamine N-oxide (LDAO) using a tight-fitting homogenizer for two times. The final washing step of the pellet was done with a buffer containing only 50 mM Tris-HCl pH 7.9. The obtained pellet was then denatured in a denaturing buffer containing 10 mM Tris-HCl pH 7.9, 1 mM ethylenediaminetetraacetic acid (EDTA), 8 M urea, and 5 mM dithiothreitol (DTT) using the homogenizer until well dissolved. The mixture was further incubated at 56 ℃ for 30 minutes with shaking. The incubated mixture was centrifuged at 10,000 g for 15 minutes to remove insoluble materials. The collected supernatant containing denatured FusA was then added dropwise to an equal volume of vigorously stirred refolding buffer containing 5% LDAO, 20 mM Tris-HCl pH 7.9, 1 M NaCl, and 5 mM DTT. This mixture was further rapidly stirred at 20 ℃ for 1.5 hours.

The refolded FusA solution was loaded into a dialysis bag (10 kDa MWCO: Thermo Fisher Scientific, Waltham, MA, USA) and dialyzed twice against 2.5 L of a buffer containing 20 mM

Tris-HCl (pH 7.9), 500 mM NaCl, 1 mM DTT, and various concentrations of detergents at 4 ℃ for 3 hours each time. The dialyzed solutions were then loaded into the nickel open tubular column (QIAGEN, Hilden, Germany) pre-equilibrated in the dialysis buffer. The resins were washed using 10 column volumes of the dialysis buffer with different concentrations of 20 mM, and 50 mM imidazole, respectively. The FusA protein bound to the resins was eluted using the dialysis buffer containing 250 mM imidazole. The eluted fraction was then dialyzed in the dialysis buffer with different detergent concentrations at 4 ℃ for 3 hours.

To remove the purification tag, the dialyzed samples were treated with TEV protease at a 16:1 weight ratio of FusA to TEV at 4 ℃ for 1 hour. The TEV-treated samples were then loaded onto a nickel column to remove the residual tag. The tag-free FusA in the flowthrough fractions was further purified using a HiLoad® 16/600 Superdex® 200 pg column (Cytiva, Washington, DC, USA) equilibrated with a buffer containing 20 mM Tris-HCl (pH 7.9), 300 mM NaCl, and various concentrations of detergents. The samples eluted with buffers containing 0.1% w/v DDM or 0.15% w/v LDAO were analyzed by native-PAGE. Only the samples purified with the 0.1% w/v DDM buffer were analyzed by SDS-PAGE. Finally, the fractions containing FusA were pooled and concentrated to 20 mg/mL using a 100-kDa MWCO Amicon filter (Millipore) and stored at –80 ℃ for further experiments. The completion of FusA refolding was assessed using circular dichroism (CD) spectroscopy with a J-1500 Circular Dichroism Spectrophotometer (JASCO, Tokyo, Japan). The CD spectra of refolded FusA were obtained under the following condition: 4.51 μM FusA, measured over a wavelength range of 190-260 nm for 4 scans, with a scan rate of 20 nm/min at room temperature.

Table 2.3 Compositions of media in FusA production by auto-induction

Chemicals	Medium	
	Non-inducing MDG	**Auto-inducing ZYM 5052**
Tryptone (% w/v)	-	1
Yeast extract ((% w/v)	-	0.5
Glycerol (% w/v)	-	0.5
Glucose (% w/v)	0.1	0.05
Aspartate (% w/v)	0.1	-
Lactose (% w/v)	-	0.1
$MgSO_4$ (mM)	2	2
50X M solution[a]	1X	1X
1000X trace elements[b]	0.2X	0.2X

[a] 50X M solution contains 1.25 M Na_2HPO_4, 1.25 M KH_2PO_4, 2.50 M NH_4Cl, 0.25 M Na_2SO_4

[b] 1000X trace elements contain 50 mM $FeCl_3$•$6H_2O$, 20 mM $CaCl_2$•$2H_2O$, 10 mM $MnCl_2$•$4H_2O$,10 mM $ZnSO_4$•$7H_2O$, 2 mM $CoCl_2$•$6H_2O$, 2 mM $CuCl_2$•$2H_2O$, 2 mM $NiCl_2$•$6H_2O$; 2 mM Na_2MoO_4•$2H_2O$; 2 mM Na_2SeO_3; 2 mM H_3BO_3

2.2.2.2 Preparation of AtFd2

The *E. coli* BL21(DE3) was used as the host strain for AtFd2 production. The host cell carrying the expression plasmid was cultured in LB broth containing 50 μg/mL kanamycin at 37 °C. Cell growth was periodically monitored by measuring OD_{600}. Induction of the culture was initiated at OD_{600} = 0.6 using Isopropyl β-D-1-thiogalactopyranoside (IPTG) at a final concentration of 0.5 mM, followed by continued growth at 25 °C for 18 hours. The cell pellet was collected and resuspended with 50 mM Tris-HCl pH 7.5, 50 mM NaCl, and 0.1 mM PMSF. The resuspended sample was placed on ice and stirred magnetically, and then disrupted by sonication for three times. The obtained lysate was centrifuged at 32,000 rpm, 4°C for 1 h and the supernatant was collected and stored on ice before purification by chromatography columns. The supernatant

was loaded into the Cellufine-A200 anion exchanged open column (CELLUFINE®, Tokyo, Japan) pre-equilibrated in buffer containing 50 mM Tris pH 7.5, 50 mM NaCl. The resin bound to the target protein was washed using 10 column volumes (CV) of buffers with NaCl concentrations of 50 mM, 100 mM, and 500 mM, respectively. Following that, the AtFd2 protein, identified by its distinctive red color, was eluted using a buffer containing 500 mM NaCl until the resin color remained clear. The desired fractions were loaded into a dialysis bag (7 kDa MWCO: Thermo Fisher Scientific), followed by dialysis overnight against 5 L of a buffer comprising 50 mM Tris-HCl pH 7.5, 50 mM NaCl. The dialyzed sample was applied to a pre-equilibrated 5-mL Hitrap Q HP column (Cytiva), with 50 mL of a buffer containing 50 mM Tris-HCl pH 7.5. The bound protein was eluted with a buffer containing a linear gradient of 0–1000 mM NaCl. The fractions containing AtFd2 were treated with ammonium sulfate, reaching a final concentration of 40%. The supernatant was separated by centrifugation at 6,000 rpm, 4 ℃ for 20 min and then, loaded into a Phenyl Sepharose column (GE Healthcare, Chicago, IL, USA). The target protein was eluted with elution buffer containing a linear gradient of 0-100% ammonium sulfate. The red fractions were pooled and concentrated using an Amicon Ultra-15 Centrifugal Filter Unit (10 kDa MWCO: Millipore). To check the size of AtFd2, the concentrated sample was applied into a HiLoad® 16/600 Superdex® 75 pg column (Cytiva) equilibrated in buffer containing 50 mM Tris pH 7.5, 50 mM NaCl. The samples eluted with the desired peak were analyzed using SDS-PAGE. The fractions containing AtFd2 were concentrated to 30 mg/mL using the 10 kDa MWCO Amicon (Millipore) and stored at -80 ℃ until required. The absorption feature of a 50-fold dilution solution of purified AtFd2 at the wavelength of 300-650 nm was measured using a V-630 UV-Vis Spectrophotometer (Jasco, Tokyo, Japan). The results of purification and characterization of AtFd2 will be presented in chapter 4.

2.2.2.3 Preparation of PM1

The *E. coli* BL21(DE3) pLysS was used as the host strain for PM1 production due to tight control of protein expression for expression of toxic proteins. The host cells carrying the expression plasmid was cultured in LB broth containing 50 μg/mL kanamycin and 32 μg/mL chloramphenicol. Cell growth was intermittently monitored by measuring optical density at a wavelength of 600 nm (DO_{600}). Induction of the culture was initiated at OD_{600} = 0.6 using Isopropyl β-D-1-thiogalactopyranoside (IPTG) at a final concentration of 0.5 mM, followed by continued growth at 28 ℃ for 6 hours. Following cell culture, PM1 was purified in a manner similar to the purification procedure of AtFd2 as described above. After gel filtration purification, the eluted samples were analyzed using SDS-PAGE. The fractions containing PM1 were pooled and concentrated to 20 mg/mL using the 10 kDa MWCO Amicon (Millipore) and stored at -80 ℃ until required for further experiments. The absorption feature of a 50-fold dilution solution of purified PM1 at the wavelength of 300-650 nm was determined using a V-630 UV-Vis Spectrophotometer (Jasco). The results of purification and characterization of PM1 will be presented in chapter 3.

2.2.3 Affinity chromatography of FusA on immobilized ferredoxin columns

Ferredoxins from Zea mays (ZmFd) and *Chlamydomonas reinhardtii* (CrFd) immobilized on Sepharose column were prepared in the lab, following the previously reported protocol[64]. 500 μL of 3mg/mL FusA was loaded into the immobilized Fd column pre-equilibrated with a buffer A. The loaded sample was washed with 5 CV of buffer A and then, eluted with a linear gradient of 0-100% of a buffer B. The details of each buffer in these experiments as shown in **Table 2.4** were

applied to the system to find the optimum condition for facilitating the binding of FusA to ferredoxins.

Table 2.4 List of buffer A and B used in affinity chromatography of FusA on immobilized Fd columns

System	Buffer A	Buffer B
1	50 mM sodium phosphate pH 6.9, 0.1% LDAO	Buffer A + 500 mM NaCl
2	5 mM sodium phosphate pH 6.9, 0.1% LDAO	Buffer A + 500 mM NaCl
3	50 mM Tris pH 7.9, 0.1% DDM	Buffer A + 500 mM NaCl
4	5 mM Tris pH 7.9, 0.1% DDM	Buffer A + 500 mM NaCl

2.2.4 Analytical size exclusion chromatography of protein complexes

To verify the interactions between FusA and its partners, AtFd2 and PM1, FusA was mixed with each partner at a 1:10 molar ratio of FusA to other proteins in various concentrations of DDM (0.1% or 0.005% w/v) and incubated at 4 ℃ for 1 hour. The complex formation was then analyzed by a Superdex^{TM} 200 Increase 10/300 GL column (Cytiva) equilibrated with the same buffer used for the reactions. The fractions eluted at the desired peaks were then analyzed by SDS-PAGE.

2.2.5 Negative staining electron microscopy

Negative staining electron microscopy (EM) analysis was used to evaluate the quality of the refolded FusA sample and to determine the appropriate purification conditions for cryo-EM. 3 µL of the protein sample, at a concentration about 6.5 µg/mL, was applied to continuous carbon film-coated copper grid (Nisshin EM, Tokyo, Japan), which had been glow-discharged for 10 seconds at 5 mA. The sample was stained twice with 3 µL of a 2% uranyl acetate solution, each

for 1 minute, and then rapidly blotted using Whatman filter paper number 1 (Sigma-Aldrich, MA, USA). The grid was dried at room temperature and then, visualized by an H-7650 HITACHI electron microscope at 80 kV equipped with a 1x1 K Tietz FastScan-F114 CCD camera (TVIPS, Gauting, Germany).

2.2.6 Cryogenic electron microscopy (Cryo-EM)

2.2.6.1 Data collection

Cryo-EM movies of each sample were collected under cryogenic conditions using a Titan Krios G2 (FEI, OR, USA) operated at acceleration voltage of 300 kV. The movies were recorded using a Bioquantum K3 detector (Gatan, CA, USA) in counting mode at a nominal magnification of 105,000x at the camera level, corresponding to a pixel size of 0.675 Å with 52 frames at a dose of 0.961e^-/Å^2 per frame and an exposure time of 2.63 seconds/movie resulting in a total dose of 49.97 e^-/Å^2. The datasets of native FusA and FusA:PM1 complex were collected in series within a defocus range of -1.5 μm to -0.7 μm.

2.2.6.2 Data processing and model building

Cryo-EM dataset processing was performed using RELION 3.1[65] on a GPU workstation, and the obtained models were visualized with UCSF CHIMERA[66]. In initial step, collected movies were applied to MotionCor2[67] and CTFFIND4.1[68] for correction of beam-induced motion and estimation of the contrast transfer function (CTF), respectively. A 100-micrograph subset was subjected to a TOPAZ particle autopicking[69] with a 60-pixel box size. A template-free 2D classification was performed on the extracted particles. Best 2D classes showing different orientations of samples were chosen as templates for autopicking in all micrographs. To eliminate all bad particles remaining in the dataset, successive rounds of 2D classification was performed.

After that, the remaining particles were used for *de novo* initial model building. The obtained initial model was used as a reference for 3D classification of the particles for dividing into 6 classes which resulted in further selection of particles from good classes. The 3D classification was repeated several times. However, data processing has been stopped at this stage because despite extensive efforts to enhance the resolution of the 3D structure, I encountered persistent challenges in achieving high resolution. This difficulty has made it challenging to determine the precise structural details of FusA and its complexes with PM1.

2.3 Results

2.3.1 Purification and characterization of FusA

In order to study the interaction of the outer membrane receptor FusA with AtFd2 and PM1, FusA expression vector was successfully constructed and then, overexpressed as inclusion bodies in *E. coli* BL21(DE3) competent cell. The FusA inclusion bodies were washed using LDAO detergent. The FusA pellet was denatured by dissolving in 8 M urea and then refolded using two detergents: 3% w/v LDAO or 2% w/v DDM. The refolded FusA was dialyzed using buffers containing lower concentrations of the same detergents to remove urea. The dialyzed FusA samples were then purified by nickel affinity chromatography, and size exclusion chromatography and analyzed by SDS-PAGE, and Native-PAGE. These characterization results are shown in **Fig. 2.1A**. Chromatogram profiles of purified FusA in different detergents and their concentrations show that FusA aggregation was significantly higher at lower concentrations of LDAO **(Fig. 2.1A)** and DDM **(Fig. 2.1C)** compared to higher concentrations of LDAO **(Fig. 2.1B)** and DDM **(Fig. 2.1D)**. Although higher detergent concentrations result in lower degrees of aggregation, 0.1% w/v DDM provided a clear separation between FusA aggregates and monomers. In contrast, at 0.15% w/v LDAO, the chromatographic peaks during elution exhibited overlapping between these populations, showing difficulty in isolation of desired monomeric FusA. Together with the previous results, SDS-PAGE analysis of the eluted samples in 0.1% w/v DDM **(Fig. 2.1E)** indicated that both peaks contain high-purity FusA (>95%) in different oligomeric states in solution. Native PAGE result **(Fig. 2.1F)** exhibits a single band of protein with the molecular mass between 146 kDa – 242 kDa confirming the oligomeric state of FusA as monomer with the

size about 170 kDa (100 kDa FusA + 72 kDa DDM micelle). The content of secondary structures of purified FusA, as determined by CD experiment (**Fig. 2.2**), is consistent with that calculated from the FusA crystal structure (PDB ID: 4zgv)[14]. This confirms that the purified FusA under this condition was properly refolded. Consequently, the buffer containing 0.1% DDM was adopted for FusA purification throughout this work.

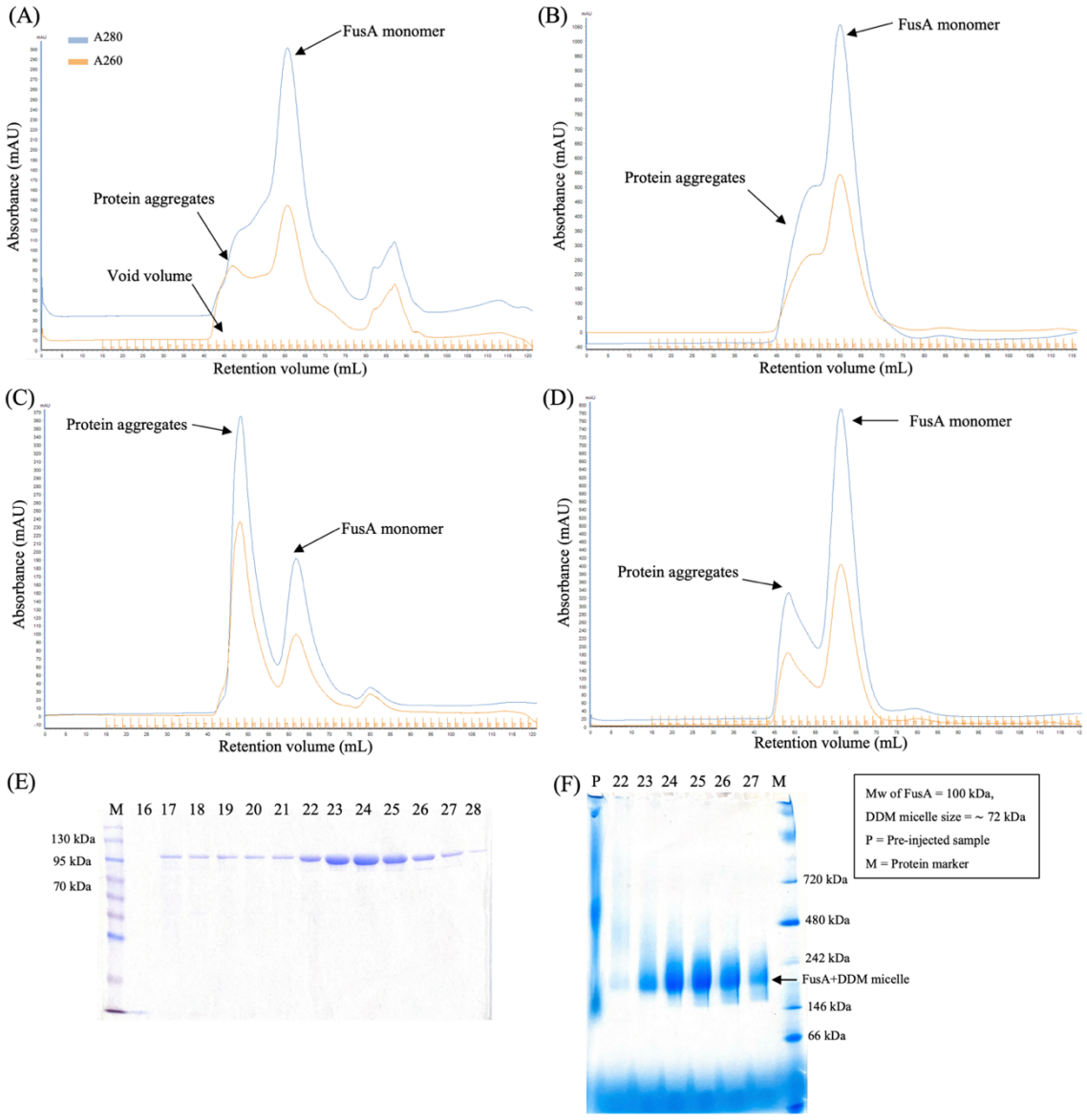

Figure 2.1 Purification and characterization of FusA in various kinds of detergents and concentrations. Superdex S200 gel filtration profiles of purified FusA in several buffer conditions including **(A)** 0.1% w/v LDAO, **(B)** 0.15% w/v LDAO, **(C)** 0.05% w/v DDM, and **(D)** 0.1% w/v DDM. **(E)** SDS-PAGE of eluted fractions from both peaks in **(D)**. **(F)** Native PAGE showing protein bands of P: pre-injected sample, and fractions 22-27 eluted from **(D)**.

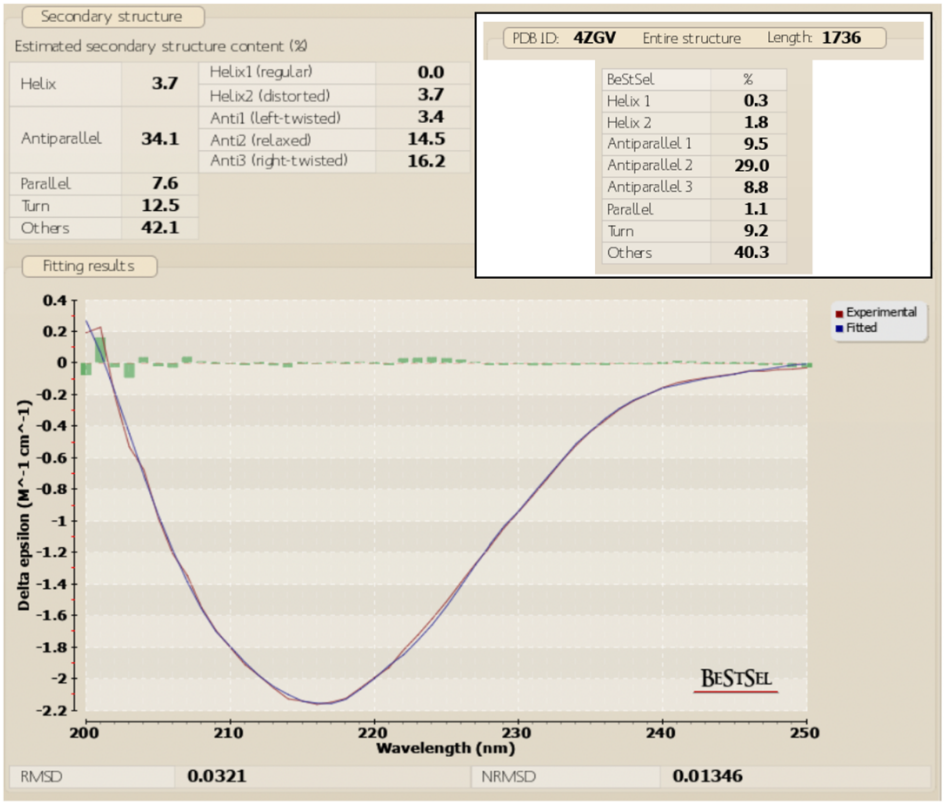

Figure 2.2 Assessment of refolding of FusA purified in buffer containing 0.1% DDM. Secondary structure determination of purified FusA based on the experimental CD spectrum using BeStSel web server[70].

2.3.2 Structure determination of native FusA and its complexes with ferredoxins

2.3.2.1 FusA

Negative stain EM was utilized to evaluate the homogeneity and quality of purified FusA preliminarily before cryo-EM data collection. The resulting images revealed a uniform distribution of monomeric FusA without any protein aggregates **(Fig. 2.3A)**. Additionally,

the FusA lumen was observable at this magnification. The same batch sample used in negative staining was also used for Cryo-EM.

A raw cryo-EM micrograph **(Fig. 2.3B)** shows well distributed dark particles, which are expected to be monomeric FusA surrounded by DDM micelles. Cryo-EM dataset of FusA was collected and then processed by RELION 3.1 software. Topaz autopicking strategy was applied for picking good particles and eliminating bad particles. The selected particles allow to generate 2D classes of this dataset as show in **Fig. 2.3C**. The obtained 2D classes revealed that the different orientations of FusA surrounded by DDM micelles were collected. The β-barrel and plug domain of FusA were clearly visible in both top and side views of the 2D classes whereas the extracellular loops appeared blurred in only some 2D classes. The particles from good 2D classes were extracted and used for initial model building as show in **Fig. 2.3D**. The FusA barrel, enveloped by DDM micelles, was distinctly visible in the generated model, although the segments potentially representing extracellular loops remained unclear. This density model was used as the reference for 3D classification of 6 classes, followed by 3D refinement. The final refined density model at resolution of 8.1 Å was obtained as shown in side- and bottom views **(Fig. 2.3E)**. At this resolution, only overall shape of protein can be visible, but the details of secondary structure and side chain information are less reliable. Despite extensive efforts in data processing to improve the resolution of 3D structure, I still suffered from low resolution of 3D model, making it difficult to determine the high resolution of 3D structure of FusA using Cryo-EM technique.

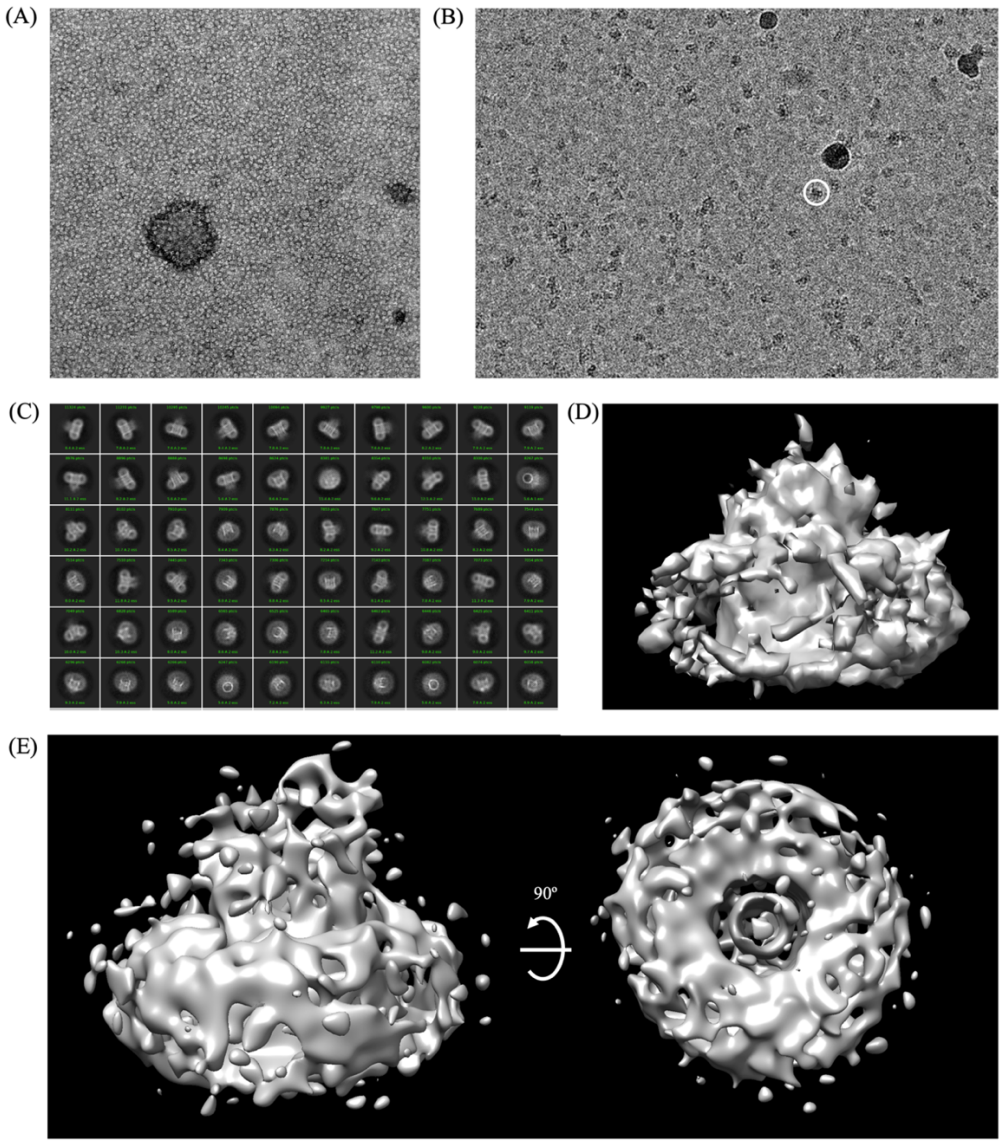

Figure 2.3 Structure determination of native FusA using electron microscopy. (A) Negative stain EM micrograph of FusA at 40,000x magnification. **(B)** An example of cryo-EM micrographs showing well-distributed dark particles, indicated by white circles. **(C)** 2D class averaging of FusA, demonstrating various orientations. **(D)** Initial model of FusA constructed from particles extracted from the good 2D classes. **(E)** The final 3D refined model at a resolution of 8.1 Å.

2.3.2.2 FusA:AtFd2 complex

I investigated the binding of FusA to ferredoxins using immobilized ferredoxin columns in different buffer systems. Two ferredoxins, CrFd and ZmFd, were immobilized onto the columns and utilized as bait to interact with FusA as the prey. The chromatograms of FusA on the CrFd column (**Fig. 2.4A-D**) showed that FusA was completely eluted at void volume during the wash step, with no FusA peak observed during the elution step, even with variations in NaCl concentrations and buffer types. So, the immobilized ZmFd column, which is the plant ferredoxin, was used for binding to FusA. However, the chromatogram of this experiment (**Fig. 2.4E**) is similar to those of the CrFd column. Additionally, another plant-type ferredoxin, AtFd2, was used in complexation reactions with FusA in buffers containing 0.1% w/v and 0.005% DDM, and then, analyzed by gel filtration chromatography, followed by SDS-PAGE. In the reaction with 0.005% DDM, peaks corresponding to FusA and the complex disappeared from the chromatogram due to the aggregation of FusA at DDM concentration lower than the CMC (result not shown). Chromatogram profile of the reaction **(Fig. 2.5A)** in 0.1% w/v DDM show two distinct peaks and SDS-PAGE result of these peak **(Fig. 2.5B)** indicates that the front peak is FusA, and another peak is AtFd2. No interaction of FusA and AtFd2 was detected in this experiment. These findings suggest that there is no strong binding between FusA and ferredoxins, and the variations in NaCl concentrations and buffer types utilized in this study do not influence nor induce the binding interaction between FusA and ferredoxins.

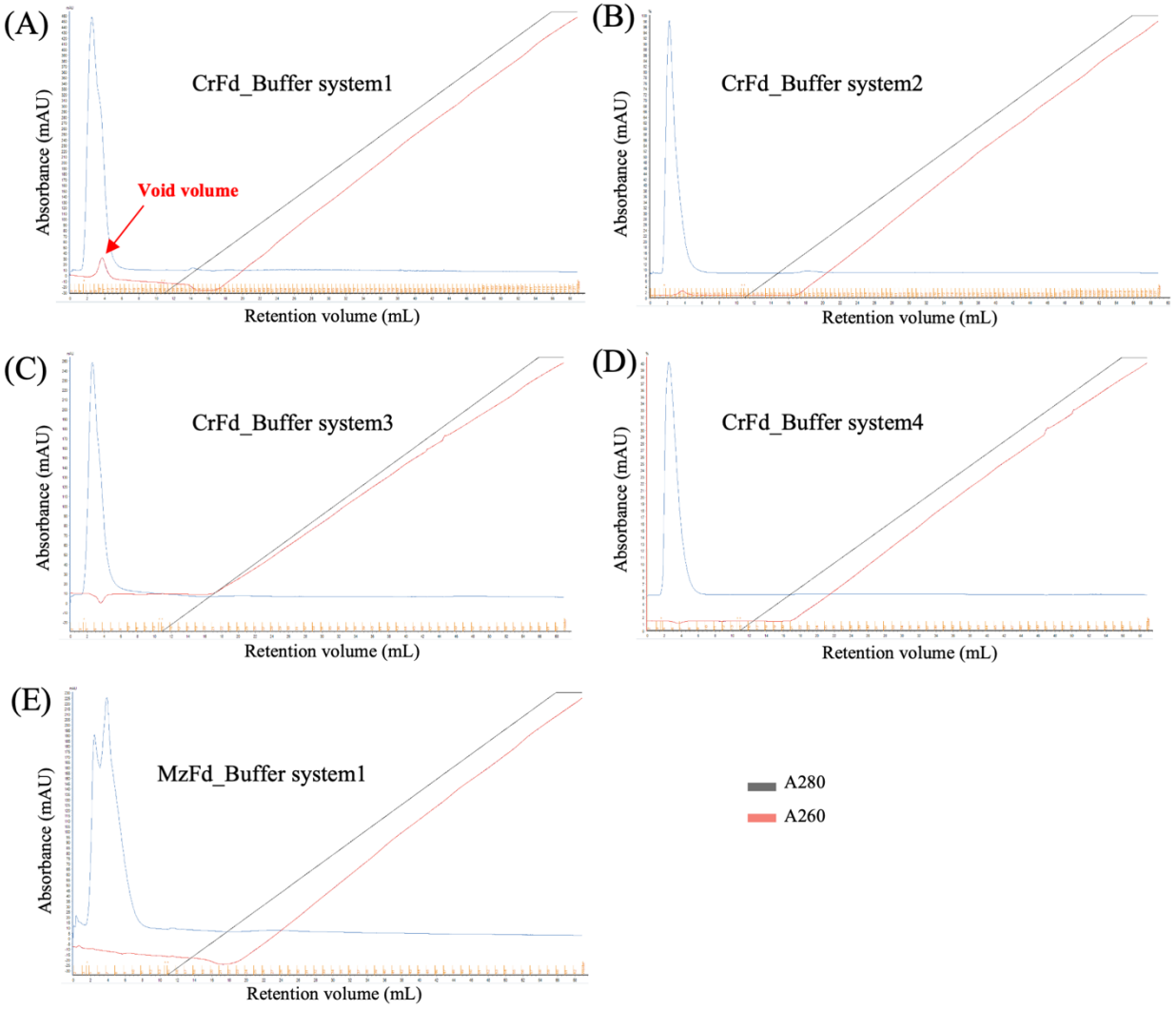

Figure 2.4 Validation of interactions of FusA with immobilized ferredoxin columns. Chromatogram profiles of FusA on immobilized CrFd column in buffers of **(A)** system 1, **(B)** system 2, **(C)** system 3, and **(D)** system 4. Chromatogram of FusA on immobilized CrFd column in buffer of **(E)** system 1.

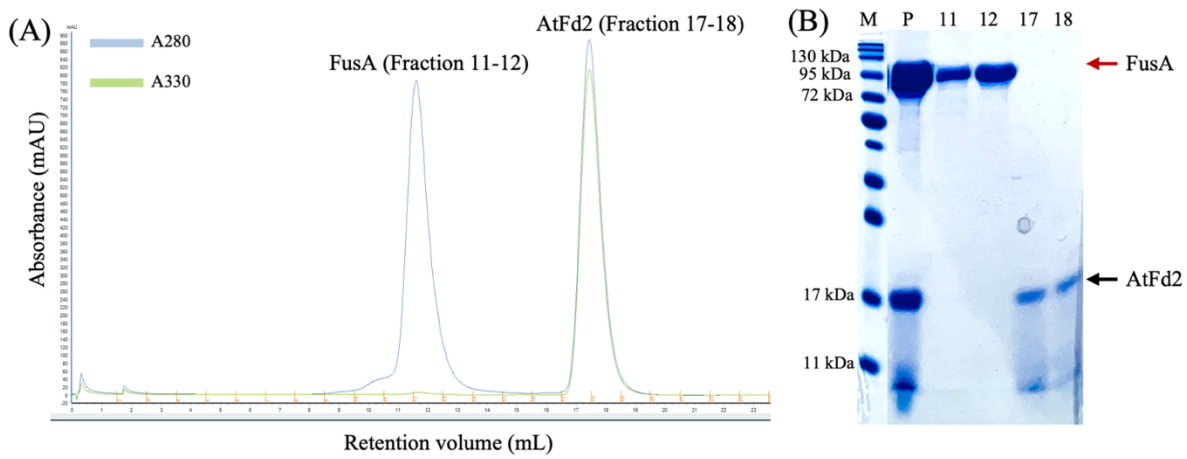

Figure 2.5 Analysis of FusA:AtFd2 complex reaction of. (A) Chromatogram profile of FusA:AtFd2 complex reaction in 0.1% w/v DDM. **(B)** SDS-PAGE result of preinjected sample (P) and the fractions corresponding to FusA (fraction 11-12) and AtFd2 (fraction 17-18) on the chromatogram in **(A)**.

2.3.2.3 FusA:PM1 complex

In a previous study, Thompson *et al*. reported that a productive complex of FusA and PM1 formed in 0.01% w/v LDAO detergent, which is below the critical micelle concentration (CMC) of LDAO (0.023% w/v). Notably, the predominant peak of FusA in the chromatogram was observed at the void volume of the analytical column. In my perspective, I suspected that FusA:PM1 complex in this work might be formed due to the aggregation of FusA and PM1 in LDAO detergent at a concentration lower than the CMC.

To validate the interaction between FusA and PM1 *in vitro* in my work, I conducted complex formation by mixing FusA with PM1 at a 1:10 molar ratio in buffers with different

DDM concentrations: 0.1% w/v and 0.005% w/v. These concentrations match those used in FusA purification and are lower than the critical micelle concentration (CMC) of DDM (0.0087% w/v), respectively. I also conducted analytical SEC experiments of individual FusA and PM1 in these DDM concentrations, as shown in **Fig. 2.6A-D**. The chromatogram of FusA **(Fig. 2.6A)** shows a monodisperse peak of the FusA monomer in 0.1% w/v DDM, whereas no peak is observed in the chromatogram of FusA in 0.005% w/v DDM **(Fig. 2.6B)** because FusA aggregates could not pass through a 0.22 μm filter during sample injection. PM1 in 0.1% w/v DDM showed several overlapping peaks in the chromatogram **(Fig. 2.6C)**, particularly a peak eluting at the same position as FusA, making it difficult to analyze the productive complex at this DDM concentration. This finding suggests that PM1 molecules are possibly to occupy or interact with DDM micelles. On the other hand, the chromatogram of PM1 in 0.005% w/v DDM **(Fig. 2.6D)** clearly showed the presence of single peak of PM1. Consequently, I analyzed the FusA:PM1 complex in 0.005% w/v DDM using analytical SEC and SDS-PAGE **(Fig. 2.6E)**. Surprisingly, the SDS-PAGE result of overlapping peaks eluted in fractions 11-12 clearly showed the presence of both FusA and PM1 bands, suggesting that FusA is stabilized by PM1, possibly through the formation of a productive complex. Furthermore, the chromatogram profile and SDS-PAGE result of the reinjection of fraction 11-12 **(Fig. 2.6F)** were similar to those of the starting reaction, suggesting the formation of stable FusA:PM1 complex in FusA:PM1. The obtained FusA:PM1 complex was further used for structure determination by Cryo-EM.

The homogeneity and quality of the FusA complex were assessed using negative stain EM. A well-distributed array of white particles was observed in the obtained image

(Fig. 2.7A). Some protein oligomerations or aggregates were clearly visible. Nevertheless, I proceeded to the next step by collecting a cryo-EM dataset of the FusA complexed with PM1 using the same batch sample as in the negative stain EM. An example of cryo-EM micrographs is shown in **Fig. 2.7B**. The obtained dataset was processed in the similar way to that of native FusA as described above. 2D classification of FusA:PM1 complex revealed the different orientations of FusA. The top views of FusA were clearly visible in several 2D classes, while the side views appeared as blurry particles, likely due to the partial collapse of the FusA structure at the low DDM concentration. This resulted in heterogeneity within the FusA:PM1 complex. Even with extensive attempts at particle picking to determine optimal conditions for 2D classification, the data processing remained problematic due to poor 2D classification. This resulted in the failure to construct an initial model, hindering progress to subsequent steps.

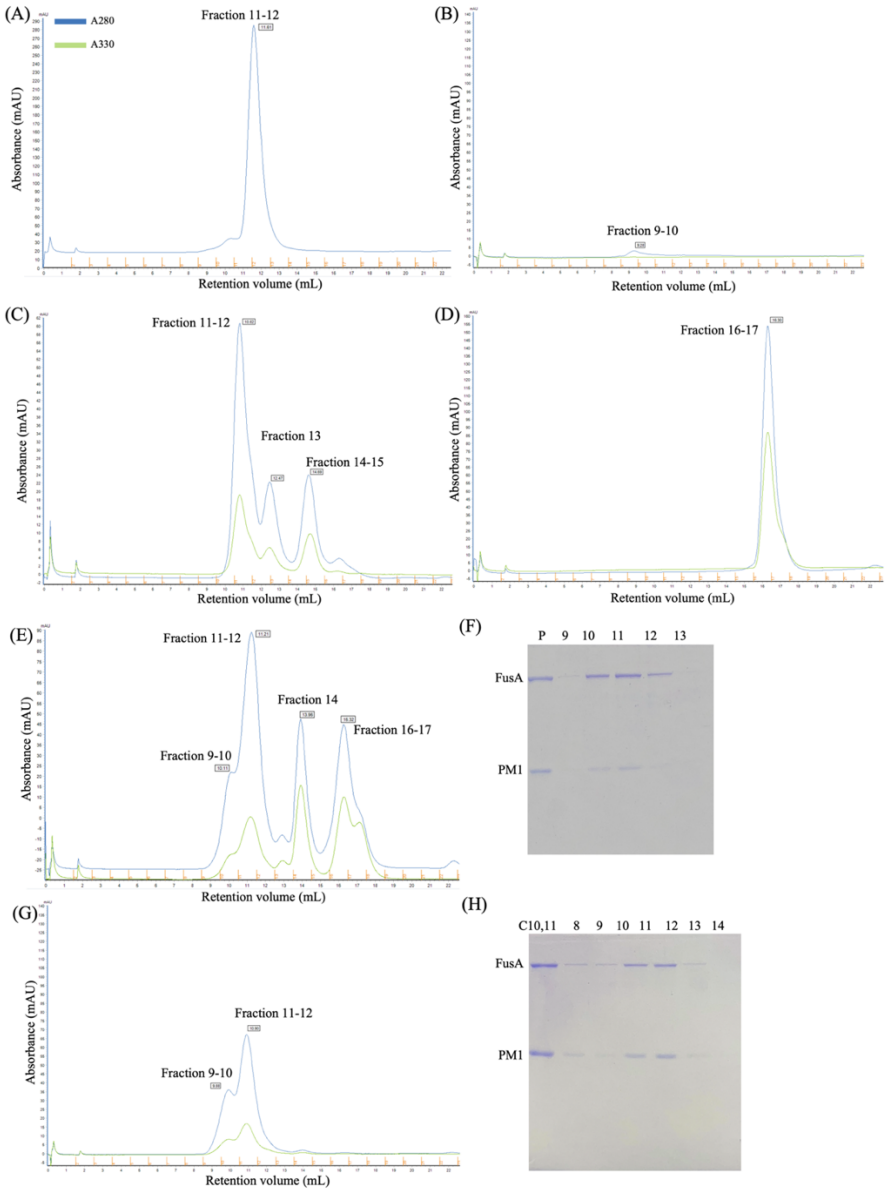

Figure 2.6 Size exclusion chromatography and SDS-PAGE revealing formation of stable complex of FusA:PM1. Chromatogram profiles of FusA in buffers containing DDM concentrations of 0.1% w/v **(A)** and 0.005% w/v **(B)**. Chromatogram profiles of PM1 in buffers containing DDM concentrations of 0.1% w/v **(C)** and 0.005% w/v **(D)**. Chromatogram profile and SDS-PAGE result of **(E)** the complex reaction of FusA:PM1 and **(F)** the reinjected sample from fractions 11-12 of **(E)** in a 0.005% w/v DDM buffer.

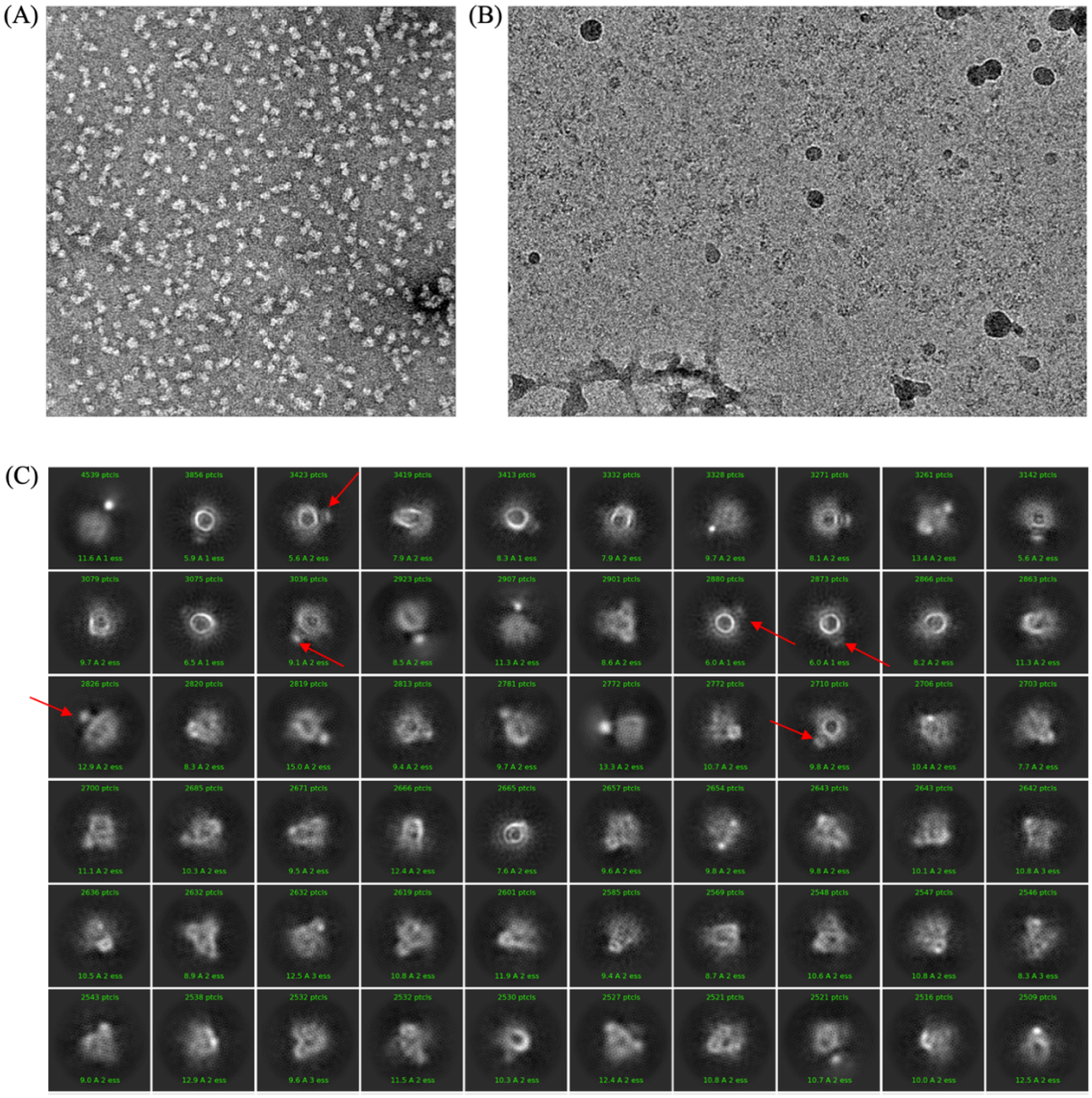

Figure 2.7 Structure determination of FusA:PM1 using electron microscopy. (A) Negative stain EM micrograph of FusA:PM1 at 60,000x magnification. **(B)** An example of cryo-EM micrographs of FusA:PM1 sample. **(C)** 2D classification of FusA:PM1, demonstrating various orientations of FusA and potential particles of PM1, indicated by red arrows.

2.4 Discussion

In this work, the comprehensive purification and characterization of FusA laid the foundation for subsequent structural analyses and interaction studies. Through several purification steps of FusA inclusion bodies involving detergent washing, urea denaturation, refolding, and chromatographic purification, we obtained highly pure monomeric FusA solubilized in the buffer containing 0.1% DDM suitable for further structural studies. Furthermore, the content of secondary structures in our purified FusA samples, as determined by CD, consistent with that of the FusA crystal structure, affirming successful refolding under the specified condition in this study.

Despite these advancements in purification and characterization, structural elucidation via Cryo-EM encountered challenges, particularly in achieving high-resolution 3D reconstructions. While negative stain EM provided preliminary insights into the homogeneity and quality of the purified FusA, Cryo-EM analysis yielded only moderate resolution structures about 8.5 Å. The obtained Cryo-EM data, though informative, fell short of resolving finer details such as secondary structure elements and side chain conformations due to limitations in resolution. Efforts to refine the Cryo-EM data and improve resolution proved challenging, underscoring the need for innovative approaches or complementary techniques to overcome these limitations in future studies.

The investigation into FusA complexes with ferredoxins, namely CrFd and ZmFd, yielded intriguing findings. Contrary to expectations, immobilized ferredoxin columns could not be utilized to detect binding interactions with FusA, suggesting a lack of affinity or a complex formation with lower affinity under the tested conditions in this study. Similarly, gel

filtration chromatography coupled with SDS-PAGE analysis of complex reaction of FusA:AtFd2 did not reveal significant interaction between FusA and AtFd2. These results challenge previous assumptions regarding FusA-ferredoxin interactions and underscore the complexity of protein-protein interactions in biological systems. These findings are consistent with the previously reported results in the literature that FusA slowly interacts to AtFd2 in *in vitro*[14]. In the affinity chromatography experiments with FusA and immobilized Fd columns, FusA could only transiently access and interact with the immobilized ferredoxin molecules, making it difficult to form stable complexes with the ferredoxins. Even with an incubation time of 1 hour for the FusA:AtFd2 reaction, productive complex formation was not achieved. It is evident that FusA requires a longer time to weakly interact with ferredoxins. Therefore, further investigation is needed to determine the appropriate conditions for forming productive complexes.

In the buffer containing DDM at a concentration higher than the CMC, the complex formations of FusA:PM1 suffered from randomly self-aggregated PM1, which hindered PM1 from accessing FusA. In contrast, the complex formation of FusA in a low concentration of DDM detergent, 0.005% w/v showed promising results. Through analytical size exclusion chromatography coupled with SDS-PAGE analysis, we observed the formation of a stable FusA complex in both the initial and reinjected samples, suggesting that PM1 potentially stabilizes the folding of FusA at DDM concentrations lower than the CMC with its interaction. The formation of the FusA:PM1 productive complex in a buffer containing LDAO at concentrations lower than the CMC was also reported[71]. These findings are consistent with my result above and with literature indicating that FusA interacts with PM1

faster than with AtFd2[14]. Despite encountering challenges in Cryo-EM data processing, preliminary analyses indicated the potential presence of PM1 molecules in 2D classes of the productive FusA:PM1 complex, making it a promising candidate for further investigation to elucidate its structural details in the conditions provided in this study, although further optimization is needed.

In summary, this study in chapter 2 successfully developed a purification and characterization protocol for FusA, achieving highly pure monomeric FusA samples suitable for structural studies. Despite the challenges in obtaining high-resolution 3D structures via Cryo-EM remain, preliminary data indicated moderate resolution. Investigations into FusA complexed with ferredoxins showed no significant interactions, while the FusA:PM1 complex demonstrated promising stability under the concentrations of DDM lower than its CMC. These findings suggest that further research efforts in optimization is needed to overcome these hurdles and advance the better understanding on structural details and interactions of FusA and its partner proteins in ferredoxin through the ferredoxin uptake system.

Chapter 3

Crystal Structure of Pectocin M1 Reveals Diverse Conformations and Interactions during Its Initial Step Via the Ferredoxin Uptake System

3.1 Introduction

In general, M-class bacteriocins including colicin M possess an N-terminal intrinsically unstructured translocation domain (IUTD)[43,45,58] that directly binds to TonB. However, PM1 and PM2 do not have an IUTD domain, but instead contain a globular plant-type ferredoxin domain at the N-terminus[14,21,23] as shown in **Fig. 1.3**. Studies have shown that the TonB-dependent receptor FusA in the ferredoxin uptake system of *Pectobacterium* ssp. is used for translocation of pectocin M (PMs) into cells[14,71]. Relative to the IUTD, plant-type ferredoxin is smaller than the plug domain of FusA that occludes the FusA lumen; thus, it can directly interact with the TonB-like protein FusB, allowing its transport into cells via the TonB-ExbB-ExbD machinery[37]. Differing from plant-type ferredoxin, the dimensions of reported PM2 structures are larger than the FusA plug domain[21]. Consequently, PMs must undergo essential conformational changes to reorient their domains into an extended conformation, enabling them to traverse the lumen of the receptor FusA and enter the periplasm intact. Interactions between the ferredoxin domain of PM1 and FusA extracellular loops have been investigated by NMR[14,71] and site-directed mutagenesis[71]; however, the mechanism underlying PM uptake into target cells *via* the ferredoxin uptake system, especially the initial step of import, remains unclear due to the lack of an atomic resolution structure of full-length PM1.

In Chapter 2, the productive complex of FusA and PM1 in a buffer containing 0.005% DDM was successfully prepared. However, structure determination of this complex using Cryo-EM single particle analysis failed due to the heterogeneity of the FusA:PM1 complex, likely caused by the partial collapse of FusA in DDM concentration lower than the CMC. Consequently, I considered alternative structural biology methods to address the interaction between FusA and PM1. X-ray crystallography was chosen to determine the atomic structure of native PM1. In this chapter, it is described how to determine the crystal structure of pectocin M1 and how the obtained structure provides insight into the mechanism of intact PM uptake into cells *via* the outer membrane receptor FusA in the ferredoxin uptake system (Fus).

In this study, I have determined the X-ray structure of full-length PM1 ($PM1_{full}$) at a resolution of 2.04 Å, unveiling a previously undocumented 'closed' conformation of PMs. Comparison of the distinct domain arrangements in PM1 and PM2 highlights differences in the orientation of conserved amino acids in the active site of the cytotoxic domain that are correlated with catalytic activity against *Pectobacterium* ssp. Analysis of the diverse domain arrangements in PMs, including our new PM1 structure, reveals the structural flexibility of PMs and how binding to the FusA receptor is enhanced in the initial step of PM uptake. Based on our full-length structure of PM1 and published chemical shift perturbation (CSP) data on the ferredoxin domain of PM1 ($PM1_{fd}$) titrated with FusA[14], we use HADDOCK modeling of FusA with the ferredoxin domain only (FusA:$PM1_{fd}$) and FusA with full-length PM1 (FusA:$PM1_{full}$) to investigate the interaction sites and optimum conformation of the transient binding of PMs to the FusA receptor during the initial uptake step. Collectively, these findings allow me to provide insight into the mechanism of intact PM uptake into cells *via* the ferredoxin uptake system.

3.2 Materials and methods

3.2.1 Bacteria strain and plasmid

The recombinant plasmid for producing PM1 was constructed as described previously in chapter 2. PM1 was expressed in *E. coli* BL21(DE3) pLysS host (Invitrogen) due to the tight control needed for expression of toxic proteins.

3.2.2 Expression and purification

Expression and purification of PM1 were carried out in the same manner as described previously in chapter 2.

The concentrated PM1 sample after purified by size exclusion chromatography on a HiLoad® 16/600 Superdex® 75 pg column (Cytiva). The fractions were analyzed by SDS-PAGE, together with aliquots of concentrated PM1 before injection and fraction 14 that had been heated for 1 minute at 90 ℃. PM1 was concentrated to 20 mg/mL using a 10-kDa MWCO Amicon filter (Millipore) and stored at –80 ℃ until crystallization. To verity the presence of iron sulfur cluster, the absorption spectra of a 50-fold dilution solution of purified PM1 at a wavelength of 300–650 nm was measured by using a V-630 UV-Vis Spectrophotometer (Jasco).

3.2.3 Crystallization and diffraction data collection

Crystallization trials were performed by using the sitting-drop vapor diffusion method at a PM1 concentration of 20 mg/mL. Crystallization droplets were prepared by mosquito LCP

technology (SPT Labtch, Royston, UK) using 100 nL of 20 mg/mL PM1 and 100 nL of reservoir solution from commercial screening kits (~400 conditions) at 4 ℃ and 20 ℃. A crystal was observed in Index™ 59 (0.02 M magnesium chloride hexahydrate, 0.1 M HEPES pH 7.5, 22% w/v polyacrylic acid sodium salt [PAS] 5100; Hampton Research, Aliso Viejo, CA, USA) at 20 ℃. Further optimization using the hanging-drop vapor-diffusion method in 0.1 M HEPES pH 7.5 and 19.2% w/v PAS 5100 resulted in the formation of brown clustered crystals with rod or plate shape.

The crystals were looped and cryoprotected by soaking for a few seconds in crystallization solution plus 20% glycerol before cryocooling in liquid N_2. The X-ray diffraction datasets were collected using a EIGER X 16M detector (DECTRIS, Baden-Dättwil, Switzerland) at SPring-8 using beamline BL44XU. The crystallographic statistics are summarized in **Table 3.1**.

3.2.4 Structure solution and refinement

The datasets were processed by XDS software[72]. The best dataset, which diffracted at 2.04 Å resolution, was solved by molecular replacement using Phaser[73] from the PHENIX package[74] with the structure of PM2 (PDB ID: 4n58)[21] as a template. An initial model was built using the AutoBuild program [75] in PHENIX. The model was built further and refined interactively using *Coot* software[76] and phenix.refine[77] up to 2.04 Å resolution. The final refined coordinates and structure factors of PM1 have been deposited to the Protein Data Bank (PDB) under the accession number 8jc1. The coordinates of chain B from the PM1 crystal structure were chosen for further atomic analysis because its electron density map was better than those of the other chains.

3.2.5 Interdomain interaction analysis

Interdomain interactions within PM1 structure was analyzed using the DIMPLOT program in the LigPlot^{+} suite[78] The ferredoxin domain (residues 2–94) was designated as domain A; the remaining regions (residues 95–268), including the cytotoxic domain and linker, were defined as domain B during the calculation.

3.2.6 Domain movement and rotational angle analysis

Rotational motions and angles between the catalytic domains of different conformations of pectocins were analyzed using DynDom[79]. Chain A from both PM2 structures (PDB ID: 4n58 and 4n59)[21] and chain B of PM1 were selected for this assessment. The two other coordinates of pectocin M2 (PM2), including open-form PM2 (PDB ID: 4n58), compact-form PM2 (PDB ID: 4n59), and closed-form PM1, have been submitted to the DynDom web server (https://dyndom.cmp.uea.ac.uk/dyndom/runDyndom.jsp) for analysis.

3.2.7 HADDOCK simulation

Simulated docking models of FusA (PDB ID: 4zgv)[14] and the ferredoxin domain of PM1 were calculated using HADDOCK 2.4[80] by submitting the coordinates to the HADDOCK web server (https://wenmr.science.uu.nl/haddock2.4/). The interacting passive residues within the extracellular loops of FusA was assigned based on previously published data[14]. Active residues in the ferredoxin domain were defined based on the criteria with CSP values of >0.02 ppm in a previous FusA–PM1$_{fd}$ NMR titration (1:1 molar ratio). During the simulation, 200 structures were

selected for the final refinement and then clustered into 10 groups based on the Fraction of Common Contacts of 0.60. The parameters in the docking were based on the default settings of the server, with the exception of a 25% removal of restraints. The N and C terminus for all proteins were treated as charged and uncharged, respectively. Detailed statistics for each cluster resulting from the docking simulation are presented in **Table 3.2**.

Table 3.1 Data collection and refinement statistics

Data collection	PM1
Wavelength (Å)	0.9000
Resolution (Å)	40.27-2.04 (2.12-2.04)
Space group	$P2_1$
Cell dimensions	
a, b, c (Å)	66.28, 138.55, 68.95
α, β, *γ* (º)	90, 94.18, 90
Total reflections	275746 (28529)
Unique reflections	78357 (7963)
Multiplicity	3.5 (3.6)
Completeness (%)	98.57(91.22)
Mean *I*/sigma (*I*)	9.73/1.61
Wilson plot B-value (Å^2)	38.86
R-meas	0.053 (0.794)
CC(1/2)	0.993(0.77)
Refinement	
Reflections used in refinement	77351 (7126)
Reflections used for *R*-free	1976 (170)
R-work	0.1952 (0.2798)
R-free	0.2329 (0.3333)
No. of non-hydrogen atoms	8765
Macromolecules	8158
Ligand/ion	67
Water	540
Protein residues	1068
RMS (bonds, Å)	0.007
RMS (angles, º)	0.85
Ramachandran favored (%)	95.56
Ramachandran allowed (%)	4.06
Ramachandran outliers (%)	0.38
Rotamer outliers (%)	1.47
Clashscore	5.11
Average B-factor (Å^2)	46.9
Macromolecules	47.0
Ligands	60.6
Solvent	45.0

Statistics for the highest-resolution shell are shown in parentheses.

Table 3.2 HADDOCK docking statistics [a].

	Cluster 5	Cluster 10	Cluster 1	Cluster 2	Cluster 7
HADDOCK score	–96.9 ± 7.8	–73.4 ± 4.1	–66.1 ± 2.1	–62.0 ± 1.2	–61.5 ± 7.8
Cluster size	8	4	54	38	6
RMSD from overall lowest-energy structure (Å)	0.8 ± 0.5	3.3 ± 0.3	9.1 ± 0.3	8.4 ± 0.2	7.7 ± 0
Van der Waals energy (kcal/ mol)	–59.2 ± 6.9	–51.9 ± 6.3	–50.8 ± 1.5	–49.9 ± 2.0	–39.8 ± 7.5
Electrostatic energy (kcal/mol)	–301.3 ± 5.8	–222.3 ± 18.6	–126.1 ± 10.2	–124.4 ± 14.3	–172.7 ± 34.6
Desolvation energy (kcal/mol)	14.0 ± 1.6	9.5 ± 2.4	0.2 ± 2.0	3.1 ± 0.7	4.4 ± 1.8
Restraints violation energy (kcal/mol)	84.5 ± 13.7	134.2 ± 20.9	97.3 ± 27.1	90.9 ± 21.1	84.4 ± 26.9
Buried surface area ($Å^2$)	2196.9 ± 210.2	1796.6 ± 116.5	1458.8 ± 33.1	1331.7 ± 47.6	1369.0 ± 97.1
Z-score	–2.3	–0.8	–0.4	–0.1	–0.1

	Cluster 6	Cluster 3	Cluster 4	Cluster 8	Cluster 9
HADDOCK score	–59.4 ± 8.2	–52.7 ± 3.2	–50.9 ± 2.3	–44.3 ± 8.2	–39.3 ± 12.1
Cluster size	7	16	9	5	4
RMSD from overall lowest-energy structure (Å)	7.1 ± 0.2	9.2. ± 0.2	6.4 ± 0.8	6.4 ± 0.3	7.2 ± 0.3
Van der Waals energy (kcal mol^{-1})	–45.1 ± 3.5	–39.7 ± 2.1	–36.7 ± 1.1	–43.8 ± 4.5	–20.1 ± 5.1
Electrostatic energy (kcal mol^{-1})	–121.9 ± 31.0	–87.8 ± 13.6	–143.2 ± 10.6	–38.6 ± 7.0	–156.2 ± 21.6
Desolvation energy (kcal mol^{-1})	4.8 ± 3.4	–3.4 ± 1.6	5.6 ± 1.0	–1.1 ± 0.9	2.1 ± 1.2
Restraints violation energy (kcal mol^{-1})	52.3 ± 26.9	79.6 ± 26.5	87.3 ± 44.5	82.7 ± 27.9	99.7 ± 45.9
Buried surface area ($Å^2$)	1371.8 ± 138.7	1282.6 ± 29.5	1317.0 ± 76.8	1271.3 ± 26.3	1091.6 ± 98.4
Z-score	0.1	0.5	0.6	1.1	1.4

[a] Docking statistics for each cluster of FusA and $PM1_{fd}$ generated by HADDOCK 2.4.

3.3 Results

3.3.1 Structure determination

The gel filtration profile of the purified sample revealed a predominant peak at 280 and 422 nm, showing the presence of a [2Fe-2S] cluster in ferredoxin domain (**Fig. 3.1A**). SDS-PAGE indicated a purity of more than 95%, but the observation of two bands in non-heated samples and one band in heated samples showed that PM1 adopts multiple conformations in solution (**Fig. 3.1B**). The absorption spectrum of purified PM1 showed peaks at 330, 423, and 466 nm (**Fig. 3.1C**), consistent with that of other pectocins and ferredoxins containing a [2Fe-2S] cluster[23,81,82].

Initial crystallization trials yielded small rod-shaped crystals of PM1 after 2 days in the condition of 0.02 M magnesium chloride hexahydrate, 0.1 M HEPES pH7.5, and 22% w/v PAS 5100 at 20 ℃ (**Fig. 3.2A**). Both rod and plate-shaped crystals were observed in the optimized condition of 0.1 M HEPES pH 7.5 and 19.2% w/v PAS 5100 with the hanging-drop vapor-diffusion method (**Fig. 3.2B**). One rod-shaped crystal diffracted well, providing the monoclinic space group of $P2_1$ with unit cell parameters of a = 66.28 Å, b = 138.55 Å, c = 68.95 Å, and β = 94.18º. The estimated number of molecules in the crystallographic asymmetric unit was four with a Matthews coefficient (V_M) of 2.63 Å^3/Da and solvent content of 53.3%.

The PM1 protein, including the ferredoxin domain (residues 1–94), α-helix linker (95-116), and catalytic domain (117–268), contains 268 amino acids with a molecular mass of 29.3 kDa (**Fig. 3.3A**). Molecular replacement using the full-length PM2 structure as a template failed in the beginning. Thus, the catalytic and ferredoxin domain each of PM2 was independently used as templates (PDB ID: 4n58) and the molecular replacement succeeded. The initial model from AutoBuild package was further refined at 2.04 Å resolution. The crystallographic statistics are

summarized in **Table 3.1**. The final coordinate contains four PM1 molecules in the crystallographic asymmetric unit. Each monomer, comprising an N-terminal ferredoxin domain and a C-terminal catalytic domain interconnected by an α-helix, is in principle the same (**Fig. 3.4**). The model of chain B (**Fig. 3.3B**) has been used as a representative in subsequent analyses because its electron density map was better than those of the other chains.

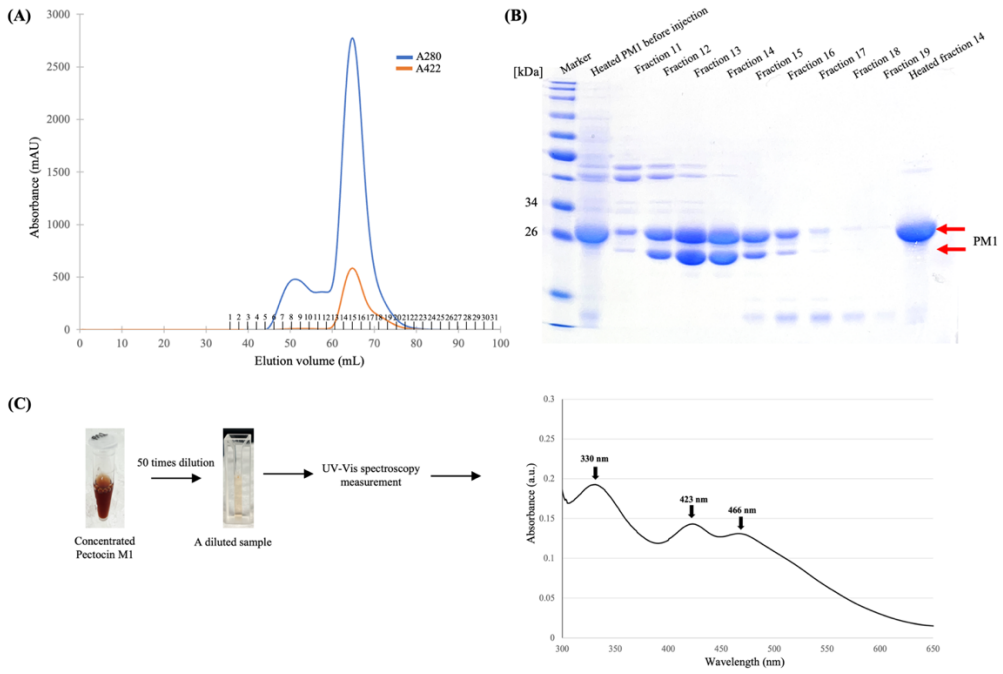

Figure 3.1 PM1 purification. (A) Superdex 75 10/60 gel filtration profile of purified PM1 monitored at wavelengths of 280 and 422 nm. **(B)** SDS-PAGE analysis of PM1 samples before and after gel filtration, and with and without heat treatment. Red arrows indicate two bands corresponding to PM1. **(C)** Workflow detailing UV-Vis spectroscopy measurement of a 50-fold diluted PM1 solution after the final purification step

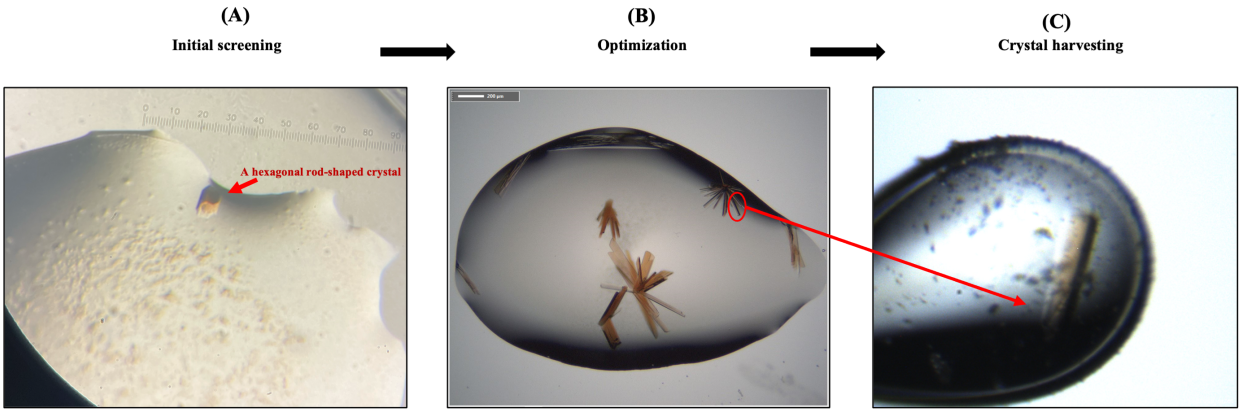

Figure 3.2 Pectocin M1 crystallization. (A) Single crystal (~80 x 20 µm) of PM1 obtained after 2 days during the initial screening. **(B)** Brown crystals with rod and plate clusters formed after 21 days of optimization using 0.1 M HEPES at pH 7.5 and 19.2% w/v poly (acrylic acid sodium salt) 5100. **(C)** The indicated rod-shaped crystal (~150 × 40 µm) in **(B)** was harvested using 20% glycerol as a cryoprotectant and used for subsequent data collection.

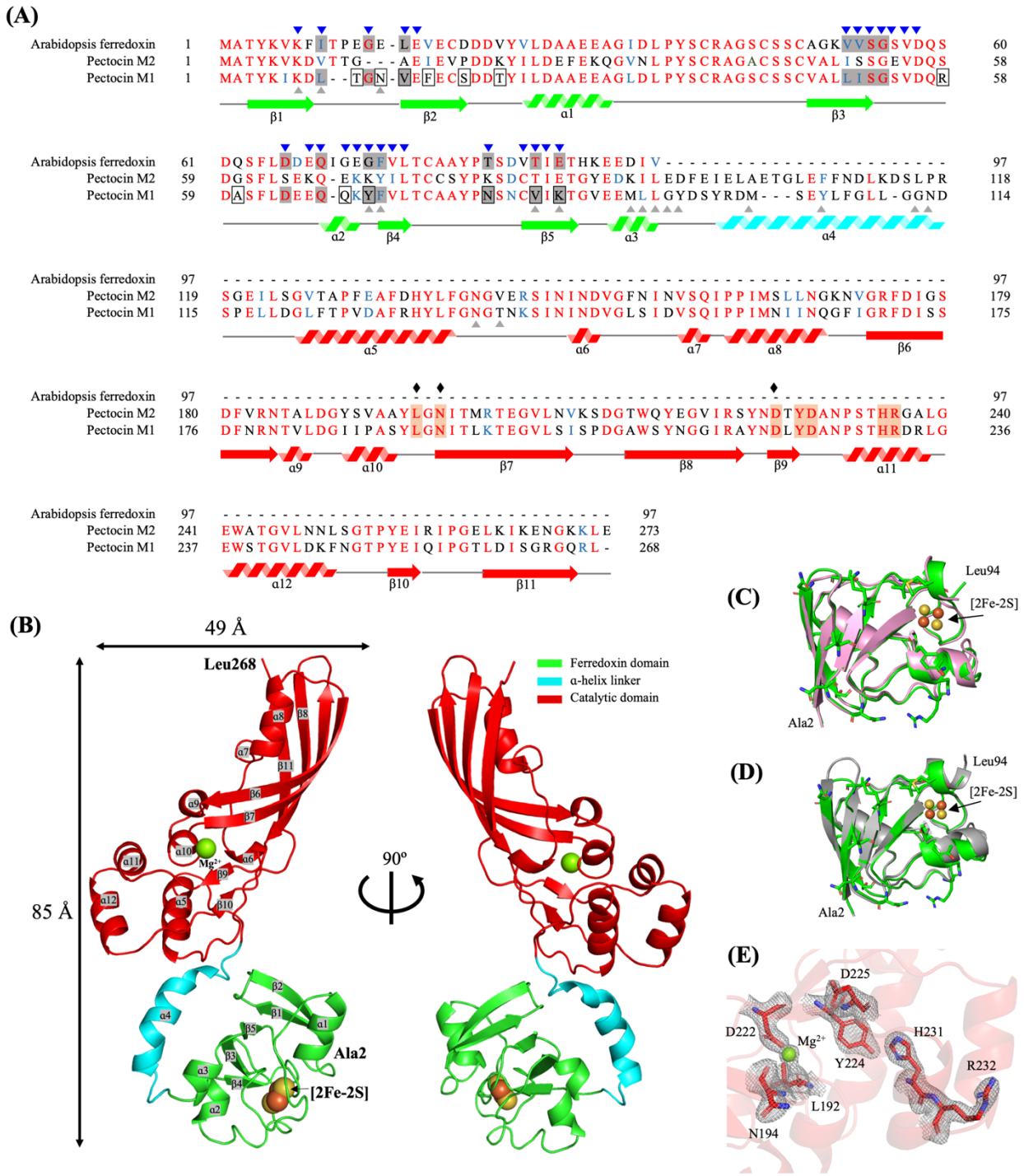

Figure 3.3 Comparison of PM1 with other ferredoxin domain-containing proteins. (A) Multiple sequence alignment of PM1, PM2, and AtFd2. Identical residues are in red, similar residues in blue, and unique residues in black. Colored arrows and zigzags denote the ferredoxin

domain (green), α-helix linker (cyan), and catalytic domain (red). Blue arrowheads indicate residues with CSP values of >0.02 ppm in a previous FusA–$PM1_{fd}$ NMR titration (1:1 molar ratio)[14]. A gray background indicates active residues in HADDOCK docking; black boxes highlight amino acids unique to the PM1 ferredoxin domain; gray arrowheads indicate amino acids of PM1 involved in interdomain interactions as analyzed by Ligplot+. Key active site residues of the catalytic domain are highlighted with an orange background; black diamonds indicate amino acids that interact with the Mg^{2+} cofactor. **(B)** Schematic depicting the crystal structure of PM1 observed in the $P2_1$ space group. The ferredoxin domain is green, α-helix linker cyan, and catalytic domain red. Spheres represent the [2Fe-2S] cluster. **(C)** Schematic showing the ferredoxin domain of PM1 (green) superimposed with that of PM2 (pink; PDB ID: 4n58) (backbone r.m.s.d. = 0.529 Å, PM1 residues = 2–94, PM2 residues = 2–94). **(D)** Schematic illustrating the ferredoxin domain of PM1 (green) aligned with that of AtFd2 (gray; PDB ID: 4zho) (backbone r.m.s.d. = 0.678 Å, PM1 residues = 2–94, AtFd2 residues = 2–98). Unique amino acids in the ferredoxin domain of PM1 are represented by sticks (black boxes in (A)). **(E)** Schematic diagram of the active site of catalytic domain with 2|*F*o|-|*F*c| electron density map (contoured at 1.6 σ and colored in grey).

3.3.2 Structure of PM1

The overall structure of PM1 has dimensions of 49 Å (width) and 85 Å (length), and is clearly larger than the FusA plug domain. Each domain of PM1 looks similar to its counterpart in the published PM2 structures (PDB ID: 4n58 and 4n59); however, the three-dimensional arrangement of these domains in PM1 differs from that in PM2.

Multiple sequence alignment reveals that the ferredoxin domain of PM1 possesses 13 unique residues (**Fig. 3.3A**, boxes), which are located on the back side of the domain away from the [2Fe-2S] cluster. This side is thought to be crucial for binding to FusA[14]. The ferredoxin domain itself shows 0.529 Å of r.m.s.d. based on Cα carbons and 60.6% of sequence identity to that of PM2 (PDB ID: 4n58, **Fig. 3.3C**)[21], and 0.678 Å and 63.9%, respectively, to that of *Arabidopsis thaliana* Fd2 (AtFd2) (PDB ID: 4zho, **Fig. 3.3D**), suggesting that differences exist only in the surface structure attributed to the side chains. The PM1 catalytic domain adopts an elongated structural feature of mixed α-helix/β-sheet components (**Fig. 3.3B and 3.5A**), commonly found in M-class bacteriocins[21,43,45,58]. The backbone structure of the catalytic domain in PM1 also shows high similarity to that of PM2 (PDB ID: 4n58) with an r.m.s.d. of 0.733 Å based on Cα atoms (**Fig. 3.5B**).

A strong peak in the electron density map is found in the active site of catalytic domain, similar to the cases of PM2[21], pyocin M (PaeM)[43], and syringacin M (SyrM)[45]. I assigned this as an Mg^{2+} ion because it fitted perfectly in this map with better values of *B*-factor and ligand coordination (**Fig. 3.3E**)[83], consistent with the catalytic activity of PM1 in presence of Mg^{2+} ion[22]. Amino acid residues conserved in the active sites (**Fig. 3.5A** and **Fig. 3.3A**, highlighted with an orange background) are similarly oriented, particularly metal-coordinated residues (**Fig. 3.3A**,

black diamonds). A notable difference is the position of the α11 helix in PM1. This helix aligns in parallel with the neighboring α5 and α12 helices in PM1, whereas the corresponding helix positions are perpendicular in PM2, leading to a different orientation of the conserved His231 and Arg232 in PM1 corresponding to His235 and Arg236 in PM2 (**Fig. 3.5A**, right). In the PM1 structure, these two residues are situated apart from other conserved residues, opening up the active site. Conversely, in the PM2 structures, these residues (His235 and Arg236) are directed toward two other conserved residues in the active site, Asn198 and Asp226 (PM2), which form hydrogen bonds with a water molecule and thereby prevent substrate from accessing the active site. The orientation of His231 and Arg232 (His235 and Arg236 of PM2) looks a key to control the accessibility of substrates into the active site as shown in **Fig. 3.5A**.

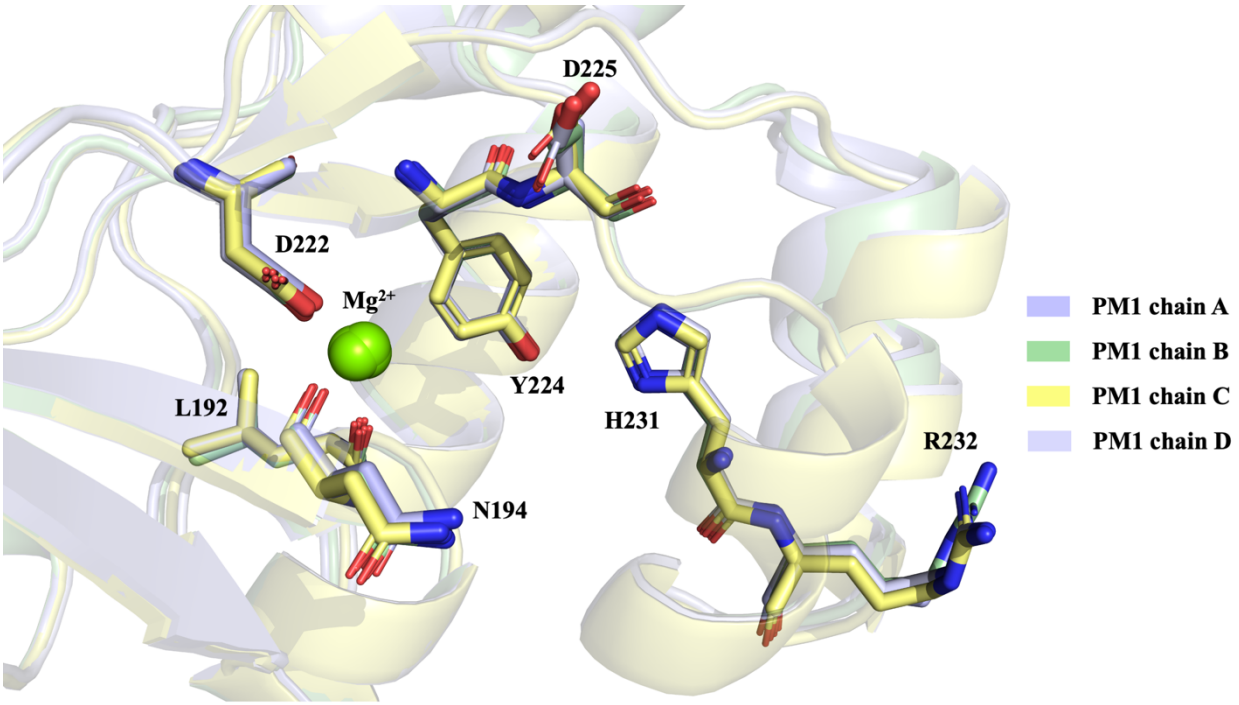

Figure 3.4 Superimposed models of the catalytic domain of four PM1 molecules in the crystallographic asymmetric unit (residues = 135–267). The key amino acids in the active site of the catalytic domain PM1 are represented by sticks.

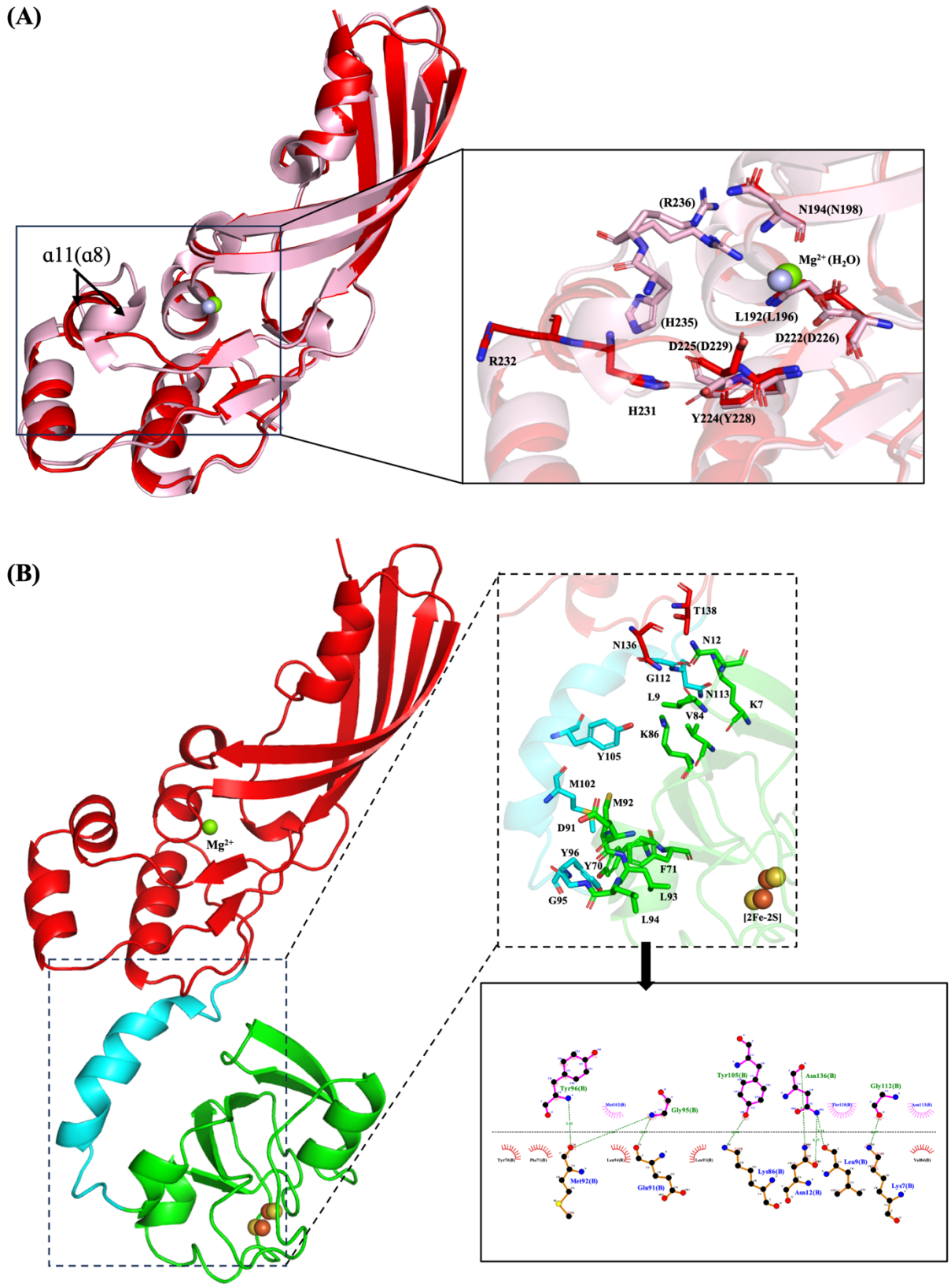
(A)
α11(α8)
(R236)
N194(N198)
Mg2+ (H2O)
(H235)
L192(L196)
D222(D226)
D225(D229)
R232
H231
Y224(Y228)
(B)
Mg2+
T138
N136
N12
G112
L9
N113
K7
V84
K86
Y105
M102
M92
D91
Y96
Y70
F71
G95
L93
L94
[2Fe-2S]
Tyr96(B)
Gly95(B)
Tyr105(B)
Asn136(B)
Gly112(B)
Met92(B)
Glu91(B)
Lys86(B)
Asn12(B)
Leu9(B)
Lys7(B)

Figure 3.5 Molecular insights into PM1 interdomain interactions and the active site. (A) Schematic alignment of the cytotoxic domains of PM1 (red) and PM2 (pink; PDB ID: 4n58) (backbone r.m.s.d. = 0.733 Å, PM1 residues = 120–268, PM2 residues = 124–271). The magnified view in the black panel focuses on the active site in PM1 and PM2, displaying key conserved residues as sticks with PM2 residues given in brackets. Mg^{2+} cofactor in PM1 and water molecule in PM2 are represented as green and light blue spheres, respectively. **(B)** Analysis of key amino acids of PM1 involved in interdomain interactions by LigPlot^{+}, highlighting residues in the ferredoxin domain in green, others in cyan and red as shown in the black dashed box. The magnified view in the black panel shows the interdomain interaction region, displaying key amino acids represented as sticks and the [2Fe-2S] cluster as spheres.

3.3.3 Domain arrangement and interdomain interaction of PM1

The two dimensions of PM1 obtained from the crystal structure in this work (85 Å × 49 Å) are similar to those determined by DAMMIF model in the SAXS analysis from the previous work (82 Å × 54 Å)[71], suggesting that the PM1 in the closed conformation is the most stable form and predominantly exits in solution. However, the CRYSOL SAXS curve predictions, coupled with ensemble optimization modeling, revealed that PM1, like PM2, is flexible and adopts multiple conformations with maximum dimensions ranging from 70 - 90 Å[71]. These findings support the existence of the domain rearrangement in PM1 between the closed form (the maximum dimension of 85 Å) and these potential intermediate conformations.

The domain arrangement found in PM1 is differs completely from that in the two PM2 structures. I call the PM1 domain arrangement the 'closed' form, consistent with a previous small-angle X-ray scattering (SAXS) study[71]. Conversely, the two other structures of PM2 show 'open' (PDB ID: 4n58) and 'compact' (PDB ID: 4n59) forms, both of which expose their back side of the ferredoxin domain to the solvent[21]. I used LigPlot^{+} to assess interdomain interactions, which revealed key amino acids on this side of the ferredoxin domain (Lys7, Leu9, Asn12, Tyr70, Phe71, Val84, Lys86 Met92, Leu93, Leu94; **Fig. 3.3A**, gray arrowheads; **Fig. 3.5B** right, stick models) that interact extensively with amino acids in other domains (Gly95, Tyr96, Met102, Tyr105, Gly112, Asn113, Asn136, Thr138; **Fig. 3.5B**). Among them, Lys7, Leu 9 and Asn136 are conserved between PM1 and PM2, implying that some interdomain interactions are shared in two isoform proteins.

Even for the closed or compact form of pectocin, the molecular dimensions are bigger than the plug domain of FusA, which means that domain rearrangement or structure melting must take

place to allow their translocation into the periplasm. To visualize and quantify the varied domain arrangement in PM2 suggested previously by SAXS[71,84], I calculated the differential rotational angles of the catalytic domains in the three forms of PM structure using the DynDom program[79] as 105.8º (open vs closed form; **Fig 3.6A**), 85.6º (open vs compact; **Fig 3.6B**), and 179.5º (compact vs closed; **Fig 3.6C**). Based on these data, I propose that there is preferred but restricted rotational movement of the catalytic domain via the α-helix linker, which might be important for the ferredoxin domain to expose its back side to FusA (**Fig. 3.6D**).

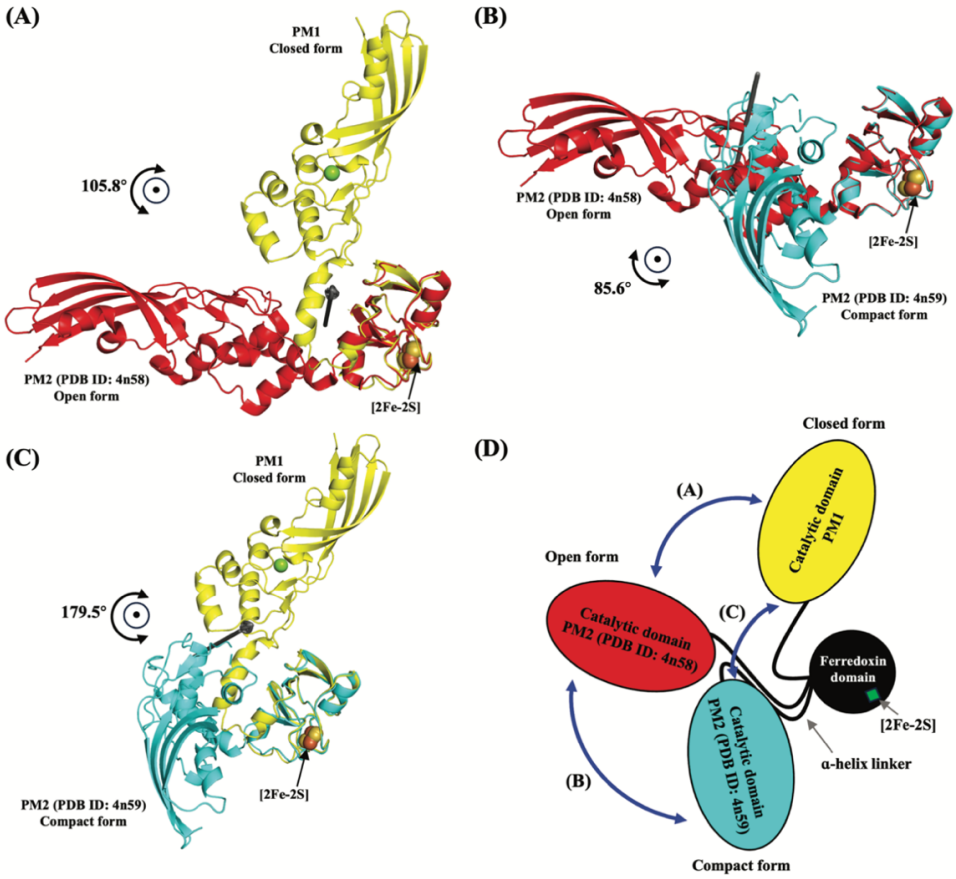

Figure 3.6 Comparative analysis of domain motions and rotational angles of catalytic domains between diverse conformations of PM. Domain movement and rotational angles of the catalytic domain via the flexible linker between are shown in **(A)** PM1 and PM2 (PDB ID: 4n58), **(B)** PM2 (PDB ID: 4n58) and PM2 (PDB ID: 4n59), and **(C)** PM1 and PM2 (PDB ID: 4n59), calculated by DynDom. Cartoons represent the crystal structure of PM1 (yellow), PM2 (red; PDB ID: 4n58), and PM2 (cyan; PDB ID: 4n59). The [2Fe-2S] cluster is shown as spheres. **(D)** Schematic drawing of the rotational motion between the catalytic domain of different conformational pectocins: PM1 (yellow), PM2 (red; PDB ID: 4n58), and PM2 (cyan; PDB ID: 4n59). The ferredoxin domain and the [2Fe-2S] cluster are represented by black spheres and green squares, respectively; the linker is shown as a black line.

3.3.4 Docking models of the complex between PM1 and FusA

Next, I explored the structure of the PM1–FusA complex using our X-ray structure of full-length PM1 coupled with a previous NMR-based interaction study between FusA extracellular loops and the ferredoxin domain of PM1 ($PM1_{fd}$)[14]. First, I mapped residues of the ferredoxin domain of PM1 reported to have a CSP of >0.02 ppm upon FusA addition at a 1:1 molar ratio[14]; (**Fig. 3.3A**, residues with a gray background) on the X-ray structure of PM1 (**Fig. 3.7A**, wheat-colored residues). The complex structure between the ferredoxin domain of PM1 and FusA (FusA:$PM1_{fd}$) was then predicted using the HADDOCK 2.4 program[80]. Below, I describe the two models with the best scores. In both predicted models, the ferredoxin domain is bound to the extracellular loops of FusA, exhibiting a similar binding mode through its back side but with a rotational variation of 50.4º (**Fig. 3.7B**). Notably, the previously reported docking models of FusA:AtFd2[14] show a distinct binding mode of AtFd2 (**Fig. 3.8**).

In both FusA:$PM1_{fd}$ models, the plug domain and the L1, L4, L5, L7, and L11 loops of FusA accommodate $PM1_{fd}$ (**Fig. 3.7C**, **3.7D**), whereas the plug domain and only three loops of FusA (L4, L5, and L7) host AtFd2 in the previously published FusA:AtFd2 model (**Fig. 3.8C**, **3.8D**). This difference in prediction may be caused by sequence variations in the back side of the ferredoxin domains (**Fig. 3.3A**, black boxes). Mapping the electrostatic potentials onto the surface of FusA, $PM1_{fd}$, and AtFd2, calculated with APBS Electrostatics plugin[85] in PyMOL program[86] , clearly explains these different preferences in binding (**Fig. 3.7C**; **Fig. 3.8C**). While the inner walls of FusA (L2, L4, L5, L7, L8, L10 and L11 loops) are positively charged and the plug domain (**Fig. 3.7B**, **3.7D**, blue stick model; and **Fig. 3.8B**, **3.8D**) exhibits a negative charge on the inner floor (**Fig. 3.7C** and **Fig. 3.8C**), the back sides of $PM1_{fd}$ and AtFd2 are clearly

different with more negative charges in AtFd2, and less negative and even positive charges in $PM1_{fd}$.

Finally, I superimposed the full-length PM1 structure and the two PM2 structures on the best-score FusA:$PM1_{fd}$ model (**Fig. 3.9A**). Using the CONTACT program in the CCP4 suite[87], the number of amino acid residues collided with the FusA molecule in all cases (**Fig.3.9A**). The degree of collision was highest for the closed conformation, intermediate for the compact form, and lowest for the open conformation when simply superimposed.

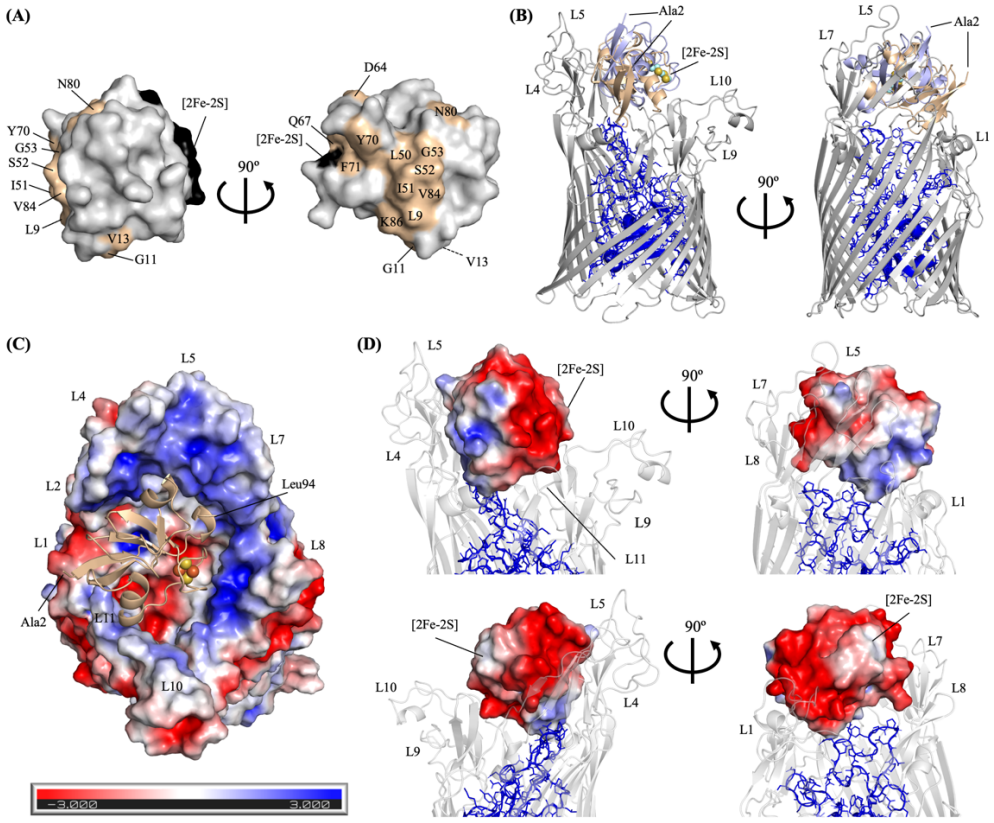

Figure 3.7 Structural analysis of FusA and PM1$_{fd}$ via HADDOCK simulation. (A) Active residues assigned in the simulation (indicated on a gray background in Fig. 1A) are mapped onto the surface of the 3D structure of PM1$_{fd}$ (wheat color). **(B)** Crystal structure of FusA (gray) with the top two models of PM1$_{fd}$ superimposed (wheat color, 1st rank; light blue, 2nd rank). The plug domain of FusA is shown as a blue stick and cartoon model; the [2Fe-2S] cluster is shown as spheres. **(C)** Top scored model of the FusA–PM1$_{fd}$ complex. FusA is shown as a molecular surface mapped with electrostatic potential; the crystal structure of PM1$_{fd}$ is shown as a wheat cartoon model. **(D)** Molecular surface mapped with electrostatic potential of PM1$_{fd}$ docked to FusA viewing from the front (top panel) and the back (bottom panel) with the right panel rotated in 90° each, shown as a white cartoon with its plug domain highlighted as a blue cartoon and stick model.

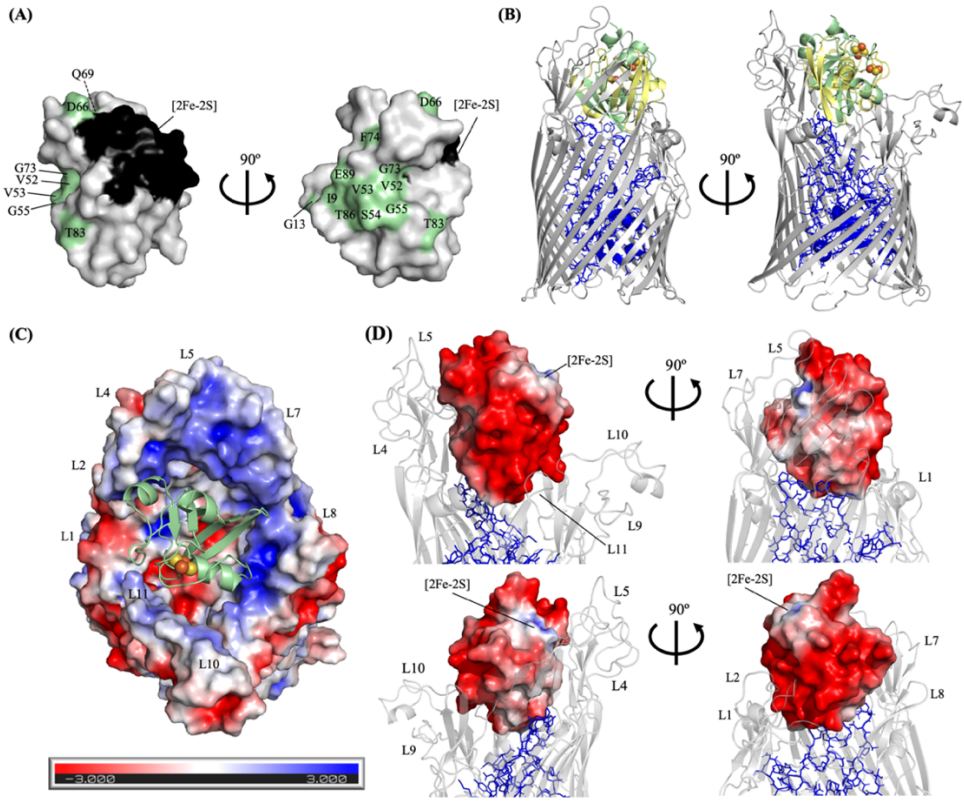

Figure 3.8 Structural analysis of the FusA–AtFd2 complex obtained via HADDOCK docking simulation. (A) Active residues assigned in the simulation (indicated on a gray background in Fig. 1A) are mapped onto the surface of the 3D structure of AtFd2 (light green). **(B)** Crystal structure of FusA (gray) with the top two models of AtFd2 superimposed (pale green, 1st rank; pale yellow, 2nd rank). The plug domain of FusA is shown as blue sticks and cartoons; the [2Fe-2S] cluster is shown as spheres. **(C)** Top scored model of the FusA–AtFd2 complex; FusA is shown as a molecular surface mapped with electrostatic potential; the crystal structure of AtFd2 is shown as a green cartoon model. **(D)** AtFd2 molecular surface mapped with electrostatic potential docked to FusA viewing from the front (top panel) and the back (bottom panel) with the right panel rotated in 90° each, shown as a white cartoon model with its plug domain shown as a blue stick and cartoon model.

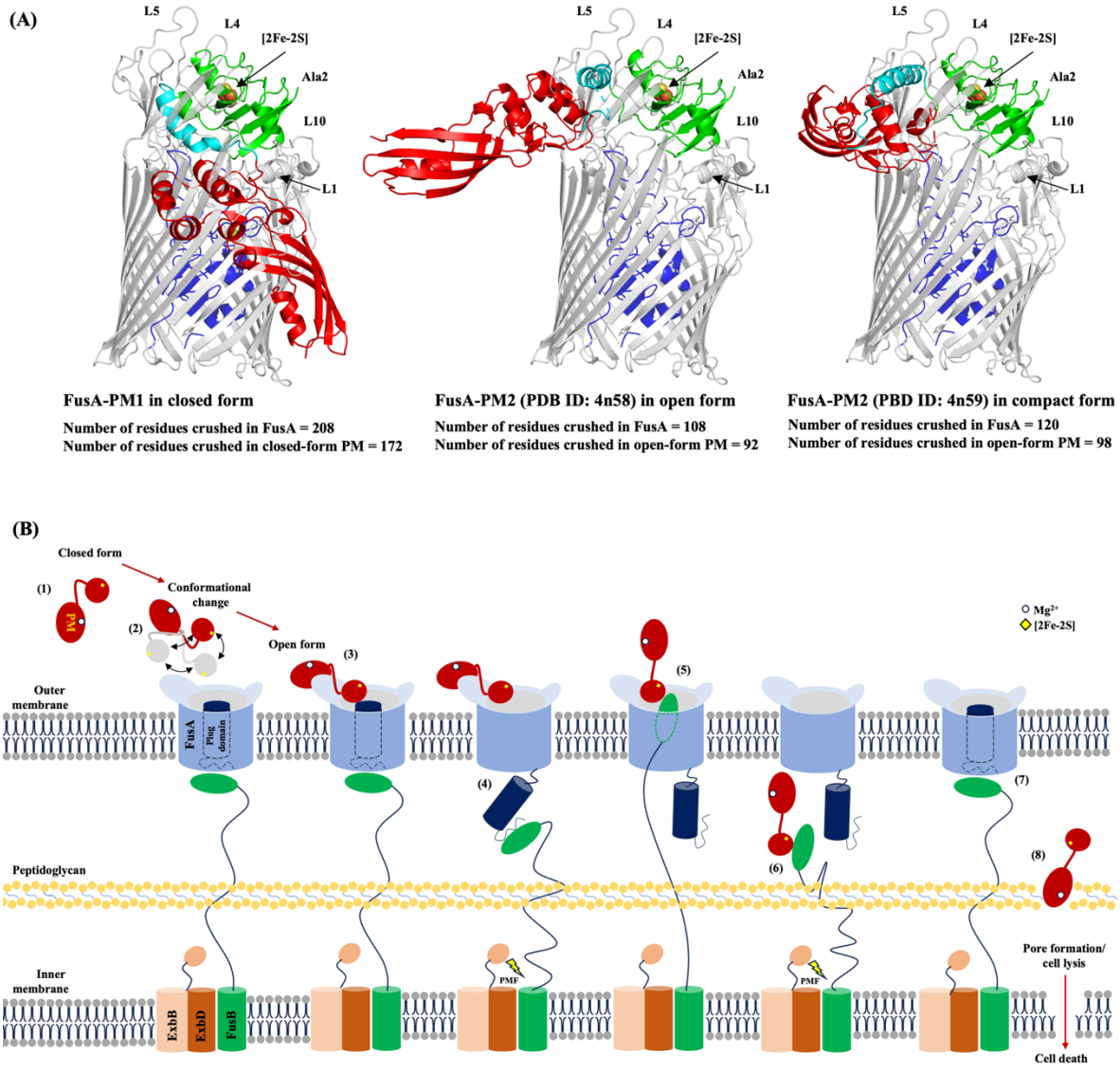

Figure 3.9 Model of the uptake of intact PM via the receptor FusA into *Pectobacterium* ssp. cells. (A) Structural superimposition of the ferredoxin domain of the FusA–$PM1_{fd}$ complex obtained from HADDOCK docking with that of the different conformations of PM shows that PM forms extensive interactions and collisions with the extracellular loops and plug domain of FusA. FusA and PM are depicted as cartoon models. FusA and its plug domain are colored grey and blue, respectively, while the ferredoxin domain, the helical

linker, and the catalytic domain of PM are colored in green, cyan, and red, respectively. Analysis of collisions among amino acid residues in complexes of FusA and different conformations of PM in FusA–PM1, FusA–PM2 (PDB ID: 4n58), and FusA–PM2 (PDB ID: 4n59) was performed using the Contact program in the CCP4 software suite[87]. The number of residues crushed in FusA and PM in each docking model are presented. **(B)** Proposed mechanism of the uptake of intact PM through the receptor FusA into *Pectobacterium* ssp. cells via the ferredoxin uptake system. In the extracellular environment, PM in the closed form **(1)** reaches the extracellular loops and plug domain of FusA, inducing a conformational change to the open form **(2)** and exposing the binding surface of PM to the extracellular loops and plug domain of FusA **(3)**. The resultant binding triggers release of the FusA plug domain into the periplasmic space, where it binds to FusB through energy transduced from the proton motive force (PMF) generated by the ExbBD complex **(4)**. Subsequently, FusB enters the FusA lumen and interacts with the ferredoxin domain of PM **(5)**. Using energy from PMF, FusB induces a conformational change of intact PM to an elongated form, and then translocates PM into the periplasm **(6)**. The plug domain re-enters the FusA lumen, restoring FusA and FusB to their resting states **(7)**. Lastly, PM binds to peptidoglycan, initiating digestion of the lipid II substrate via its catalytic domain and leading to pore formation, cell lysis, and ultimately cell death **(8)**.

3.4 Discussion

The uptake of M-class bacteriocins across the outer membrane of a target cell typically utilizes TonB-dependent receptors[42,58] in a pathway similar to the case of iron acquisition systems of Gram-negative bacteria[88]. The TonB-dependent receptor FusA, a component of plant-ferredoxin uptake systems used by *Pectobacterium* ssp., has been also identified as a receptor for PM uptake[14,71]. However, it has remained unclear how full-length PMs comprising ferredoxin and catalytic domains can be recruited to and translocated through FusA. In this study, therefore, I determined the full-length structure of PM1 that has potential use as a biological agrochemical to investigate the mechanism underlying the translocation of PMs across the outer membrane.

Comparison of the catalytic domain of PM1 with that of PM2 (PDB ID: 4n58) revealed that the two domains each had nearly identical structure due to high sequence similarity (>60%). However, a difference in orientation between the α11 helix of catalytic domain in PM1 and the corresponding α8 helix in PM2 alters the relative orientations of the conserved His231 (His235 in PM2 numbering) and Arg232 (Arg236) residues on these helices (**Fig. 3.5A**), creating a much more open active-site cavity in PM1 that enhances the accessibility of peptidoglycan lipid-II intermediates as a substrate. A conserved arginine residue is similarly positioned outside the active site in the homologous bacteriocins pyocin M and Syringacin M, also resulting in open active-site cavities[43,45]. This observation suggests that there is high flexibility in these regions within the M-class bacteriocin family, potentially aiding in lipid-II coordination and stabilization of the pyrophosphate group near key catalytic residues[21]. Although the catalytic mechanism of M-class bacteriocins toward lipid-II substrates remains unclear, I suggest that the PM1 structure identified in this work represents a highly active-site conformation, while the previous PM2 structures

represent a less active state, which correlates with their catalytic performance towards *Pectobacterium* ssp.[21,23].

Owing to the lack of a full-length PM1 structure, a previous model of the uptake of PM1 through FusA was proposed based on NMR spectroscopy of the ferredoxin domain of PM1 and subsequent site-directed mutagenesis[71]. Our newly determined X-ray structure of full-length PM1 allows me to develop this model further. In the full-length PM1 structure, the ferredoxin domain and colicin M-like catalytic domain are uniquely interconnected by a flexible helix linker in a 'closed' conformation. HADDOCK-simulated models of FusA:PM1$_{full}$ complexes based on the FusA:PM1$_{fd}$ complex (**Fig. 3.9A**, left) revealed extensive collision between FusA and PM1 in the closed conformation. I therefore performed docking between FusA and full-length PM with the previously documented open and compact forms of PM2 (**Fig. 3.9A**, middle and right). However, none of three docked models looks feasible because of collision; thus, domain rearrangement is clearly required for productive complex formation between PM and the extracellular loops of FusA. This domain rearrangement may involve a partial melt to facilitate translocation of PM with its additional catalytic domain relative to plant-type ferredoxin. Our predicted model of FusA:PM1$_{fd}$ shows clear differences from the previously predicted FusA:AtFd2 model in terms of orientation and positioning of the ferredoxin domain[14] (**Fig. 3.7** and **Fig. 3.8**). Differences in the sequence of the back side of the ferredoxin and ferredoxin domain of PMs, which would impact binding energies and electrostatic potential between FusA and the ferredoxin domain, may be central to the domain rearrangement function, suggesting that these interactions are crucial for facilitating the binding of PMs to FusA in the initial transportation step of intact PM through the FusA lumen.

Fig. 3.9B shows my proposed model of PM translocation *via* a partial melt of structure at the domain level. (1) In this model, PM adopts the closed conformation for stability and to prevent the binding interface on the ferredoxin domain interacting with other molecules in the extracellular environment. (2) When the closed-form of PM reaches the extracellular loops of FusA embedded in the outer membrane of the target cell, it fluctuates among its diverse conformations *via* movement of the domain and α-helix linker to produce the open conformation, (3) enabling the ferredoxin domain to bind extensively to the extracellular loops and plug domain of FusA, as analyzed using the DynDom program[79]. (4) Binding of PM to the plug domain of FusA causes dislocation of the plug domain to the periplasm, where it is bound by FusB through energy transduced from PMF generated by the ExbBD complex.

To pass through the outer membrane, intact PM needs to adopt an elongated conformation that closely fits the dimensions of the FusA lumen. Because the dimensions are so similar, it seems unlikely that PM passively diffuses through this pore. Therefore, I suggest that, (5) when FusB inserted into the FusA lumen interacts with the ferredoxin domain of PM bound to the FusA extracellular loops, it triggers a change in PM to the elongated conformation. This process probably relies on (6) a subsequent step driven by PMF, which would be essential for pulling the elongated PM through the FusA lumen. In the next step, (7) PM is released into the periplasm, allowing the plug domain to re-enter the FusA lumen, which returns FusA and FusB to their resting states. (8) Lastly, PM reaches the peptidoglycan lipid-II intermediates in the periplasm and digests them, leading to pore formation, cell lysis, and ultimately, cell death.

In summary, I have described the structurally dynamic characteristics of PM1, a bacteriocin from *P. carotovorum*, focusing on its interaction with the outer membrane receptor FusA in the

initial step of PM uptake *via* the ferredoxin uptake system. The crystal structure of full-length PM1 reveals a previously undocumented closed domain arrangement, stabilized by extensive interdomain interactions. This structure, together with docking models simulated in this study, provides insights into the structure-based translocation mechanism of PM1 during the initial steps of its importation into the periplasmic space of susceptible cells, highlighting its parasitization of the FusA receptor of the ferredoxin uptake system. Comparison with AtFd2 structure highlights structural similarities but also differences in the electrostatic surface properties on the back side of the ferredoxin domains. These differential electrostatic potentials may explain why structural differences not in the main chain but in the side chains level affect the preference of binding position and orientation of $PM1_{fd}$ to FusA in the docking models. Collectively, the findings in this work provide insights into the structure-based mechanism of PM1 during the initial steps of its importation into periplasmic space of susceptible cells by parasitizing receptor FusA of the ferredoxin uptake system.

Chapter 4

Molecular Insights into Ferredoxin Uptake *via* the TonB System in *Pectobacterium carotovorum*: The Role of FusB Oligomerization and Interactions with Ferredoxin or Pectocin M1

4.1 Introduction

Iron is an essential element for the growth[89] and infectious ability[90] of pathogenic bacteria. Although it is one of the most abundant elements on Earth, iron is often available in limited amounts for bacteria due to its insolubility under aerobic conditions[89]. Gram-negative bacteria have evolved considerable resources to acquire iron and employ elaborate control mechanisms to alleviate iron deficiency in iron-limiting environments, with TonB-dependent receptors (TBDRs) being crucial to this process[24,91]. These transporters in TBDRs family target microbial iron-scavenging siderophores and iron-containing proteins such as lactoferrin, transferrin, hemoglobin, ferritin, and ferredoxin[14,24,92]. For iron piracy from host iron-containing proteins, these proteins are captured by binding to TBDRs embedded in the outer membrane and subsequently transported through the barrel pore of TBDRs for further iron stripping[24,93]. An energizing complex of Ton system consisting of TonB/ExbB/ExbD anchored in the bacterial inner membrane conveys the energy of the proton motive force (PMF) for facilitating translocation of iron-containing molecules across TBDR lumen in this system[24,94].

Early research demonstrated the role of TonB systems in siderophore-mediated iron uptake[94]. In addition to the uptake of small molecules such as metal chelating compounds and iron siderophores, more recent studies have explored the ability of TonB systems to extract iron directly from host proteins[14,92]. This involves more complex interactions due to the larger and more variable nature of protein substrates compared to siderophores. In importing these large molecules, monomer TonB proteins have been observed to directly interact with their specific substrates, in contrast to the well-studied siderophore substrates in the Ton system[42,46,47]. TonB directly interacts with TonB-box of the colicin and pyocin containing intrinsically unstructured translocation domain (IUTD), facilitated by the TBDR plug domain in lumen.

Pectobacterium species utilize a specialized TBDR, FusA, for importing ferredoxins and ferredoxin-containing bacteriocins as discussed in the chapters above[14]. The Fus system is unique in that it possesses a TonB-like protein called FusB. This protein aids ferredoxin entry by removing the force-sensitive plug domain of FusA, utilizing energy from the PMF generated by the ExbBD complex, and then dragging ferredoxin through the channel[37]. Recent work has shown that FusB directly forms a stable complex with intact ferredoxin substrates and the ferredoxin domains of bacteriocins outside of the TBDR lumen[37]. This additional function of FusB may facilitate the traversal of these proteins in their intact form through the FusA channel. In Chapter 3, based on structural information of full-length PM1 coupled with HADDOCK docking models, I elucidated the initial step of ferredoxin uptake *via* the ferredoxin uptake system, highlighting the interaction between the FusA and ferredoxin domain of PM1. However, insights into the mechanism underlying the complex

formation between the FusB and ferredoxin/PM1 during ferredoxin uptake into target cells remain unclear due to the lack of an atomic-resolution structure of the FusB and ferredoxin/PM1 complex. In this chapter, I focused on the further step of ferredoxin uptake after binding of ferredoxin/PM1 to FusA and elucidated how ferredoxin uptake system works through FusA lumen using energy transduced from FusB/ExbB/ExbD complex, underlying intermolecular interactions of FusB and ferredoxin/PM1.

This chapter aims to determine the oligomeric state of FusB responsible for interacting with ferredoxin/PM1 and elucidate the structural details of the FusB-ferredoxin complex during ferredoxin/PM1 uptake. Structural and biochemical studies have significantly advanced our understanding of the ferredoxin uptake system. The study employs a multi-disciplinary approach, combining analytical SEC, X-ray crystallography, and ITC to examine the FusB-ferredoxin/PM1 interaction. Initial SEC analysis revealed that FusB exists in both dimeric and monomeric states in aqueous solution, with the dimeric form capable of forming stable complexes with ferredoxin. These findings were further supported by crystallographic data, which provided high-resolution structural details of the homodimeric FusB and monomeric ferredoxin complex that revealed the structural formation of this productive complex. ITC analysis revealed that the enthalpy-driven complex formation of FusB and ferredoxin/PM1 in solution is thermodynamically favored and simultaneous, possibly facilitating the capture of ferredoxin by homodimeric FusB in the periplasmic space. Combining the mapping of interactions with an understanding of the conformational changes induced upon binding of ferredoxin to homodimeric FusB offers insight into the mechanism by which FusB facilitates the uptake of ferredoxin through the

FusA receptor. This model will not only elucidate the specific roles of FusB oligomers but also contribute to the broader understanding of the transportation of atypically large substrates via TBDR systems in Gram-negative bacteria.

4.2 Materials and methods

4.2.1 Plasmids and bacterial strains

The *E. coli* strain BL21(DE3) (Invitrogen) was used as the host for expressing the FusB, AtFd2. For PM1 production, the competent cell *E. coli* strain BL21(DE3) pLysS (Invitrogen) was selected as describe previously.

To create the plasmid for recombinant FusB protein production, the gene encoding FusB from *Pectobacterium carotovorum* was identified from its complete genome (NCBI Reference Sequence: WP_138254891). The gene segment encoding the C-terminal domain (residues 224-324) was synthesized and inserted into the pET28a vector with an N-terminal His6-tag and a TEV protease cleavage sequence (Genscript).

The plasmids for producing recombinant AtFd2 and PM1 proteins were constructed as described previously in chapter 2.

4.2.2 Expression and purification for structural study and isothermal titration calorimetry measurement experiments

The AtFd2 and PM1 proteins were overexpressed and purified by the same protocols as presented in chapter 2.

To produce highly pure FusB, the *E.coli* BL21(DE3) host cells carrying the recombinant FusB plasmid was cultured in LB broth containing 50 μg/mL kanamycin. The cells were cultured until the OD_{600} reached to 0.6. The resulting culture was induced by IPTG

at the final concentration of 0.5 mM followed by continued growth at 20 ℃ for 16 hours. The cells were collected by centrifugation at 6000 rpm for 15 minutes. The pellet was resuspended in lysis buffer containing 50 mM Tris-HCl pH 7.5, 500 mM NaCl, 0.5 mg/mL lysozyme, and 0.1 mM PMSF. The cell resuspension was placed on ice and stirred magnetically, and then disrupted by sonicating for three times. The resulting lysate was centrifuged at 4℃ for 1 h at 32,000 rpm. The supernatant was collected and then loaded into the nickel open tubular column pre-equilibrated in buffer containing 50 mM Tris pH 7.5, 500 mM NaCl. The nickel beads bound with the desired protein was washed using 10 column volumes of buffers with imidazole concentrations of 10 mM, 20 mM, and 50 mM, respectively. The target protein was eluted using buffers containing imidazole concentrations of 250 mM and 500 mM, respectively. Subsequently, the samples in each faction were analyzed using SDS-PAGE. The sample eluted with buffer containing imidazole concentration of 250 mM were dialyzed against 50 mM Tris-HCl pH 7.5, 500 mM NaCl overnight. To remove the purification tag, the dialyzed sample in the addition of TEV protease with a 20:1 weight ratio of FusB:TEV was incubated at 20 ℃ for 2 hours. The TEV-treated sample was loaded into the nickel column again to remove the residual tag and tag-remaining FusB protein. The flowthrough was collected and concentrated using an Amicon Ultra-15 Centrifugal Filter Unit (10 kDa MWCO: Millipore). Then, the concentrated sample was purified by a HiLoad® 16/600 Superdex® 75 pg column (Cytiva) equilibrated in buffer containing 50 mM Tris pH 7.5, 500 mM NaCl. Subsequently, the fractions eluted within the desired peak were analyzed using SDS-PAGE. The eluted fractions containing FusB were concentrated to 30 mg/mL using the 10 kDa MWCO Amicon (Millipore) and stored at -80 ℃ for further structural study.

To prepare the FusB and PM1 proteins for ITC measurement experiments, the expression and purification of these proteins were performed in the similar way of those for structural study, with the exception of buffer compositions in the gel filtration chromatography. The buffer compositions for equilibration and elution were 20 mM sodium phosphate buffer pH 7.5, and 150 mM NaCl. Briefly, each protein was purified by a HiLoad® 16/600 Superdex® 75 pg column (Cytiva) equilibrated in this buffer. The purified proteins were concentrated to 0.28 mg/mL for FusB and 17.60 mg/mL for PM1.

4.2.3 Isothermal titration calorimetry (ITC) measurement experiments

For ITC measurements, proteins were prepared in 20 mM sodium phosphate pH7.5 and 150 mM NaCl. Measurements were performed using a VP-ITC instrument (MicroCal™, Malvern Instrument, UK) at 25 °C with stirring speed of 307 rpm. The syringe contained 480 μM of PM1 was titrated into 20 μM FusB in the ITC cell.

4.2.4 Analytical size exclusion chromatography of protein complexes

To evaluate the formation of stable complexes involving FusB and its partners, AtFd2 and PM1, FusB was mixed with each partner at a 2:1 molar ratio of FusA to the other proteins in a buffer consisting of 20 mM Tris-HCl and 150 mM NaCl. The mixture was subsequently incubated at 4 °C for 1 hour. The complex formations were analyzed using a S200 increase 10/300 GL column (Cytiva), which was pre-equilibrated with the same buffer employed for the complex formation.

4.2.5 Crystallization trials and optimization

The protein complexes between FusB with AtFd2/PM1 were generated by mixing FusB to AtFd2 or PM1 with a 1:2 molar ratio of FusB: ferredoxin/PM1. The mixtures were incubated at 4℃ for 1 hour before crystallization trial experiments. The initial crystallization screenings were performed in 96 well plate (Violamo, Osaka, Japan) using the sitting-drop vapor diffusion method. Crystallization droplets were generated by mosquito LCP technology (SPT Labtch) using 100 nL of the protein complex mixture and 100 nL of reservoir solution from commercial screening kits (~400 conditions of Crystal Screen™ 1&2, PEG/Ion Screen™ 1&2, PEGRx™ 1&2, and Index™: Hampton Research) at incubation temperatures of 4 ℃ and 20 ℃.

The crystallization plates for FusB:PM1 complex were set up and monitored for years but there were no crystals observed. On the other hand, the crystals of FusB:AtFd were observed in PEG/Ion Screen™ 48 (0.2 M Ammonium citrate dibasic (ACD), 20% (w/v) polyethylene glycol (PEG) 3,500 at 4 ℃. Optimization was carried out using the hanging-drop vapor-diffusion method by adjusting the concentrations of ACD and PEG 3,350. Crystallization droplets were prepared by mixing 1 μL of the protein complex with 1 μL of the reservoir solution on a siliconized cover slide (Matsunami, Osaka, Japan). These droplets were then equilibrated against 150 μL of the reservoir solution in a 48-well plate (HR3-275, Hampton Research).

The optimal crystallization condition for the FusB:AtFd2 complex, consisting of 0.35 M ACD and 19.0% (w/v) PEG 3,350, produced small rod-shaped crystals. Further optimization was carried out by altering the molar ratios of FusB to AtFd2. The ratios tested were 1:2, 1:1, 2:1, 3:1, and 5:1. Finally, the best crystals of FusB:AtFd2 was obtained at molar ratios of 2:1. The crystals were picked up by mounting loops and cryoprotected by soaking for a few seconds in the crystallization solutions plus 20% triethylene glycol before cryocooling in liquid N_2.

4.2.6 X-ray data collection and structure determination

X-ray diffraction experiment of each crystal was taken at the BL44XU beamline of the synchrotron facility SPring-8. The diffraction spots were collected by an EIGER X 16M detector using a synchrotron beam with a wavelength of 0.9000 Å. 1800 diffracted images of all datasets were collected from each crystal by rotating from 0 to 180º with an oscillation angle of 0.1º and an exposure time of 0.1 second per frame at 100 K.

The datasets obtained from the FusB:AtFd2 crystal was processed using Dials software[95]. The best dataset was used, and the structure was solved by molecular replacement with Phaser from the PHENIX package[73,74], using the structures of native FusB (PDB ID: 7zc8) and *Arabidopsis thaliana* ferredoxin (PDB ID: 1off) as templates. The model was then manually rebuilt and refined using *Coot* software [76] and the phenix.refine program[77],. Validation of the final refined structures was checked by using the wwPDB validation server.

4.2.7 Interdomain interaction analysis

The coordinate of the final refined structure of FusB:AtFd2 was applied to the DIMPLOT program in the LigPlot^{+} suite[78] for intermolecular interaction analysis.

4.3 Results

4.3.1 Protein purification and complex formations

The plasmid for producing the recombinant soluble C-terminal domain of FusB (residues 224-324) was transformed into *E.coli* BL21 (DE3) and cultured in LB medium supplemented with 50 μg/mL kanamycin. 0.5 mM IPTG was added to the cell culture with OD600 = 0.6-1.0 to induce protein expression at 20 ℃ for 16 hours. The expressed FusB was purified using Ni-IMAC column, TEV protease treatment, and then, size exclusion chromatography. The protein purity of the desired fractions after gel filtration were assessed by SDS-PAGE. The S75 10/600 gel filtration profile of purified FusB revealed two overlapping peaks, which corresponded to dimeric FusB in the first peak ($FusB_D$; fractions 14-19) and monomeric FusB in the second peak ($FusB_M$; fractions 20-25). These fractions exhibited high purity, exceeding 95% approximately, as shown in **Fig. 4.1**. Gel filtration profiles of re-injected samples from both peaks showed the similar results indicating that the purified FusB exists in equilibrium between dimeric and monomeric FusB in aqueous solution (results not shown). The eluted fractions were separately concentrated and the $FusB_D$ sample was used for further studies.

The complex formation of FusB:AtFd2 and FusB:PM1 were carried out in the buffer containing 20 mM Tris-HCl and 150 mM NaCl and analyzed by analytical size exclusion chromatography. The individual proteins, FusB, AtFd2 and PM1, were also analyzed in the same manner as controls. The analytical S200 10/30 gel filtration profiles monitored at wavelength of 280 nm and 330 nm were shown in **Fig. 4.2**. The absorption at 330 nm was used for monitoring protein containing the iron-sulfur cluster, AtFd2 and PM1. S75 10/30 gel

filtration profile of $FusB_D$ **(Fig. 4.2A)** was monitored only at 280 nm revealed two overlapping peaks corresponding to $FusB_D$ (retention volume (V_R) = 16.70 mL) and $FusB_M$ (V_R = 18.30 mL). These results are consistent with the chromatogram of purified FusB mentioned above as expected. The chromatogram features of AtFd2 **(Fig. 4.2B)** and PM1 **(Fig. 4.2C)** monitored at both 280 nm and 330 nm displayed the V_R at 17.30 mL and 16.30 mL, respectively.

The chromatogram profile of FusB:AtFd2 monitored at 280 nm **(Fig. 4.2D)** revealed two overlapping peaks at V_R = 16.30 mL and 18.30 mL, while when monitored at 330 nm, it showed only a single peak at V_R = 16.30 mL, which eluted faster than both $FusB_D$ and AtFd2. The shift of the front peak from 16.70 mL to 16.30 mL suggests the formation of a productive complex of FusB and AtFd2, consistent with the absorbance at 330 nm by the iron-sulfur cluster in AtFd2. Similarlty, the chromatogram of FusB:PM1 **(Fig. 4.2E)** revealed two peaks at V_R = 15.70 mL and 18.30 mL when monitored at 280 nm, whereas only a single peak at V_R of 18.30 mL was observed in monitoring at 330 nm. The faster elution of the front peak and its absorbance at 330 nm indicate the formation of a stable complex of FusB:PM1. In addition, the peak at 18.30 mL corresponding to $FusB_M$ in both samples showed no absorption at the wavelength of 330 nm, indicating either no binding or only weak interaction between $FusB_M$ and its partners, AtFd2 and PM1.

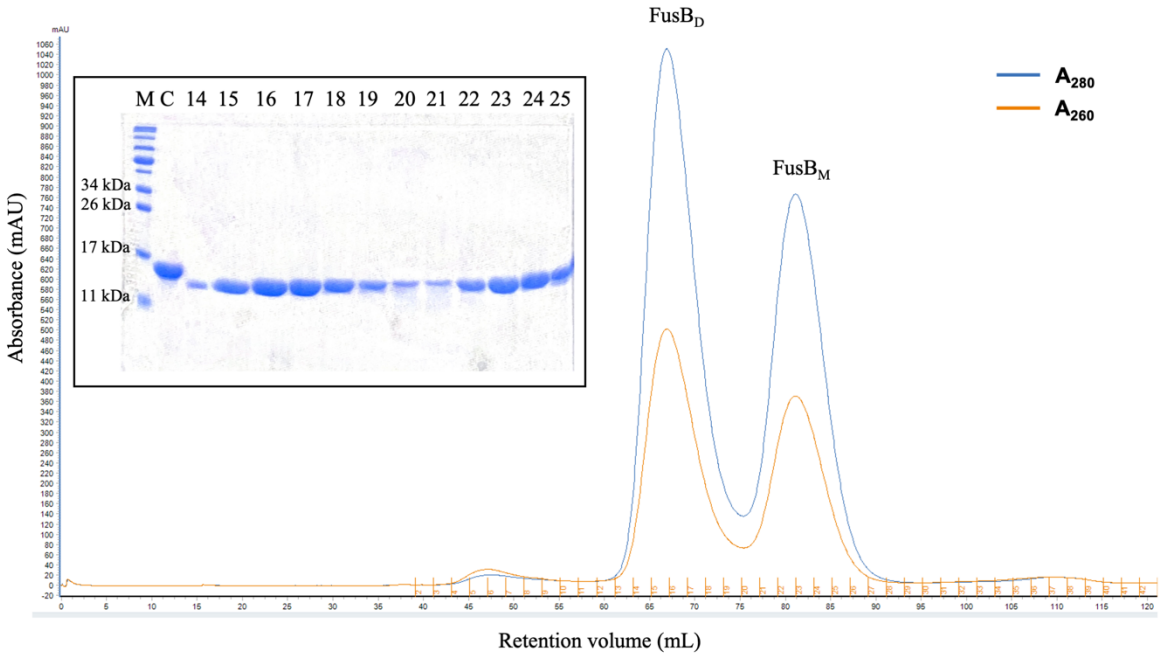

Figure 4.1 Purification of FusB by size exclusion chromatography. S75 10/600 gel filtration profile of purified FusB after TEV protease treatment monitored at wavelengths of 260 nm and 280 nm. Inset: SDS-PAGE analysis of concentrated FusB before gel filtration and the eluted samples of fractions 14–25.

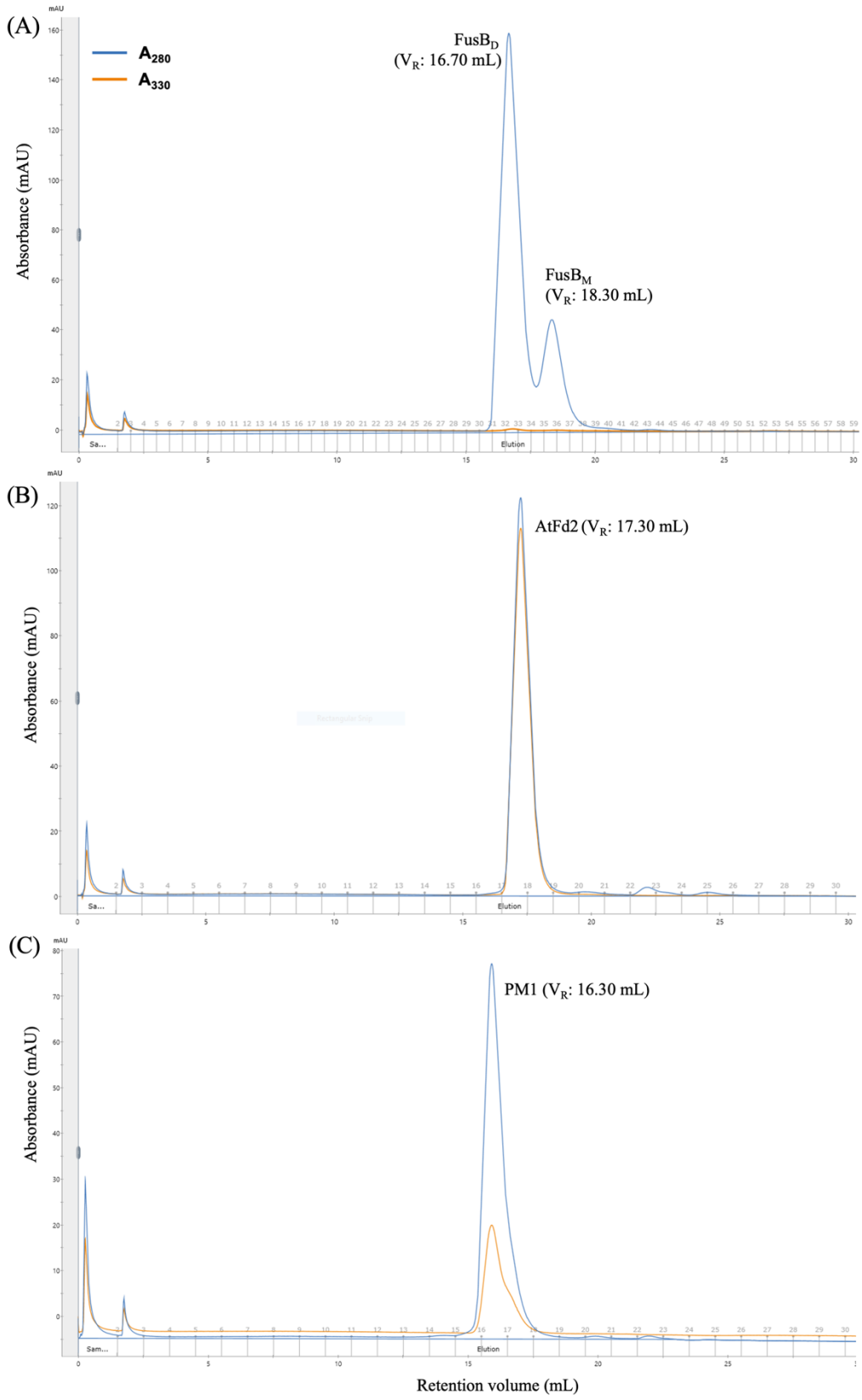
(A)
A280
A330
FusBD
(VR: 16.70 mL)
FusBM
(VR: 18.30 mL)
Absorbance (mAU)
(B)
AtFd2 (VR: 17.30 mL)
Absorbance (mAU)
(C)
PM1 (VR: 16.30 mL)
Absorbance (mAU)
Retention volume (mL)

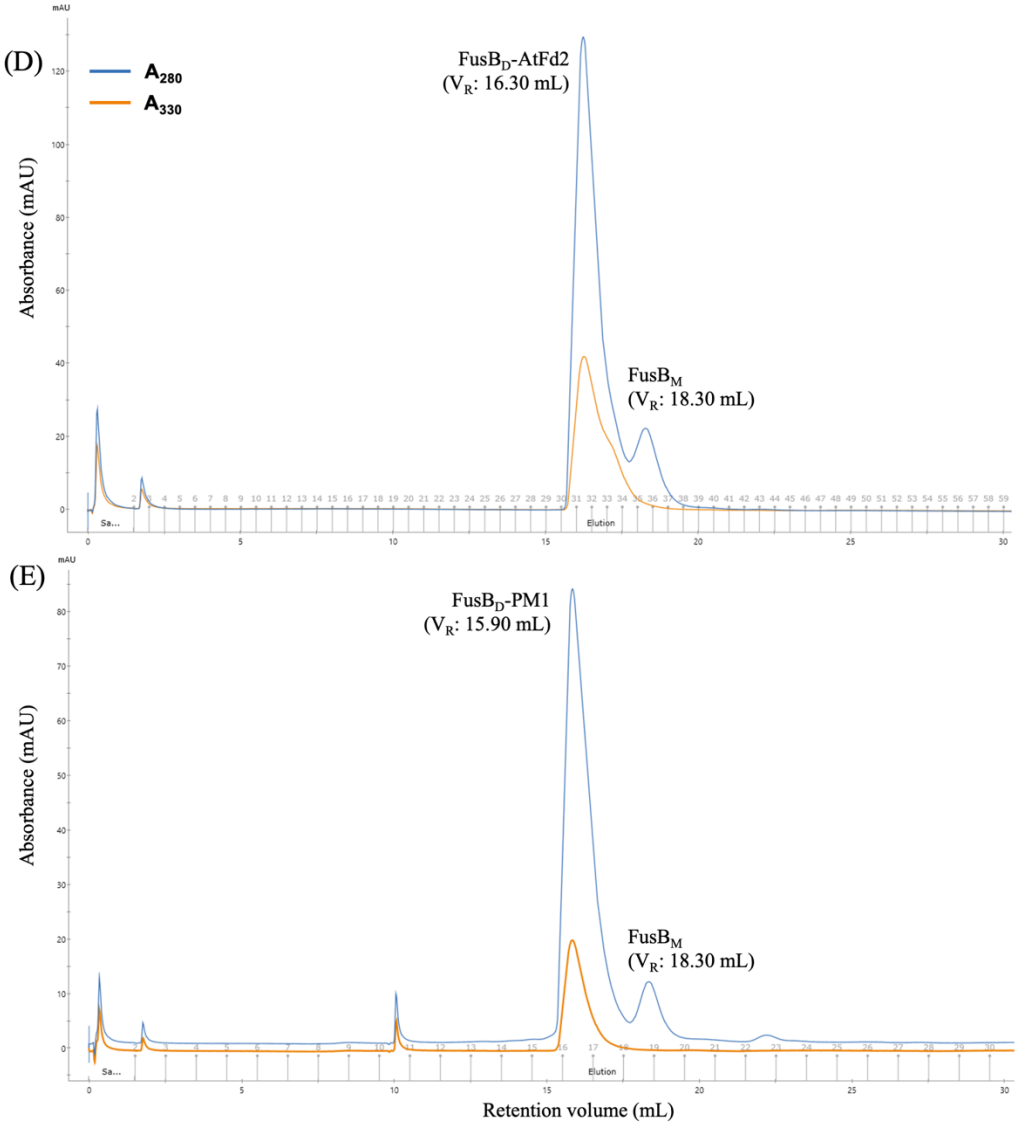

Figure 4.2 Assessment of FusB complexed with AtFd2 and PM1. S200 10/30 gel filtration profiles of individual **(A)** FusB, **(B)** AtFd2, **(C)** PM1, and complex reactions of **(D)** FusB:AtFd2 and **(E)** FusB:PM1 monitored at 280 nm and 330 nm.

4.3.2 Crystallization , optimization, data collection and structure solution

In crystallization trials of FusB:AtFd and FusB:PM1, the mixtures of FusB to other proteins at a 1:2 molar ratio were used for initial screening using commercial screening kits. Unfortunately, no crystals were obtained from crystallization plates of FusB:PM1. On the other hand, several tiny crystals of FusB:AtFd were observed in PEG/Ion Screen^{TM} 48 (0.2 M ammonium citrate dibasic (ACD), 20% (w/v) PEG 3,500) at 4 ℃ as indicated in the red circle of **Fig. 4.3A**. Initial optimization was performed using the hanging-drop vapor-diffusion method by adjusting the molar ratios of FusB to AtFd2 to produce large protein crystals **(Fig. 4.3B)**. The crystallization droplet of hanging-drop vapor-diffusion method, using a molar ratio of FusB :AtFd2 of 2:1, yielded larger and desired crystals **(Fig. 4.3C)**. Consequently, this ratio was utilized for further optimization. The second optimization step involved varying concentrations of ACD (0-0.5 M) and PEG 3,350 (10-30% w/v). Ultimately, large crystals of FusB:AtFd2 were obtained from a crystallization condition containing 0.35 M ACD and 19.0% (w/v) PEG 3,350, as depicted in **Fig. 4.3C**. The desired crystals were carefully selected and flash-cooled using the mother reservoir solution supplemented with 20% triethylene glycol as a cryoprotectant. Subsequently, the frozen crystals were stored in liquid nitrogen until diffraction data collection.

The X-ray diffraction images of FusB:AtFd2 crystals were taken at the BL44XU beamline of the synchrotron facility SPring-8 equipped with an EIGER X 16M detector. [13]The best dataset was used and the structure was solved by molecular replacement with Phaser from the PHENIX package[73,74], using the structures of native FusB (PDB: 7zc8) and *Arabidopsis thaliana* ferredoxin (PDB: 1off) as templates. The model was then manually

built and refined using Coot software [76] and the PHENIX.REFINE program [77] at the 2.80 Å resolutions. The final refined structure has the values of R_{work} and R_{free} of 0.2376 and 0.2907, respectively. The final crystallographic data and refinement statistics are shown in **Table 4.1**.

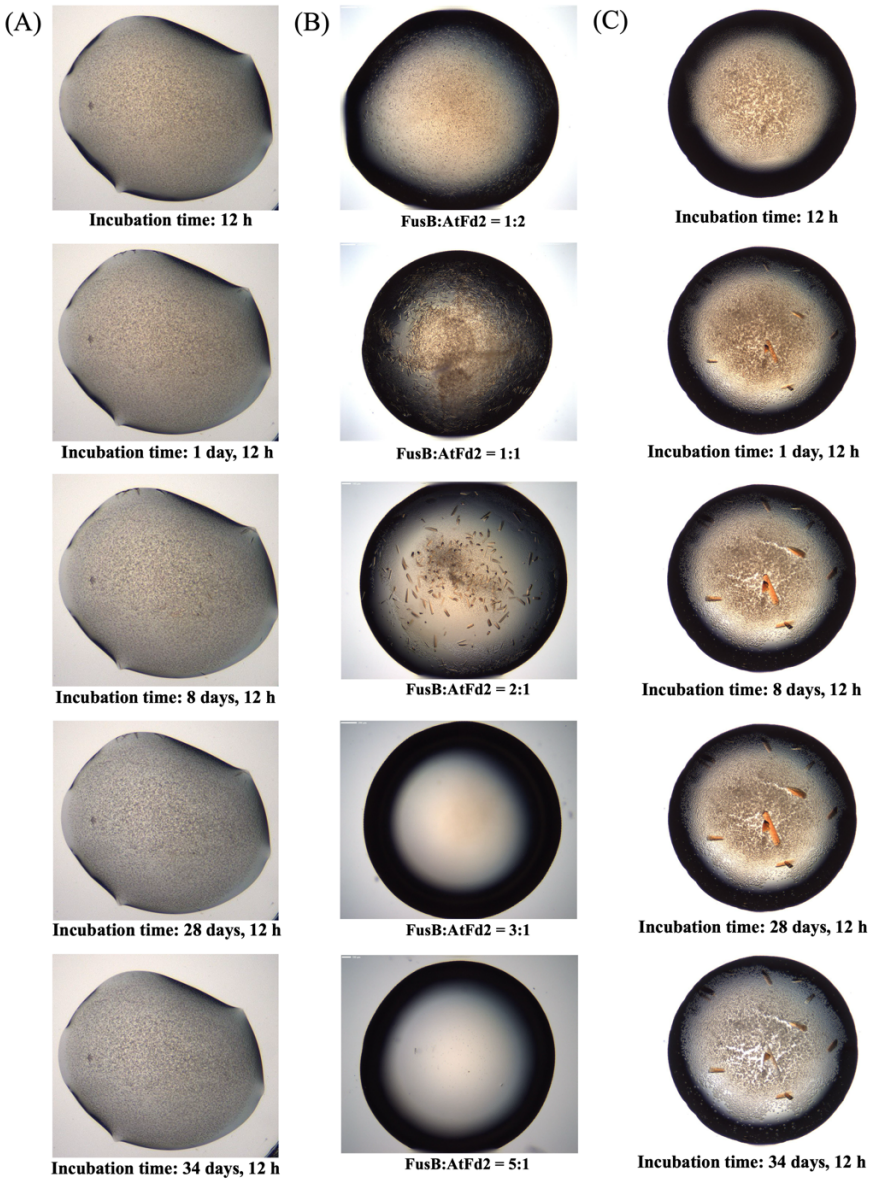

Figure 4.3 Crystallization trial and optimization of FusB:AtFd2 complex. **(A)** Crystallization trial of FusB:AtFd2 complex at 4 ℃ for different durations and **(B)** Variation in the molar ratios of FusB to AtFd2 at 4 ℃ for 8 days and 12 h observed in PEG/Ion Screen^{TM} 48 (0.2 M Ammonium citrate dibasic (ACD), 20% (w/v) polyethylene glycol (PEG) 3,500. **(C)** Optimization of the concentrations of PEG 3,350 and ACD in the PEG/Ion Screen^{TM} 48 condition carried out for various durations.

Table 4.1 Data collection and refinement statistics.

Data Collection	**Value**
Wavelength (Å)	0.90000
Resolution range (Å)	31.47 - 2.80 (2.90 - 2.80) [a]
Space group	$P2_1$
Unit cell (*a, b, c*, α, β, *γ*)	84.4209 154.787 91.5061 90 95.8671 90
Unique reflections	57428 (5720) [a]
Multiplicity	3.56 (3.73) [a]
Completeness (%)	99.81 (99.76) [a]
Mean *I*/sigma (*I*)	5.3 (0.5) [a]
Wilson B-factor (Å^2)	65.47
R-meas	0.177 (0.779) [a]
CC1/2	0.981 (0.558) [a]
Refinement	
Reflections used in refinement	57401 (5716) [a]
Reflections used for R-free	1964 (176) [a]
R-work/ *R*-free	0.2376 (0.3039)[a] /0.2907 (0.3389) [a]
No. of non-hydrogen atoms	11303
macromolecules	11279
ligands	24
solvent	0
Protein residues	1529
RMS (bonds, Å)	0.010
RMS (angles, º)	1.42
Ramachandran plot (%)	
Favored/ Allowed/ Outliers	94.05/ 4.06/1.89
Clash score	12.81
Average B-factor (Å^2)	72.95
macromolecules	73.01
ligands	48.45

[a] Statistics for the highest-resolution shell are shown in parentheses.

4.3.3 Crystal structure of FusB:AtFd2

The crystal structure of FusB:AtFd2 complex contains six molecules of FusB:AtFd2 complex per a crystallographic asymmetric unit as shown in **Fig. 4.4A**. Therefore, the non-crystallographic restraint was applied during the refinement process due to poor electron density map in some regions. Six FusB:AtFd2 molecules were not identical and formed a dimer of trimers (C1, C2, C3 and C4, C5, C6), each trimer of which was related by non-crystallographic pseudo twofold symmetry. However, no obvious rotational symmetry was found in each trimer. All FusB:AtFd2 complex contains dimeric FusB and monomeric AtFd2 **(Fig. 4.4B)**. The ratio of FusB to AtFd2 of 2:1 in the crystal structure is consistent with that analyzed by analytical size exclusion chromatography above. The r.m.s.d.(s) between Cα atoms in the complex molecule of FusB:AtFd2 is in the range from 0.329 to 0.616 Å.

Temperature factor putty models revealed large variation of the B-factors of each complex, ranging from 41.3 to 154.0 Å^2. AtFd2 was identified as the most ordered molecule in the complex based on the B-factors. The two FusB molecules hosting one AtFd2, one with lower B-factors of which was termed the rigid FusB ($FusB_{rig}$). Conversely, the other of FusB with higher B-factors was named as the flexible FusB ($FusB_{flex}$), most of which showed very flexible structure with larger B-factors. Specifically, the $FusB_{flex}$ showed lower B-values only in the 10 amino acids of the C-terminus and the higher values for the rest of molecule. These findings indicate that AtFd2 binding was stabilized by the $FusB_{rig}$ and the C-terminus of $FusB_{flex}$.

The recombinant FusB and AtFd2 proteins comprise 102 and 97 amino acids, respectively. The complete sequence of amino acid residues for AtFd2 was fully assigned to

the electron density map. In contrast, the $FusB_{rig}$ and $FusB_{flex}$ molecules missed first fourteen and twenty-four amino acids at N-terminal residues, respectively due to a high flexibility of this region[96,97]. Additionally, the loops of $FusB_{flex}$ extending away from the complex could not be fully modeled in all complex molecules except for C1 where these loops were completely modeled. Among each complex molecule, the model of complex C1 contained more structurally complete information than the others in the crystallographic asymmetric unit. I chose the complex C1 here after as a representative and described the crystal structure of FusB:AtFd2 by referring it to the FusB:AtFd2 complex **(Fig. 4.4B).**

The crystal structure of FusB:AtFd2 complex contains two molecules of FusB, $FusB_{rig}$ and $FusB_{flex}$, and one AtFd2. The three dimensions of this complex are 73.9 x 52.1 x 29.3 Å **(Fig. 4.4B)**. Oligomeric state of FusB molecules in this complex is a dimer formed by $FusB_{rig}$ and $FusB_{flex}$, which is like the previously reported structure of native dimeric FusB (PDB:7zc8) and TonB homologue[97]. The secondary structure elements of $FusB_{rig}$ are in the order of β1*-α1-β1-β2-α2-β2*-β3 whereas those of $FusB_{flex}$ are in the order of α1-β1-β2-α2-β3. Three β strands (β1, β2, β3) of $FusB_{rig}$ and β3 of $FusB_{flex}$ form a β-sheet, and the two strands of β1* and β2* form a separate small sheet. The $FusB_{rig}$ is mostly responsible for hosting AtFd2 molecule in its groove. The AtFd2 in the complex keep its secondary structure of β1-β2-α1-β3-α2-β4-α3, exhibiting a high similarity to that of single AtFd2 (PBD: 1off; residues 2-96; r.m.s.d. of Cα = 0.439 Å) (result not shown).

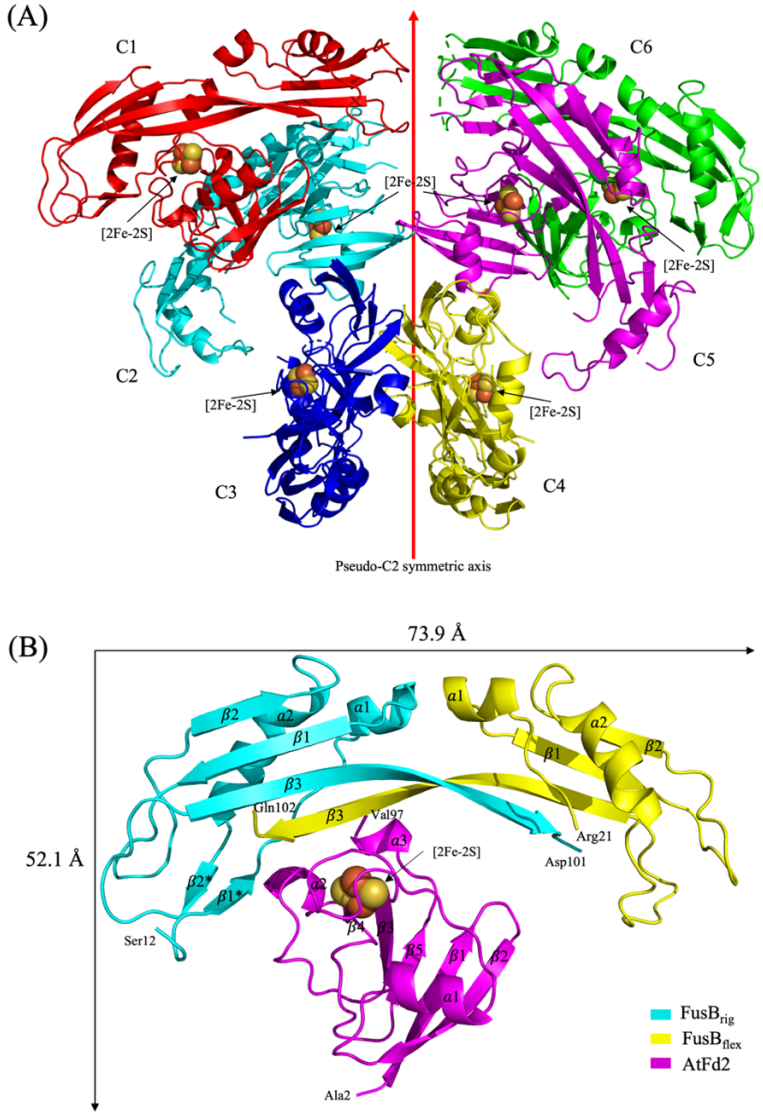

Figure 4.4 Overview of the FusB:AtFd2 crystal structure. (A) Representation of six FusB:AtFd2 complexes (C1 to C6) in the crystallographic asymmetric unit of $P2_1$ space group. FusB and AtFd2 are depicted in cartoons, and an iron-sulfur cluster is illustrated in spheres. Red arrow indicates the pseudo two-fold rotational axis. **(B)** Schematic depiction of the crystal structure of the C1 molecule of FusB:AtFd2 observed in the $P2_1$ space group. The ferredoxin domain is in magenta, $FusB_{rig}$ in cyan, and $FusB_{flex}$ in yellow. Spheres represent the iron-sulfur cluster.

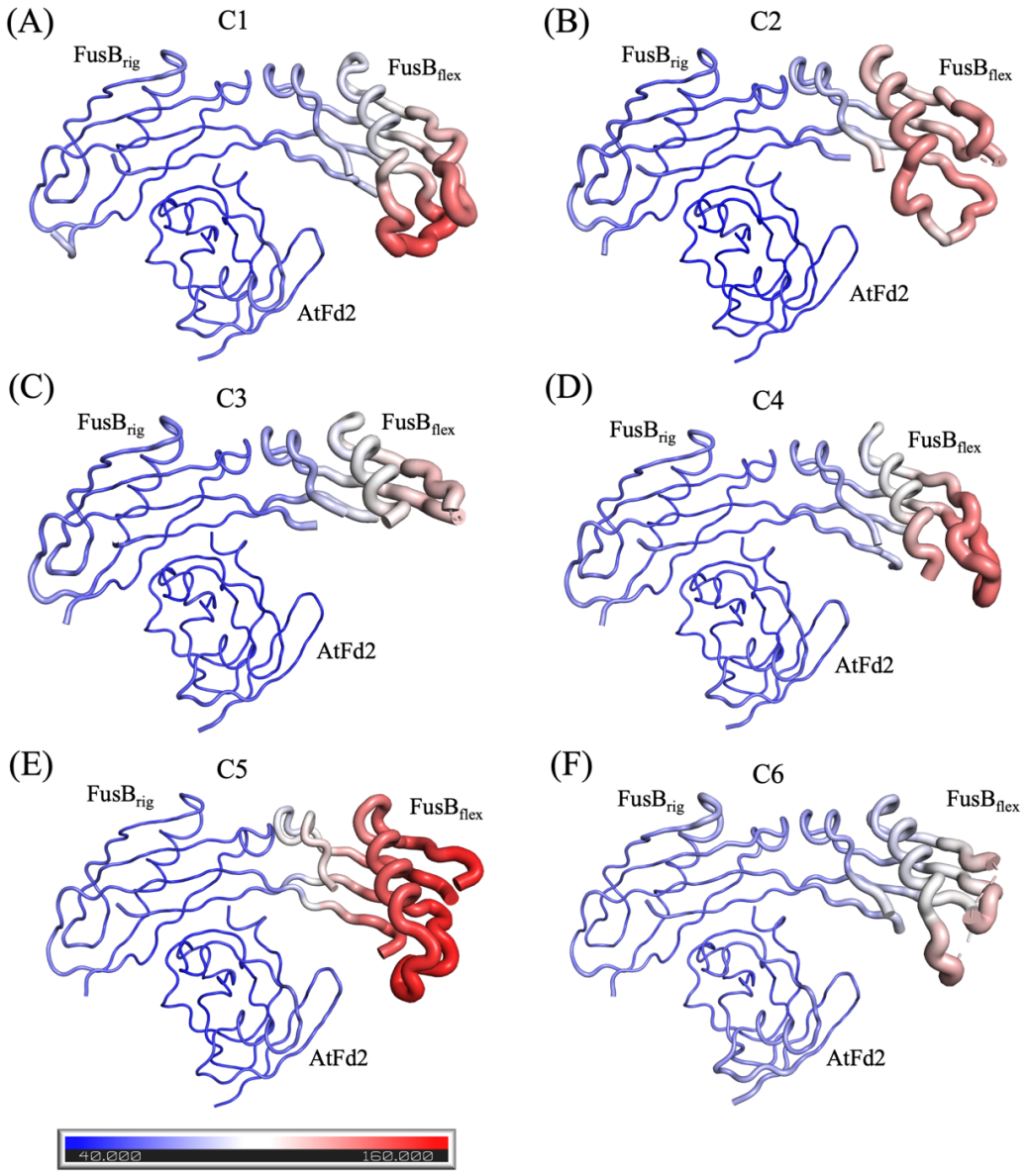

Figure 4.5 B-factor putty representations of each FusB:AtFd2 in the crystallographic asymmetric unit calculated by the B-factor putty program in PyMOL. Side views showing the B factors of FusB$_{rig}$, FusB$_{flex}$, and AtFd2 in each complex including **(A)** C1; complex1; **(B)** C2; complex2; **(C)** C3; complex3; **(D)** C4; complex4; **(E)** C5; complex5; **(F)** C6; complex6. The B-factor values are colored in a blue-white-red spectrum with a minimum value of 40 and a maximum value of 160 Å^2.

4.3.4 Intermolecular interactions of FusB and AtFd2

At the interface of the FusB:AtFd2 complex, extensive inter-domain interactions were observed **(Fig 4.6, and 4.7)**. Superimposition of $FusB_{rig}$ and each the dimeric FusB molecules without Fd (PDB: 7zc8) resulted in a r.m.s.d. value of 0.466 Å **(Fig. 4.6)** and 1.665 Å, respectively. I compared the interdomain interactions between FusB molecules in both of the complexed and Fd-free forms **(Fig. 4.6; top-right black dashed box)**. In the Fd-free form, the Lys16 (29) residue located on the α1 helix of each FusB molecule forms a salt bridge with Glu20 (34) and a hydrogen bond with Leu79 (93) of the other FusB (numbers for the corresponding residues in the complexed FusB molecules are indicated in parenthesis). Conversely, in the complexed state, these amino acids were too far from each other to form such interactions. These findings suggest that stabilizing the dimeric interfaces of FusB makes two FusB molecules more rigid. The absence of these interactions when forming a complex with Fd leads to high flexibility of one FusB molecule and become a $FusB_{flex}$ in the complex. The superimposition of $FusB_{rig}$ to the Fd-free FusB revealed a movement of $FusB_{flex}$ upon complex formation, resulting in a closure of the FusB groove with a rotation angle of 14.8º **(Fig. 4.6; bottom-right)**. These finding suggest that the flexibility of $FusB_{flex}$ in the complex is induced upon AtFd2 binding, as indicated by the high B-factor observed for the $FusB_{flex}$ **(Fig. 4.5)**. Additionally, dimeric state of FusB, both in its complexed and Fd-free forms, was also stabilized by antiparallel β-strands on the pseudo two-fold axis formed by seven residues (Ser88, Val90, Lys92, Asn94, His96, Val96, Asp100) from each β3 strand of two FusB molecules. The left panel of **Fig. 4.7** illustrates half of these symmetric interdomain interactions. Notably, a salt bridge interaction formed by Arg20 of $FusB_{rig}$ and

Asp101 of $FusB_{flex}$ was observed at the end of the antiparallel β-strands, potentially helping to stabilize the FusB dimer tightly.

The intermolecular interactions of AtFd2 to $FusB_{rig}$ and $FusB_{flex}$ were unveiled by the crystal structure in this work as shown in **Fig. 4.7**. AtFd2 utilizes the different surfaces to interact to each FusB. Five amino acid residues (Ser39, Ser44, Ser46, Ser47, and Glu93) located on the surface near the iron-sulfur cluster of AtFd2 extensively form hydrogen bonds and a salt bridge with four residues (His96, Ile97, Arg98, and Val99) on the β3 strand of $FusB_{flex}$ **(Fig. 4.7, left panel),** and other five residues (Ser60, Ser63, Leu65, Asp66, and Asp67) of ArFd2 form hydrogen bonds with three (Arg16, Arg20, and Arg21) of $FusB_{flex}$ **(Fig. 4.7, right panel)**. Interestingly, some of these residues of extended β3 strand of $FusB_{flex}$ also participated in formation of antiparallel β-sheet with the β3 strand of $FusB_{rig}$, as described above. In addition, the acidic AtFd2 molecule occupies a basic groove of $FusB_{rig}$ by forming salt bridges and hydrogen bonds with five residues (Ser60, Ser63, Leu65, Asp67, Asp67) of AtFd2 to four basic residues (Asp16, His19, Arg20, and Arg21) of $FusB_{rig}$. This bulk interaction likely contributes to the more rigid structure of $FusB_{rig}$ in the complex compared with $FusB_{flex}$, which is consistent with the low B-factors observed for this protomer. Remarkably, Arg20 of $FusB_{rig}$ is the only residue in this complex that forms intermolecular interactions with both of $FusB_{flex}$ and AtFd2. It forms a salt bridge with Asn101 of $FusB_{flex}$ and a hydrogen bond with Ser63 of AtFd2. This possibly imply its importance in the complex stabilization.

I also investigated the conformational changes of amino acid side chains participated in interaction of FusB:AtFd2 complex compared with those in the Fd-free form and single

AtFd2 structure **(Fig.4.8)**. No significant conformational changes were observed between the crystal structures of AtFd2, but obvious distortion of the Asp66 and Asp67 residues in AtFd2 within the complex was detected **(Fig.4.8A)**. This distortion likely occurs to avoid clashes of these amino acids and to facilitate their binding to His19 and Arg21 of $FusB_{rig}$, respectively. In contrast, the side chains of Arg16 and His19 of $FusB_{rig}$ in the complex showed significantly different conformations from those in the Fd-free form **(Fig. 4.8B)**. These changes are induced by binding to key residues of AtFd2 (Arg16 to Ser60; His19 to Leu65 and Asp67) during complex formation. Similarly, the side chain of Arg98 of $FusB_{flex}$ forms a hydrogen bond to Ser39 of AtFd2, resulting in its conformational change. The position of His96 is also slightly shifted from its position in Fd-free form to prevent residue clash and facilitate binding to Ser46 and Glu93 of AtFd2.

Analytical SEC analysis suggests that FusB directly interacts with both AtFd2 and PM1 in solution. Although extensive crystallization trials of FusB:PM1 complex were performed, no crystals were obtained in these attempts. To confirm the binding of PM1 to FusB, I further investigated the complex formation of FusB:PM1 with ITC by titrating PM1 to FusB solution as shown in **Fig. 4.9**. The obtained ITC thermogram **(Fig.4.9A)** showed the negative ITC peak for this binding, indicating exothermic reaction by releasing of heat. The binding isotherm **(Fig. 4.9B)** revealed that the interaction between FusB and PM1 is driven mainly by enthalpy, with contributions from entropy as well. The thermodynamic parameters of PM1 to FusB binding are K_d = 8.1 μM, ΔG = -6.9 kcal/mol, ΔH = -6.0 kcal/mol, and -$T\Delta S$= -0.9 kcal/mol. These parameters suggest that the complex formation of FusB:PM1 is a thermodynamically favored and spontaneous reaction. The large negative enthalpy

contribution in FusB:PM1 complex formation may reflect the release of heat following direct molecular binding at the protein surfaces, including intermolecular hydrogen bonds, salt bridges **(Fig. 4.7)**, and van der Waals interactions.

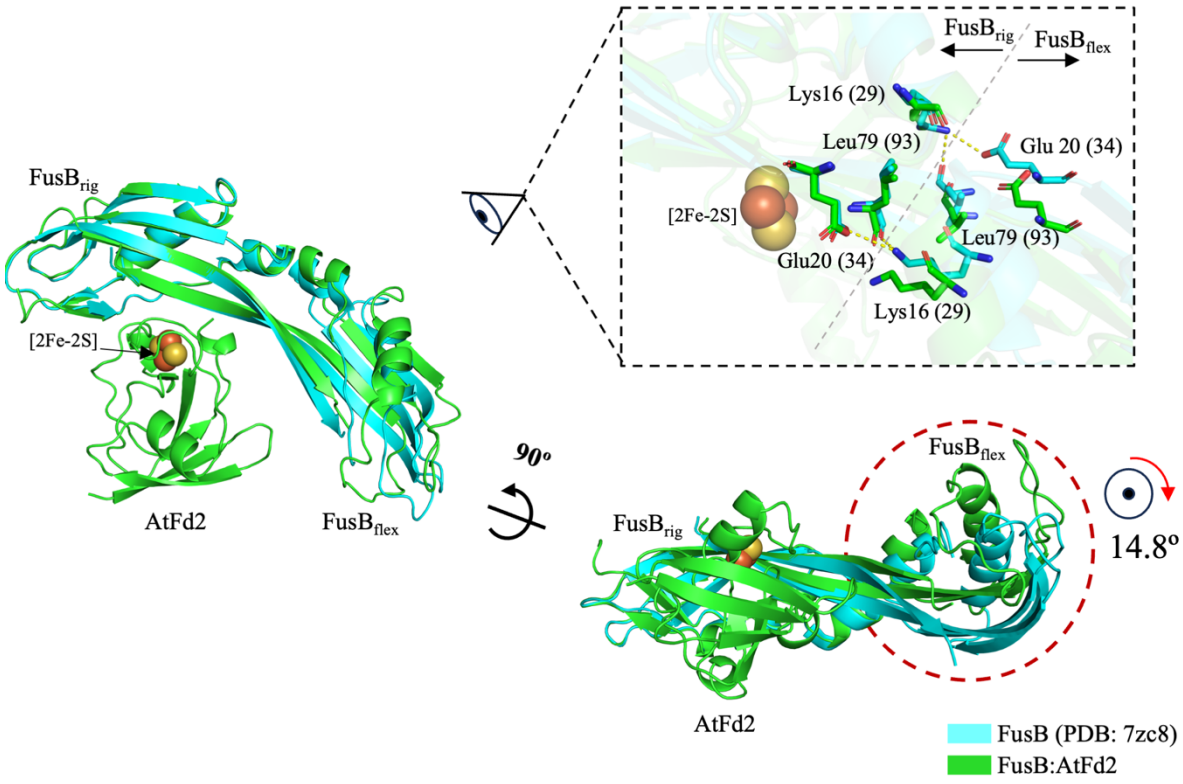

Figure 4.6 Comparison of domain movement of FusB$_{flex}$ in complex and in Fd-free form. The superimposition of FusB$_{rig}$ in FusB:AtFd2 with FusB (PDB: 7zc8) in its Fd-free form (residues 2-88; backbone r.m.s.d. 0.446). FusB and AtFd2 are depicted in cartoons, and an iron-sulfur cluster is shown in spheres. The amino acid residues involved in the dimer interaction of FusB are depicted as stick models in the top-right black dashed box. Amino acid numbers for the corresponding residues in FusB molecules in this work are indicated in parenthesis. The angle of rotational movement of FusB$_{flex}$ upon complex formation was calculated to be 14.8º using the PyMOL program, as shown in the bottom-right red dashed circle.

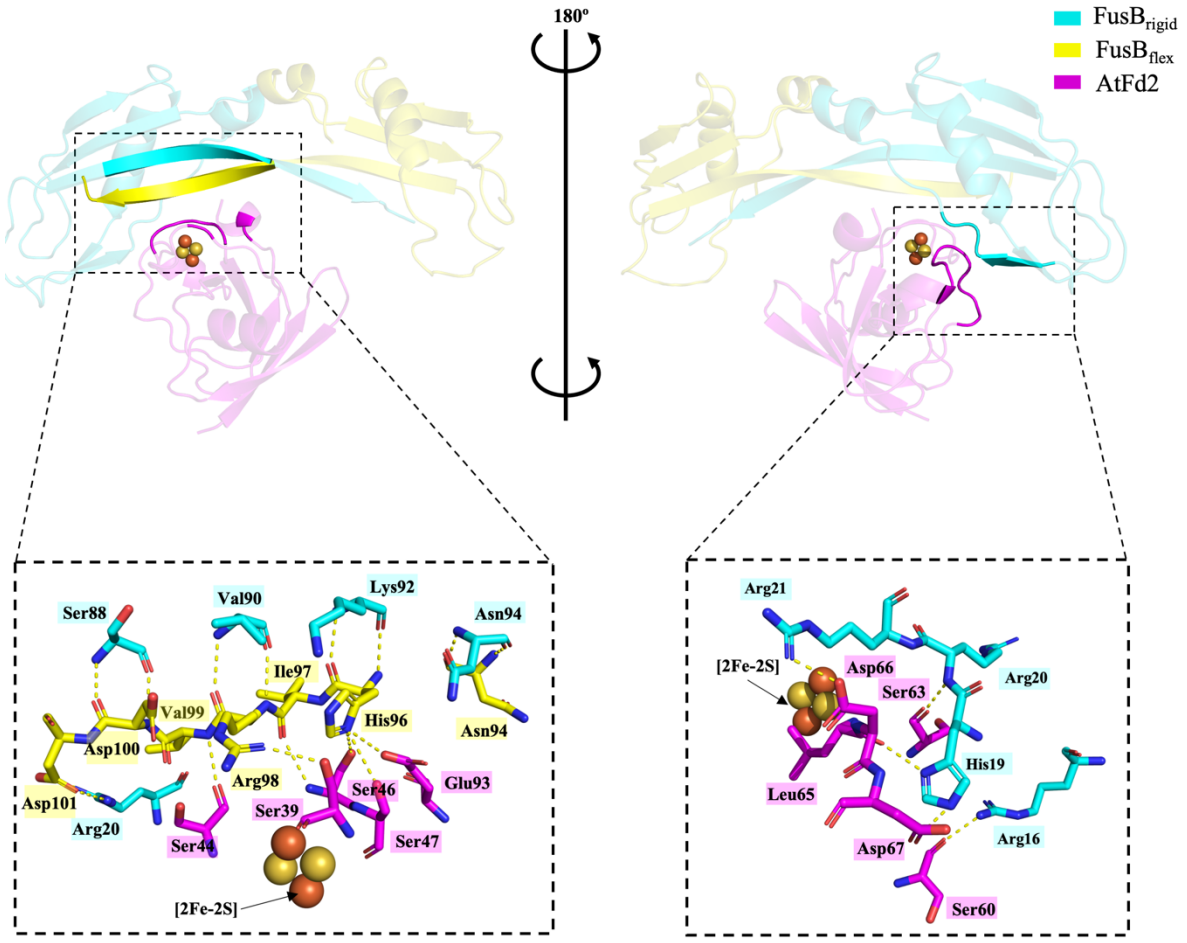

Figure 4.7 Interdomain interactions of FusB:AtFd2. Open-book representation of intermolecular interactions in crystal structure of FusB:AtFd2 investigated by LigPlot^{+}. The complex is depicted as transparent cartoon models, highlighting the key amino acids on secondary structures involved in intermolecular interactions with AtFd2 (magenta), FusB$_{rig}$ (cyan), and FusB$_{flex}$ (yellow). The magnified views highlighting the key amino acids of FusB:AtFd2 on both sides are presented within the black dashed boxes. The key residues are presented as stick models and an iron sulfur cluster is shown as spheres their bonds are shown as dashed lines.

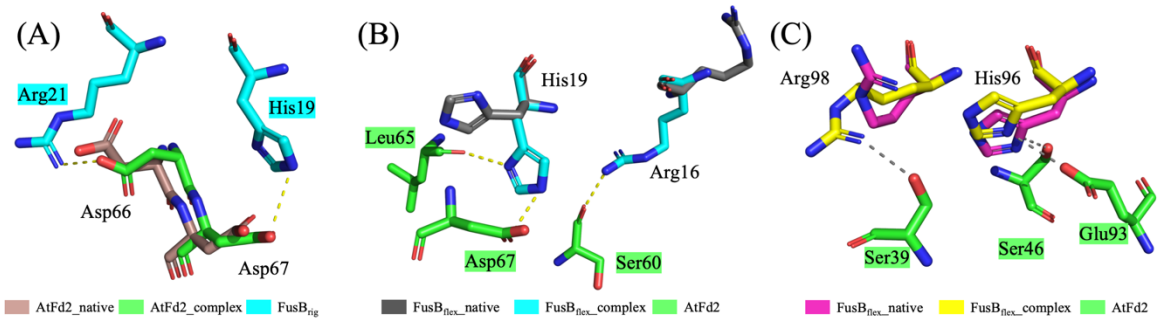

Figure 4.8 Conformation changes of key amino acids involved in intermolecular interactions of FusB:AtFd upon complex formation. (A) Schematic drawing of superimposition of key amino acids, Asp66 and Asp67, of AtFd2 in the complex (green) and single form (dark red) responsible for binding to His19 and Arg21 of $FusB_{rig}$ (cyan). **(B)** Schematic drawing of superimposition of key amino acids, His19 and Arg21, of $FusB_{rig}$ in the complex (cyan) and Fd-free form (grey) responsible for binding to Ser60, Leu65, and Asp67 of AtFd2 (green). **(C)** Schematic drawing of superimposition of key amino acids, Arg98 and His96, of $FusB_{flex}$ in the complex (yellow) and Fd-free form (magenta) responsible for binding to Ser39, Ser46, and Glu93 of AtFd2 (green). These amino acids are represented as stick models and their interactions are shown as dashed lines.

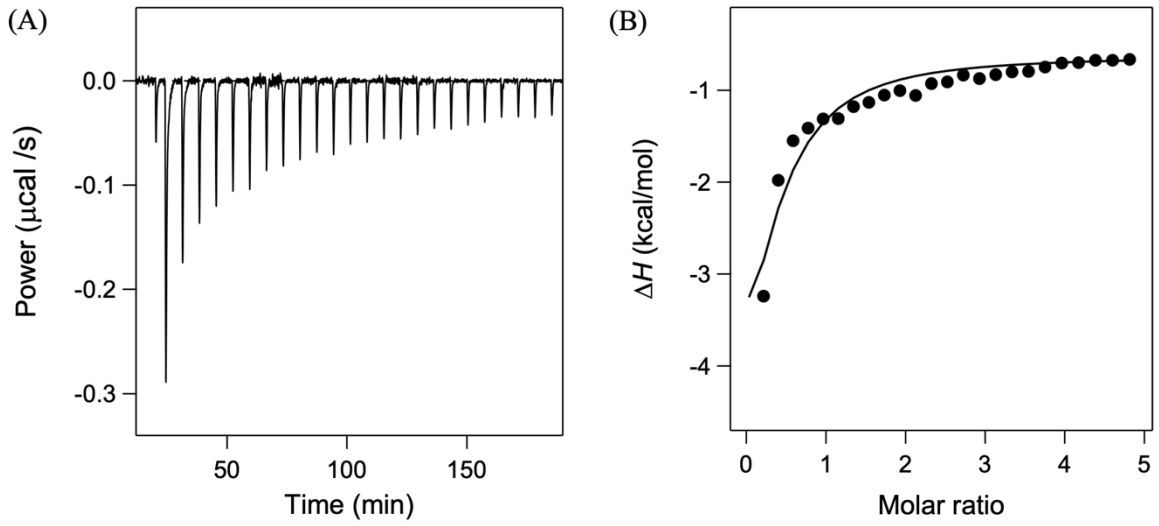

Figure 4.9 FusB interacts with PM1. (A) ITC thermograms of the titration of PM1 to FusB obtained at 25 ℃ under 20 mM sodium phosphate pH 7.5, 150 mM NaCl. (B) FusB:PM1 binding isotherms obtained from (A). The calculated values for FusB:PM1 complex are K_d = 8.1 µM, ΔG = -6.9 kcal/mol, ΔH = -6.0 kcal/mol, and $-T\Delta S$= -0.9 kcal/mol.

4.3.5 Comparison of non-redox and redox complexes of ferredoxins and their partners

In this section, I investigated the intermolecular interactions of electron transfer complex formation by plant-type ferredoxins and their redox partners in photosynthesis, ferredoxin-NADP+ reductase (FNR) and sulfite reductase (SiR), as well as those of non-redox partners of plant-type ferredoxin (AtFd2) and TonB-like FusB in the ferredoxin uptake system. The focus was the residues responsible for complex formation on the ferredoxin shared among all complex formation **(Fig. 4.10)**. Fd of FusB:AtFd2 utilized 6 unique residues (Ser44, Ser46, Ser47, Ser60, Leu65, and Glu93) in extensively binding to FusB molecules by forming salt bridge and hydrogen bonds **(Fig. 4.10A; green sticks)**. For comparison with FusB:AtFd2 (**Fig. 4.10B)** in this study, the complexes of *Zea mays* ferredoxin with SiR[33] (SiR:Fd; PDB: 5h8y; **Fig. 4.10C**) and that with FNR[32] (FNR:Fd ; PDB: 1gaq**; Fig. 4.10D**) were selected. Interestingly, four key residues (Ser39, Ser63, Asp66, and Asp67) were shared among the Fd domain in the FusB:AtFd2 and FNR:Fd complexes for interdomain interactions with their partners. Three of the four residues (Ser63, Asp66, and Asp67) were observed only in these two complexes, not in SiR:Fd **(Fig. 4.10A; cyan sticks)**. The Fd molecule in FusB:AtFd2 shared only one residue, Ser39, for intermolecular interactions with SiR:Fd complex **(Fig. 4.10A; blue stick)**. Probably, Ser39 of Fd found in all three intermolecular interactions may be crucial in complex formation as well as possibly important in biological function. Based on these findings, the binding characteristics of Fd in FusB:AtFd2 complex formation in this work are more similar to those in FNR:Fd than to those in SiR:Fd.

Thermodynamical basis on formation of FNR:Fd[35] and SiR:Fd[34] complexes at various conditions was determined. The FNR:Fd binding is an endothermic reaction, driven primarily by entropy, while the SiR:Fd binding is an exothermic reaction, driven mainly by enthalpy. The characteristic of enthalpy-driven formation of the FusB and PM1 complex is more similar to that of SiR:Fd than FNR:Fd, with enthalpy being a more crucial factor than entropy in controlling interprotein affinity.

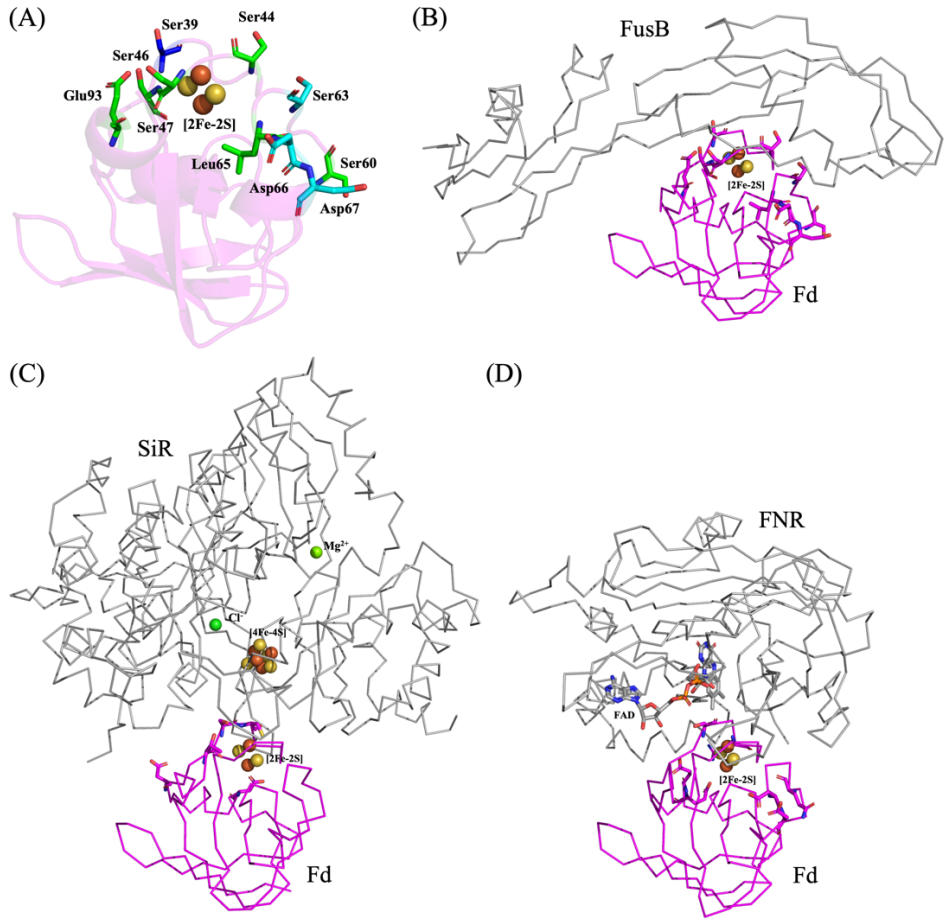

Figure 4.9 Ferredoxins form diverse intermolecular interactions to their redox and non-redox partners. (A) Ferredoxin in the FusB:AtFd2 complex, depicted as a cartoon model, shares interacting residues with those in the FNR:Fd and SiR:Fd complexes. The interacting residues of Fd in FusB:AtFd2 are represented as stick models, with unique residues shown in green, interreacting residues shared with Fd in only FNR:Fd in cyan, and interacting residues shared with Fd in both FNR:Fd and SiR:Fd in blue. Ferredoxins complexed with their partners, including **(B)** FusB, **(C)** SiR, and **(D)** FNR, are presented as ribbon models. The residues on each Fd responsible for interdomain interactions are shown as stick models. Iron-sulfur clusters, Mg^{2+}, and Cl^{-} are depicted as spheres, and FAD is shown as sticks.

4.3.6 Binding interfaces of ferredoxin with its partners in ferredoxin uptake system (Fus)

Iron-containing ferredoxin interacts with its receptor proteins of ferredoxin uptake system (Fus)[14,37,98]. The binding interfaces of ferredoxin responsible for binding to these proteins in Fus need to be investigated to understand whether binding manner is consistent or not in Fus. I selected the crystal structure of FusB:AtFd2 in this work and the docking model of FusA:AtFd2 based on NMR data in the previous report[14] for analysis. Based on these structures, I assigned the binding surfaces on ferredoxin with labeling residues responsible for binding to FusA in blue and FusB in red as shown in **Fig. 4.11A**. Ferredoxin interacts to extracellular loops and plug domain of FusA by using its back side away from the iron-sulfur cluster **(Fig. 4.11B)** whereas the key residues located on the front side near the iron-sulfur cluster are responsible for binding to FusB molecules **(Fig. 4.11C)**. Notably, the key residues on ferredoxin responsible for intermolecular interactions with FusA or FusB are distinct, with no overlap observed. Even the superimposition of the ferredoxin domains of both complexes showed no structural clashes between FusA and FusB but binding could occur sequentially (result not shown).

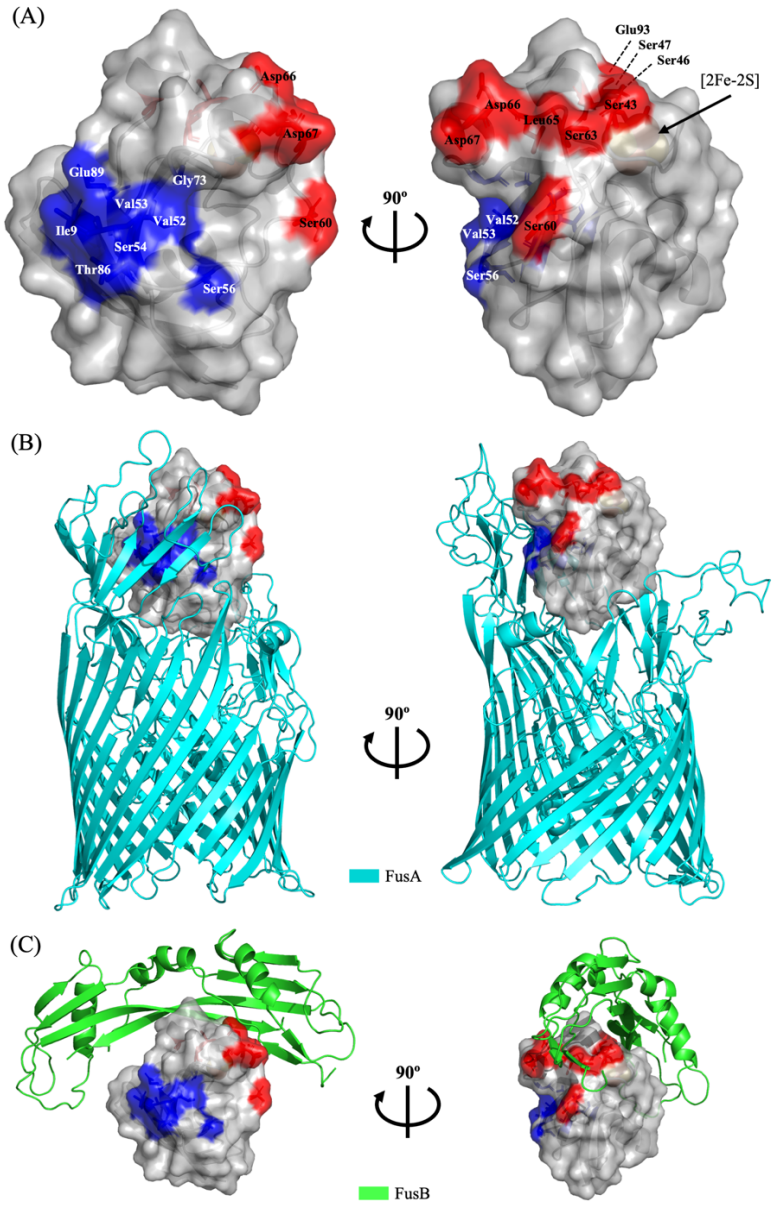

Figure 4.11 Structures of Fus proteins complexed with AtFd2 in ferredoxin uptake system. (A) Surface representation of AtFd2 highlighted FusA's interacting residues in blue surfaces (white labels) and FusB's interacting residues in red surfaces (black labels). **(B)** Superimposition of AtFd2 domain in **(A)** to a cyan cartoon model of FusA:AtFd2 obtained from chapter 3. **(C)** Crystal structure of FusB:AtFd2 showing the AtFd2 from the same orientation to **(A)** and **(B)**, and FusB in a green cartoon model.

4.3.7 Possible complex structure of FusB:PM

Pectocin M bacteriocins, produced by *Pectobacterium* species to eliminate closely related bacteria, contain a ferredoxin-like domain that shares amino acid sequence similarity of more than 60% with plant-type ferredoxins[14,21]. This domain enables PM to parasitize the ferredoxin uptake system of susceptible cells, thereby exerting its lethal actions. Interactions of the ferredoxin domain of PM with Fus proteins in the ferredoxin uptake system, including FusA[14] and FusB[37], have been reported. In this chapter, I confirmed the formation of productive complex of FusB:PM1 using analytical size exclusion chromatography as explained above. However, no crystal structure of FusB:PM1 was obtained despite the extensive crystallization trials on this complex. Consequently, I superimposed the ferredoxin domain in the determined FusB:AtFd2 complex with diverse conformations of PM as shown in **Fig. 4.12**.

Superimposing ferredoxin domains of PM to AtFd2 in FusB:AtFd2 shows low r.m.s.d values ranging from 0.635 to 0.674, indicating high similarity in the 3D structures of these domains. Notably, α helical linker of PM and FusB molecules had no clashes in all superimposed models of FusB:PM complexes, FusB:PM1 in the closed from, FusB:PM2 in the compact form, and FusB:PM2 in the open form. However, the model of FusB with PM1 in the closed form revealed clashes of amino acids in the 75-85 loop of $FusB_{flex}$ with the catalytic domain of PM1 **(Fig. 4.12A)**. Furthermore, this loop is positioned over the active site of the catalytic domain of PM1, thereby preventing substrate access to the active site. Therefore, it is necessary to rearrange the catalytic domain of PM1 *via* movement of the α-helix linker to facilitate the substrate binding and avoid these clashes. Conversely, in the models of FusB complexed with PM in the compact **(Fig. 4.12B)** or open form **(Fig. 4.12C)**,

no structure collisions were observed between FusB and the catalytic domain of PM. Moreover, the active site of PM in these models is clearly exposed to the environment, allowing substrate access to the active site.

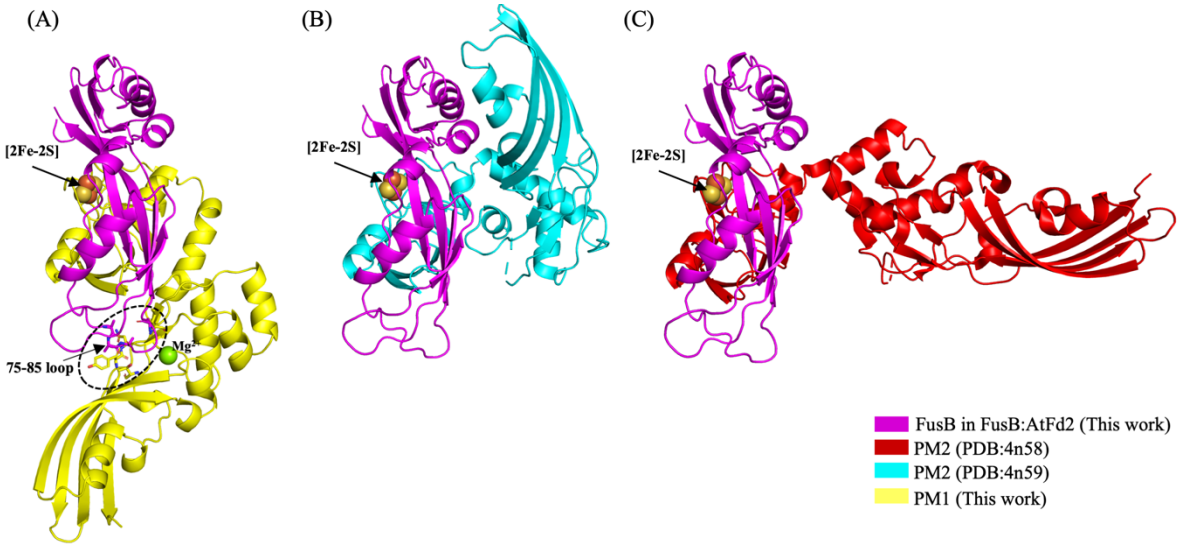

Figure 4.12 Possible models of FusB complexed with diverse conformations of pectocin M. Superimposition of the ferredoxin domain of the FusA:AtFd2 complex obtained in this work with that of the different conformations of PM including **(A)** PM1 in the closed form (this work; residues 2-96; r.m.s.d.= 0.674), **(B)** PM2 in the open form(PDB: 4n58; residues 2-96; r.m.s.d.=0.637), and **(C)** PM2 in the compact form (PDB: 4n59; residues 2-96; r.m.s.d.= 0.635). Clashes of amino acids within the 75-85 loop of $FusB_{flex}$ (residues Glu79, Ala80, Pro81, and Asn84) and the catalytic domain of PM1 (residues Thr196, Tyr220, Asn221, and Leu223) shown as stick models in **(A)** are indicated by a dashed black circle.

4.4 Discussion

Gram-negative bacteria inhabiting iron-limiting environments have developed specialized outer membrane receptors belonging to the TBDR family for facilitating the uptake of microbial iron-siderophores and iron-containing host proteins[24]. *Pectobacterium* ssp. utilize TonB dependent receptor FusA for importing ferredoxins or ferredoxin-containing bacteriocins[14]. In addition to FusA receptor, the Ton complex including TonB-like FusB, ExbB, and ExbD, anchored in the inner membrane, is required to facilitate ferredoxin entry. This complex achieves transport of ferredoxin/pectocin M by removing the plug domain that occupies the lumen of FusA and providing proton motive force (PMF) to drive the transport process. A better understanding of the mechanisms involved in ferredoxin uptake *via* this Fus system has been developed through the accumulation of structural and biological information on ferredoxin and its protein partners[14,37,38,98]. Importantly, the formation of a productive complex between TonB-like FusB and ferredoxin has been confirmed through analytical SEC analysis. Additionally, a mechanism detailing the complex of FusB and ferredoxin has been proposed[37], but the details regarding how FusB interacts with ferredoxin/PM during the uptake process remained unclear due to the absence of an atomic resolution structure of this complex. Therefore, in this chapter, I utilized X-ray crystallography coupled with isothermal titration calorimetry technique to study the interactions and structural information of the complex between FusB and ferredoxin/PM1. This approach provided insights into the intermolecular interactions between FusB and ferredoxin/PM1, developing a more precise mechanism of ferredoxin uptake system.

I investigated the interactions of FusB and AtFd2 in both solution and crystalline phases. Analytical SEC analysis of the soluble purified FusB domain (residues 224-324) in this work revealed the presence of both dimeric and monomeric states in aqueous solution. Re-injection of dimeric FusB produced a chromatogram feature similar to that of the starting sample. These results indicate the reversible oligomerization of FusB in equilibrium yielded a mixture of dimeric and monomeric forms. In contrast, only one oligomeric state of FusB, which can form a productive complex with ferredoxin, was reported in the previously studied FusB[37]. This difference is potentially due to variations in the length of acidic residues at the N-terminus of TonB proteins, where the presence of longer N-terminal residues leads to a shift in their oligomeric state from dimer to monomer in solution. However, full-length TonB, which includes the transmembrane part, can also form dimers or multimers[51,52].

Biological functions of dimeric and monomeric TonB were previously discussed[24,48]. The dimeric TonB with LysM motifs interacts with peptidoglycan and TonB-independent outer membrane receptor (e.g. OmpA), allowing its localization near the periplasmic interface of the outer membrane bilayer to finds ligand-bound receptor proteins[48,49]. However, the homodimeric form of TonB does not represent the form of TonB that binds to the transporters[48,50–52]. This unaccounted function of TonB in its dimeric form is fulfilled by its monomeric form, wherein the C-terminal sequence of monomeric TonB interacts with the TonB box sequence of TBDR to form an interprotein β-sheet through strand exchange[53–56]. Previously, the interaction between ferredoxin and FusB was reported, but the oligomeric state of FusB involved in this interaction remained unknown[37]. Remarkably, in this study, I uncovered an additional biological function of dimeric TonB-like FusB against ferredoxins

using analytical SEC analysis coupled with X-ray crystallography. These findings revealed that the FusB dimer strongly forms stable complexes with both AtFd2 and PM1 in solution, whereas its monomer cannot bind to these molecules **(Fig. 4.2)**. Monomeric FusB, like other TonB proteins, potentially plays a crucial role in binding to the plug domain of the TBDR FusA. This interaction facilitates the dislocation or melting of the plug domain into the periplasmic space, enabling ferredoxin translocation through the FusA lumen using energy from PMF generated by the ExbBD complex. In the subsequent step, dimeric FusB hosts the translocated ferredoxin molecule using its basic groove, inducing conformational changes in amino acids of FusB dimer and promoting flexibility of the unoccupied $FusB_{flex}$ to form a productive complex, as depicted in **Fig. 4.4B, 4.5, and 4.8**. These findings support the hypothesis that the monomer-dimer transition of TonB proteins serves distinct functions in facilitating the uptake of their substrates into the cell[48,50,99]. The next step involves FusC, an M16 protease existing in dimeric form, digesting ferredoxin in the periplasm to provide iron for cellular use. The dimeric structure of FusB exhibits flexibility of monomerization in solution and undergoes conformational changes upon binding to ferredoxin[38]. Consequently, I proposed the relationship between FusB and FusC based on the similarity in their dimeric state in active form and the flexibility of their structures upon ferredoxin binding. The binding of ferredoxin to the FusB dimer induces flexibility in the FusB structure, enabling this complex to locate and interact with the vacant dimeric FusC in the periplasmic space. The ferredoxin is transferred to FusC through conformational changes in the formed supramolecular complex, resulting in the digestion of ferredoxin by FusC and ultimately releasing iron for cellular utilization.

Alongside ExbBD complex, TonB proteins are involved in the full- or partial removal of the plug domain from the lumen of their specific receptors, facilitating the substrate uptake[57,100,101]. Additionally, TonB proteins have been observed to directly interact with their specific substrates, particularly with unusually large substrates such as colicin[42,47], pyocin[57], ferredoxin[37], and pectocin M1 (this study) in comparison to the well-studied siderophore substrates in the Ton system. Unlike colicin and pyocin, where TonB directly interacts with their IUTD within the TBDR lumen, TonB-like FusB in this study interacts directly with the folded ferredoxin domains of AtFd2 and PM1 without any assistance from the FusA lumen. This suggests that ferredoxin and pectocin M could possibly traverse across the FusA lumen without undergoing melting or partial unfolding, which is consistent with the results in chapter 3 and the previous reports[14,21].

The intermolecular interactions of FusB:AtFd2 were stabilized by extensive contacts, including hydrogen bonds and salt bridges **(Fig 4.7)**. Binding of homodimeric FusB to AtFd2 results in increased flexibility in $FusB_{flex}$ due to the loss of interactions at the dimer interfaces, which also induces conformational changes in key residues. Among these residues, mutating FusB at arginine positions 176 and 177 to lysine (corresponding to arginine positions 220 and 221 in this study) destroyed the binding ability of FusB to ferredoxin[37]. The crystal structure in my work revealed that these two residues in $FusB_{rig}$ are crucial for forming strong intermolecular contacts, including hydrogen bonds and salt bridges. Notably, the Arg20 residue forms a hydrogen bond with AtFd2 and a salt bridge with $FusB_{flex}$. Changing arginine to lysine results in a shorter side chain[37], leading to the loss of these critical contacts and ultimately disrupting the complex formation.

Ferredoxin can interact widely to redox- and non-redox protein partners in photosynthesis[36] and ferredoxin uptake system [14,37,38]. Comparison of intermolecular interactions of FusB:AtFd2 with well-characterized complexes of FNR:Fd and SiR:Fd revealed that interacting residues on ferredoxin in this complex (FusB:AtFd2) share higher similarity to those in FNR:Fd more than those in SiR:Fd. Even though the interacting residues involved in intermolecular interactions of the FusB and ferredoxin complex share greater similarity with those of FNR:Fd than SiR:Fd, the energy-driven complex formation of the FusB and ferredoxin is more similar to that of SiR:Fd, with enthalpy being a more crucial factor than entropy in controlling interprotein affinity. Although there are significant similarities in the intermolecular contacts of the ferredoxin complexed with FusB and FNR, the endothermic entropy-driven complex formation of the FNR:Fd is likely important for its enzymatic reaction[34]. In contrast, no such enzymatic reaction occurs with the FusB and ferredoxin complex, where the exothermic enthalpy-driven complex formation is more favorable for facilitating ferredoxin uptake.

The binding site of ferredoxin in the FusA and ferredoxin complex is located on the backside, away from the iron-sulfur cluster, as reported in the chapter 3 and literature[14]. A molecular surface of ferredoxin mapping key residues responsible for binding to FusA and FusB in my work reveals the reasonable and distinct binding interfaces for both protein partners without structural clashes of FusA and FusB. This suggests that the binding of ferredoxin to FusA and FusB could occur either sequentially or concurrently.

In chapter 3, I proposed that the domain rearrangement of pectocin M adopts an elongated conformation to avoid structural clashes between PM and FusA. This proposal is

consistent with the high flexibility of PM2[21]. Superimposition of the ferredoxin molecule in FusB:AtFd2 complex with various conformations of PMs revealed overlapping amino acids between the loop (75-85) of $FusB_{rig}$ and the catalytic domain of PM1. This structural clashes also may prevent the active site of PM1 from accessing its substrates. These findings support the hypothesis that the domain rearrangement of PM is crucial both to avoid clashes with its protein partners and to facilitate its translocation in the ferredoxin uptake system.

FusB plays crucial roles in interacting not only with the TonB box, recognition sequence for TonB proteins, of FusA but also with ferredoxin[37]. These two proteins, FusA and FusB, are necessary in facilitating the traverse of intact ferredoxin across FusA lumen. Although numerous TonB systems have been investigated, the Fus system is the only system in which a TonB protein has been shown to directly interact with the substrate without any assistance from a TBDR[37]. Consistent with these, in this work, I found that FusB, in its homodimeric form rather than as a monomer, is responsible for this function. This additional function of homodimeric FusB potentially facilitates the uptake of intact ferredoxin without denaturing or partial melting across the FusA lumen. It then transfers the intact ferredoxin to the M16 protease FusC, where the ferredoxin is proteolytically digested to release the iron-sulfur cluster necessary for bacterial survival. Additionally, I successfully identified the intermolecular contacts of AtFd2 with homodimeric FusB. Based on my findings in this work, I have developed the ferredoxin uptake mechanism *via* ferredoxin uptake system in *P. carotovorum* as shown in **Fig. 4.13**. In my proposed mechanism, distinct oligomers of FusB are responsible for different biological functions. In this model, in the resting state without ferredoxin substrate, FusA lumen is occluded with a plug domain to prevent nonspecific-substrate influx. FusB adopts a dimer form, which facilitates its interaction with

peptidoglycan and TonB-independent outer membrane receptors, enabling its localization near the periplasmic interface of the outer membrane bilayer. This positioning allows FusB to locate ligand-bound receptor proteins effectively. Once ferredoxin reaches the extracellular loops and plug domain of FusA, binding occurs on the side opposite to the iron-sulfur cluster. This interaction results in the TonB box sequence being released into the periplasmic space, where it is subsequently bound by monomeric FusB. Because of similar dimensions of FusA lumen and the globular ferredoxin, it is improbable that intact ferredoxin can easily diffuse across the FusA lumen and enter the periplasm[14]. The mechanism by which ferredoxin traverses across the FusA lumen in this system remains unclear. I additionally hypothesize that the interaction between monomeric FusB and the plug domain bound to ferredoxin involves a further step energized by PMF produced by ExbBD complex to facilitate the pulling of both the plug domain and ferredoxin through the FusA lumen into the periplasm. Ferredoxin exposed in the periplasm, is then captured by the homodimeric FusB through a thermodynamically favored and spontaneous reaction. This allows the plug domain to re-enter the FusA lumen, thereby restoring FusA and FusB to their resting states. The binding of the dimeric FusB to ferredoxin induces the movement of $FusB_{flex}$, potentially facilitating its interaction with the homodimeric M16 protease FusC, thereby transferring ferredoxin from FusB to FusC. Ferredoxin is then proteolytically digested by FusC to extract iron for cell survival.

In summary, I have described the relationship between oligomerization and the biological functions of FusB, a TonB protein involved in the ferredoxin uptake system of *P. carotovorum,* with a focus on its interaction with the ferredoxin substrate during the uptake

process. The crystal structure of FusB:AtFd2 reveals that acidic ferredoxin occupies the basic groove of $FusB_{rig}$ mainly and induces fluctuation of the other FusB structure in the complex, resulting from extensive intermolecular interactions of ferredoxin with both FusB molecules. The enthalpy-driven complex formation of FusB and ferredoxin in solution is thermodynamically favored and simultaneous, facilitating the capture of ferredoxin by homodimeric FusB in the periplasmic space. The crystal structure of the FusB:AtFd2 complex, along with their complex formation in aqueous solution, provides insights into the structure-based translocation mechanism of intact ferredoxin during its import into the periplasmic space of susceptible cells, highlighting its interaction with homodimeric FusB in the ferredoxin uptake system. Collectively, the findings in this work shed light on the mechanism of ferredoxin binding to homodimeric FusB during its import into the periplasmic space of susceptible cells by parasitizing the ferredoxin uptake system in *Pectobacterium*.

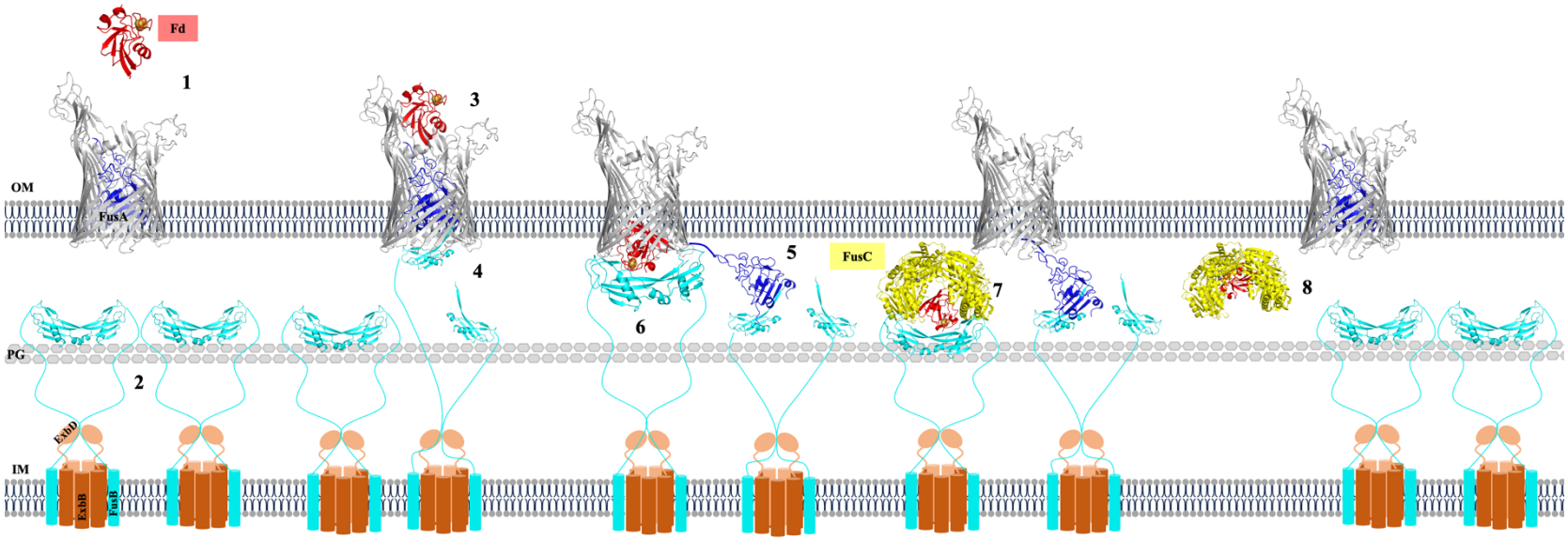

Figure 4.13 Proposed mechanism of ferredoxin uptake in *Pectobacterium*. In this model, in the resting state, (1) the lumen of FusA (grey) is filled by a plug domain (blue) to prevent nonspecific-substrate influx. (2) Dimeric FusB (cyan) complexed with ExbBD motor proteins (dark and light brown) interacts with peptidoglycan (PG) and TonB-independent receptors, allowing its localization near the periplasmic interface of the outer membrane bilayer. (3) The ferredoxin substrate (red) in the extracellular environment reaches its receptor FusA, (4) which induces the exposure of the TonB-box of the plug domain, allowing it to bind with the FusB monomer. (5) This binding of monomeric FusB to TonB-box energized by the PMF from the ExbB complex pulls the plug domain out from the FusA lumen and (6) also facilitates the translocation of ferredoxin through the FusA lumen into

periplasmic space, where ferredoxin can be captured by homodimeric FusB. (7) The structural fluctuation of dimeric FusB and ferredoxin complex facilitates the binding and transferring ferredoxin substrate to M16 protease FusC (yellow). (8) Then, the plug domain re-enters the FusA lumen, returning FusA and FusB to their resting states. Finally, ferredoxin is proteolytically digested by FusC to extract iron, which is then imported into the cell for survival.

Chapter 5

Conclusion

In iron-limiting conditions, *Pectobacterium* ssp., a phytopathogen, has evolved a specialized system known as the ferredoxin uptake system (Fus) to extract and import iron from imported ferredoxin of its host plants. This Fus system contains four proteins working together to import ferredoxin and extract iron for cellular use. In addition, *Pectobacterium* ssp. also produces pectocin M (PM) to outcompete closely related bacteria for the limiting nutrients in the environment. Possessing a plant-like ferredoxin domain, PM is able to translocate into susceptible cells by parasitizing FusA of the Fus system, with the assistance of FusB, to exert its lethal effect by degrading the peptidoglycan of closely related bacteria using its catalytic domain. As I introduced in Chapter 1, the uptake mechanisms of ferredoxin and PM through the Fus system in *Pectobacterium* ssp. remain unclear due to the lack of structural information and characterization of the binding profiles of these iron-containing proteins to Fus proteins. Consequently, in this thesis, I comprehensively addressed the purification, structural characterization, and mechanistic insights of key components involved in Fus system of *Pectobacterium* ssp. Specifically, I focused on the TonB-dependent receptor FusA and TonB-like FusB and their interactions with ferredoxins and PM1. The research encompasses three major chapters, Chapter 2, 3 and 4, each providing significant contributions to the better understanding of this complex biological system.

In chapter 2, to determine the atomic structures of FusA and its complexes with ferredoxins or PM, I successfully established a comprehensive method for purifying and characterizing FusA, essential for future structural and interaction studies by cryo-EM. Through several purification steps, I yielded highly pure monomeric FusA with secondary structure content matching the known FusA crystal structure. Negatively stained EM confirmed the homogeneity and high quality of purified FusA, but unfortunately cryo-EM analysis on FusA only achieved moderate resolution (~8.5 Å), insufficient for resolving finer structural details. Despite extensive efforts to improve resolution, challenges remained, underscoring the need for innovative approaches or complementary techniques in the future. In exploring FusA complexes with ferredoxins, I obtained unexpected results as no interactions between FusA and ferredoxins were detected. This suggests either a lack of affinity or the formation of a complex with lower affinity, which aligns with literature findings indicating that FusA interacts slowly with ferredoxins, often requiring longer times for productive complexes to be detectable. These findings challenge previous assumptions about FusA-ferredoxin interactions. However, I observed promising results in the productive complex formation of FusA:PM1 at DDM concentration lower than CMC, suggesting PM1 may somehow stabilize FusA folding. Preliminary cryo-EM analyses indicated potential PM1 presence in 2D classes of the FusA:PM1 complex, warranting further investigation to elucidate structural details under optimized conditions. Based on the complex formation and interaction of FusA and PM1 described in the literature, I confirmed the interaction between these proteins and identified new condition to stabilize and accelerate the formation of this productive complex.

PM1, possessing the ferredoxin domain, is another molecule capable of translocating into the target cell via FusA lumen in Fus system. While its biological function in inhibiting the growth of *Pectobacterium* ssp. has been extensively elucidated, the structure-based mechanism underlying its interactions with FusA and FusB remains unclear due to the lack of an atomic structure of PM1. In chapter 3, I focused on the structural determination of full-length PM1 and its interaction with FusA. The crystal structure of PM1 at 2.04 Å resolution revealed the unique closed conformation, which differs from that of the previously solved PM2 structures and provided a deeper understanding of the structural flexibility within pectocin M family. Combining structural information of PM1 and FusA with HADDOCK docking allows me to propose a more precise mechanism model for intact PM translocation through FusA lumen involving domain rearrangement and diverse binding modes of PM_{fd} to FusA, emphasizing the role of electrostatic surface properties in binding specificity. The findings in this work advanced the existing model of PM uptake through Fus system and also highlighted the structural differences and similarities compared with other ferredoxins and PM2.

After binding to the extracellular loops of FusA, both ferredoxin and PM require assistance from FusB along with the ExbB/ExbD complex, which provides PMF to energize the dislocation of the plug domain from the FusA barrel and the translocation of these proteins across the FusA lumen. However, the question of which oligomeric state of FusB is responsible for binding to ferredoxin and the ferredoxin domain of PM remains unclear due to limitation of structural and biochemical studies on FusB and ferredoxin complex.

Consequently, in Chapter 4, I examined the complex formations of FusB to AtFd2 and PM1 in solution. I found that FusB exhibits both dimeric and monomeric states in solution, with the dimeric form being capable of forming stable complexes with AtFd2 and PM1, unlike the monomeric form. I also successfully determine the crystal structure of FusB:AtFd2 complex that reveals extensive intermolecular contacts between dimeric FusB and AtFd2, involving hydrogen bonds and salt bridges crucial for complex stability. A structural comparison of FusB in its complexed and Fd-free forms suggested the flexibility of the dimer and the conformational changes of key residues on FusB upon AtFd2 binding. Based on these new findings, I strongly assert that the dimeric form of FusB plays a crucial role in binding to ferredoxin and PM during the translocation of these iron-containing proteins through FusA lumen in Fus system.The enthalpy-driven complex formations of FusB with ferredoxin and PM1 in solution are thermodynamically favored and occurs simultaneously. This binding characteristic potentially facilitates the capture of the ferredoxin domain by homodimeric FusB in the periplasmic space. Based on the new findings in Chapter 4, I have provided more insights into the structure-based translocation mechanism of intact ferredoxin during its import into the periplasmic space of susceptible cells, underlying its interaction with the homodimeric FusB in Fus system in *Pectobacterium* ssp.

Collectively, the currently available structural and biological information obtained in this thesis significantly advance the understanding of importing ferredoxin and PM through Fus system in *Pectobacterium* ssp. by providing detailed structural and mechanistic insights into the interactions of these iron-containing proteins to Fus proteins, FusA and FusB. The purification protocol and the structural determination established for FusA and its complexed

with PM1 lay a strong foundation for future research. The proposed mechanisms for PM and ferredoxin uptake in Fus system provide valuable frameworks for further investigation, offering deeper insights into their processes. Despite the challenges encountered in achieving high-resolution structures, the findings underscore the need for innovative approaches and complementary techniques to overcome these limitations. Future research should focus on optimizing conditions for complex formations, improving cryo-EM resolution, and exploring the dynamic interactions within Fus system. These efforts will contribute to a more comprehensive understanding of the molecular mechanisms underlying nutrient acquisition in Gram-negative bacteria. In addition, they have the potential to guide the development of novel antibacterial strategies aimed at combating infections caused by phytopathogens in crops and ornamental plants.

References

1. Charkowski, A. O. The soft rot Erwinia. in *Plant-Associated Bacteria* (ed. Gnanamanickam, S. S.) 423–505 (Springer Netherlands, Dordrecht, 2006).

2. Mansfield, J. *et al.* Top 10 plant pathogenic bacteria in molecular plant pathology. *Mol Plant Pathol* **13**, 614–629 (2012).

3. Nabhan, S., De Boer, S. H., Maiss, E. & Wydra, K. *Pectobacterium aroidearum* sp. nov., a soft rot pathogen with preference for monocotyledonous plants. *Int J Syst Evol Microbiol* **63**, 2520–2525 (2013).

4. Bell, K. S. *et al.* Genome sequence of the enterobacterial phytopathogen *Erwinia carotovora* subsp. atroseptica and characterization of virulence factors. *Proc Natl Acad Sci* **101**, 11105–11110 (2004).

5. Charkowski, A. O. The Changing Face of Bacterial Soft-Rot Diseases. *Annu Rev Phytopathol* **56**, 269–288 (2018).

6. Czajkowski, R., Pérombelon, M. C. M., van Veen, J. A. & van der Wolf, J. M. Control of blackleg and tuber soft rot of potato caused by *Pectobacterium* and *Dickeya* species: a review. *Plant Pathol* **60**, 999–1013 (2011).

7. Bhat, K. A. *et. al*. Current Status of Post Harvest Soft Rot in Vegetables: A Review. *Asian J Plant Sci* **9**, 200–208 (2010).

8. Davidsson, P. R., Kariola, T., Niemi, O. & Palva, T. Pathogenicity of and plant immunity to soft rot *pectobacteria*. *Front Plant Sci* **4**, (2013).

9. Pérombelon, M. C. M. Potato diseases caused by soft rot *erwinias*: an overview of pathogenesis. *Plant Pathol* **51**, 1–12 (2002).

10. Walters, D. R. & Bingham, I. J. Influence of nutrition on disease development caused by fungal pathogens: implications for plant disease control. *Annals of Applied Biology* **151**, 307–324 (2007).

11. Gill, E. D., Schaerer, S. & Dupuis, B. Factors impacting blackleg development caused by *Dickeya* spp. in the field. *Eur J Plant Pathol* **140**, 317–327 (2014).

12. Ishimaru, C. A. & Loper, J. E. High-affinity iron uptake systems present in *Erwinia carotovora* subsp. carotovora include the hydroxamate siderophore aerobactin. *J Bacteriol* **174**, 2993–3003 (1992).

13. Gorshkov, V. *et al.* The Knockout of Enterobactin-Related Gene in *Pectobacterium atrosepticum* Results in Reduced Stress Resistance and Virulence towards the Primed Plants. *Int J Mol Sci* **22**, (2021).

14. Grinter, R. *et al.* Structure of the bacterial plant-ferredoxin receptor FusA. *Nat Commun* **7**, (2016).

15. van der Wolf, J. M. *et al.* Management of Diseases Caused by *Pectobacterium* and *Dickeya* Species. in *Plant Diseases Caused by Dickeya and Pectobacterium Species* (eds. Van Gijsegem, F., van der Wolf, J. M. & Toth, I. K.) 175–214 (Springer International Publishing, Cham, 2021).

16. ELPHINSTONE, J. G. & PÉROMBELON, M. C. M. Control of contamination of potatoes with air-borne *Erwinia carotovora* by foliar application of copper oxychloride. *Annals of Applied Biology* **110**, 535–544 (1987).

17. Gracia-Garza, J. A., Allen, W., Blom, T. J. & Brown, W. Pre- and post-plant applications of copper-based compounds to control *Erwinia* soft rot of calla lilies. *Canadian Journal of Plant Pathology* **24**, 274–280 (2002).

18. Blom, T. J. & Brown, W. Preplant Copper-Based Compounds Reduce *Erwinia* Soft Rot on Calla Lilies. *Hort Tech*, **9(1)**, (1999).

19. Jones, A. L., Schnabel, E. & Vanneste, J. L. The development of streptomycin-resistant strains of *erwinia amylovora*. in *Fire blight: the disease and its causative agent, Erwinia amylovora.* 235–251 (CABI Publishing, UK, 2000).

20. Buttimer, C. *et al.* Bacteriophages and bacterial plant diseases. *Front Microbiol* **8**, (2017).

21. Grinter, R. *et al.* Structure of the atypical bacteriocin pectocin M2 implies a novel mechanism of protein uptake. *Mol Microbiol* **93**, 234–246 (2014).

22. Chérier, D. *et al.* Pectocin M1 (PcaM1) inhibits *Escherichia coli* cell growth and peptidoglycan biosynthesis through periplasmic expression. *Antibiotics* **5**, (2016).

23. Grinter, R., Milner, J. & Walker, D. Ferredoxin containing bacteriocins suggest a novel mechanism of iron uptake in *Pectobacterium* spp. *PLoS One* **7**, (2012).

24. Klebba, P. E. *et al.* Iron Acquisition Systems of Gram-negative Bacterial Pathogens Define TonB-Dependent Pathways to Novel Antibiotics. *Chem Rev* **121**, 5193–5239 (2021).

25. Mondal, J. & Bruce, B. D. Ferredoxin: the central hub connecting photosystem I to cellular metabolism. *Photosynthetica* **56**, 279–293 (2018).

26. Nzuza, N. *et al.* Diversification of Ferredoxins across Living Organisms. *Curr Issues Mol Biol* **43**, 1374–1390 (2021).

27. Tanaka, H. Toward Elucidation of the Photosynthetic Electron Transfer Mechanism. *J Physical Soc Japan* **91**, 091002 (2022).

28. Kameda, H., Hirabayashi, K., Wada, K. & Fukuyama, K. Mapping of Protein-Protein Interaction Sites in the Plant-Type [2Fe-2S] Ferredoxin. *PLoS One* **6**, (2011).

29. Hurley, J. K. *et al.* Structure–function relationships in *Anabaena* ferredoxin/ferredoxin:NADP+ reductase electron transfer: insights from site-directed mutagenesis, transient absorption spectroscopy and X-ray crystallography. *Biochim Biophys Acta - Bioenerg* **1554**, 5–21 (2002).

30. Kovalenko, I. B., Diakonova, A. N., Abaturova, A. M., Riznichenko, G. Y. & Rubin, A. B. Direct computer simulation of ferredoxin and FNR complex formation in solution. *Phys Biol* **7**, (2010).

31. HALL, D. O., CAMMACK, R. & RAO, K. K. Role for Ferredoxins in the Origin of Life and Biological Evolution. *Nature* **233**, 136–138 (1971).

32. Kurisu, G. *et al.* Structure of the electron transfer complex between ferredoxin and ferredoxin-NADP+ reductase. *Nat Struct Biol* **8**, 117–121 (2001).

33. Kim, J. Y., Nakayama, M., Toyota, H., Kurisu, G. & Hase, T. Structural and mutational studies of an electron transfer complex of maize sulfite reductase and ferredoxin. *J Biochem* **160**, 101–109 (2016).

34. Kinoshita, M. *et al.* Energetic basis on interactions between ferredoxin and ferredoxin NADP+ reductase at varying physiological conditions. *Biochem Biophys Res Commun* **482**, 909–915 (2017).

35. Kim, J. Y. *et al.* Non-covalent forces tune the electron transfer complex between ferredoxin and sulfite reductase to optimize enzymatic activity. *Biochem J* **473**, 3837–3854 (2016).

36. Mondal, J. & Bruce, B. D. Ferredoxin: the central hub connecting photosystem I to cellular metabolism. *Photosynthetica* **56**, 279–293 (2018).

37. Wojnowska, M. & Walker, D. Fusb energizes import across the outer membrane through direct interaction with its ferredoxin substrate. *mBio* **11**, 1–11 (2020).

38. Grinter, R. *et al.* FusC, a member of the M16 protease family acquired by bacteria for iron piracy against plants. *PLoS Biol* **16**, (2018).

39. Simons, A., Alhanout, K. & Duval, R. E. Bacteriocins, Antimicrobial Peptides from Bacterial Origin: Overview of Their Biology and Their Impact against Multidrug-Resistant Bacteria. *Microorganisms* **8**, (2020).

40. Mavridou, D. A. I., Gonzalez, D., Kim, W., West, S. A. & Foster, K. R. Bacteria Use Collective Behavior to Generate Diverse Combat Strategies. *Curr Biol* **28**, 345-355 (2018).

41. Granato, E. T. & Foster, K. R. The Evolution of Mass Cell Suicide in Bacterial Warfare. *Curr Biol* **30**, 2836-2843 (2020).

42. Chérier, D., Patin, D., Blanot, D., Touzé, T. & Barreteau, H. The Biology of Colicin M and Its Orthologs. *Antibiotics* **10**, (2021).

43. Barreteau, H. *et al.* Functional and structural characterization of PaeM, a colicin M-like bacteriocin produced by *Pseudomonas aeruginosa*. *J Biol Chem* **287**, 37395–37405 (2012).

44. Zeth, K., Römer, C., Patzer, S. I. & Braun, V. Crystal structure of colicin M, a novel phosphatase specifically imported by *Escherichia coli*. *J Biol Chem* **283**, 25324–25331 (2008).

45. Grinter, R., Roszak, A. W., Cogdell, R. J., Milner, J. J. & Walker, D. The crystal structure of the lipid II-degrading bacteriocin syringacin M suggests unexpected evolutionary relationships between colicin M-like bacteriocins. *J Biol Chem* **287**, 38876–38888 (2012).

46. Latino, L. *et al.* Impact of FiuA Outer Membrane Receptor Polymorphism on the Resistance of *Pseudomonas Aeruginosa* toward Peptidoglycan Lipid II-Targeting PaeM Pyocins. *J Bacteriol* **201(13)**, (2019).

47. Cascales, E. *et al.* Colicin Biology. *Microbiol Mol Biol Rev* **71**, 158–229 (2007).

48. Klebba, P. E. ROSET Model of TonB Action in Gram-Negative Bacterial Iron Acquisition. *J Bacteriol* **198**, 1013–1021 (2016).

49. Kaserer, W. A. *et al.* Insight from TonB Hybrid Proteins into the Mechanism of Iron Transport through the Outer Membrane. *J Bacteriol* **190**, 4001–4016 (2008).

50. Gresock, M. G., Kastead, K. A. & Postle, K. From Homodimer to Heterodimer and Back: Elucidating the TonB Energy Transduction Cycle. *J Bacteriol* **197**, 3433–3445 (2015).

51. Koedding, J. *et al.* Dimerization of TonB Is Not Essential for Its Binding to the Outer Membrane Siderophore Receptor FhuA of *Escherichia coli**. *J Biol Chem* **279**, 9978–9986 (2004).

52. Sauter, A., Howard, S. P. & Braun, V. In vivo evidence for TonB dimerization. *J Bacteriol* **185**, 5747–5754 (2003).

53. Josts, I., Veith, K. & Tidow, H. Ternary structure of the outer membrane transporter FoxA with resolved signalling domain provides insights into TonB-mediated siderophore uptake. *Elife* **8**, (2019).

54. Pawelek, P. D. *et al.* Structure of TonB in Complex with FhuA, E. coli Outer Membrane Receptor. *Science (1979)* **312**, 1399–1402 (2006).

55. Shultis, D. D., Purdy, M. D., Banchs, C. N. & Wiener, M. C. Outer Membrane Active Transport: Structure of the BtuB:TonB Complex. *Science (1979)* **312**, 1396–1399 (2006).

56. Oeemig, J. S., Ollila, O. H. S. & Iwaï, H. NMR structure of the C-terminal domain of TonB protein from *Pseudomonas aeruginosa*. *PeerJ* **6**, (2018).

57. White, P. *et al.* Exploitation of an iron transporter for bacterial protein antibiotic import. *Proc Natl Acad Sci* **114**, 12051–12056 (2017).

58. Zeth, K., Römer, C., Patzer, S. I. & Braun, V. Crystal structure of colicin M, a novel phosphatase specifically imported by *Escherichia coli*. *J Biol Chem* **283**, 25324–25331 (2008).

59. He, R. *et al.* Effect of Ferredoxin Receptor FusA on the Virulence Mechanism of *Pseudomonas plecoglossicida*. *Front Cell Infect Microbiol* **12**, (2022).

60. Kühlbrandt, W. The Resolution Revolution. *Science (1979)* **343**, 1443–1444 (2014).

61. Wu, M. & Lander, G. C. How low can we go? Structure determination of small biological complexes using single-particle cryo-EM. *Curr Opin Struct Biol* **64**, 9–16 (2020).

62. Studier, F. W. Protein production by auto-induction in high-density shaking cultures. *Protein Expr Purif* **41**, 207–234 (2005).

63. Fox, B. G. & Blommel, P. G. Autoinduction of Protein Expression. *Curr Protoc Protein Sci* **56**, (2009).

64. Kubota-Kawai, H. *et al.* X-ray structure of an asymmetrical trimeric ferredoxin–photosystem I complex. *Nat Plants* **4**, 218–224 (2018).

65. Zivanov, J. *et al*. New tools for automated high-resolution cryo-EM structure determination in RELION-3. *Elife* **7**, (2018)

66. Pettersen, E. F. *et al*. UCSF Chimera—A visualization system for exploratory research and analysis. *J Comput Chem* **25**, 1605–1612 (2004).

67. Zheng, S. Q. *et al*. MotionCor2: anisotropic correction of beam-induced motion for improved cryo-electron microscopy. *Nat Methods* **14**, 331–332 (2017).

68. Rohou, A. & Grigorieff, N. CTFFIND4: Fast and accurate defocus estimation from electron micrographs. *J Struct Biol* **192**, 216–221 (2015).

69. Bepler, T. *et al*. Positive-unlabeled convolutional neural networks for particle picking in cryo-electron micrographs. *Nat Methods* **16**, 1153–1160 (2019).

70. Micsonai, A. *et al.* Accurate secondary structure prediction and fold recognition for circular dichroism spectroscopy. *Proc Natl Acad Sci* **112**, 3095–3103 (2015).

71. Thompson, C. M. A. *The Biochemical and Biophysical Characterisation of Protein Antibiotics Targeting Pectobacterium ssp. and Streptococcus agalactiae*. PhD thesis, University of Glasgow. (2019).

72. Kabsch, W. XDS. *Acta Crystallogr D Biol Crystallogr* **66**, 125–132 (2010).

73. McCoy, A. J. *et al.* Phaser crystallographic software. *J Appl Crystallogr* **40**, 658–674 (2007).

74. Liebschner, D. *et al.* Macromolecular structure determination using X-rays, neutrons and electrons: Recent developments in Phenix. *Acta Crystallogr D Struct Biol* **75**, 861–877 (2019).

75. Terwilliger, T. C. *et al*. Iterative model building, structure refinement and density modification with the PHENIX AutoBuild wizard. *Acta Crystallogr D Biol Crystallogr* **64**, 61–69 (2008).

76. Emsley, P., Lohkamp, B., Scott, W. G. & Cowtan, K. Features and development of Coot. *Acta Crystallogr D Biol Crystallogr* **66**, 486–501 (2010).

77. Afonine, P. V. *et al.* Towards automated crystallographic structure refinement with phenix.refine. *Acta Crystallogr D Biol Crystallogr* **68**, 352–367 (2012).

78. Laskowski, R. A. & Swindells, M. B. LigPlot^{+}: Multiple ligand-protein interaction diagrams for drug discovery. *J Chem Inf Model* **51**, 2778–2786 (2011).

79. Hayward, S. & Berendsen, H. J. C. Systematic analysis of domain motions in proteins from conformational change: New results on citrate synthase and T4 lysozyme. *Proteins* **30**, 144–154 (1998).

80. De Vries, S. J., Van Dijk, M. & Bonvin, A. M. J. J. The HADDOCK web server for data-driven biomolecular docking. *Nat Protoc* **5**, 883–897 (2010).

81. Hall, D. O., Cammack, R. & Rao, K. K. The plant ferredoxins and their relationship to the evolution of ferredoxins from primitive life. *Pure Appl Chem* **34**, 553–578 (1973).

82. Bottin, H. & Lagoutte, B. Ferrodoxin and flavodoxin from the cyanobacterium *Synechocystis* sp PCC 6803. *Biochim Biophys Acta - Bioenerg* **1101**, 48–56 (1992).

83. Zheng, H., Chruszcz, M., Lasota, P., Lebioda, L. & Minor, W. Data mining of metal ion environments present in protein structures. *J Inorg Biochem* **102**, 1765–1776 (2008).

84. Grinter, R. W. *Discovering colicin and lectin-like bacteriocins for the creation of disease resistant transgenic plants.* PhD thesis, University of Glasgow. (2014).

85. Jurrus, E. *et al.* Improvements to the APBS biomolecular solvation software suite. Protein Science **27**, 112–128 (2018).

86. Schrödinger LLC. The PyMOL Molecular Graphics System, Version~1.8. (2015).

87. Agirre, J. *et al.* The CCP4 suite: integrative software for macromolecular crystallography. *Acta Crystallogr D Biol Crystallogr* **79**, 449–461 (2023).

88. Faraldo-Gómez, J. D. & Sansom, M. S. P. Acquisition of siderophores in gram-negative bacteria. *Nat Rev Mol Cell Biol* **4**, 105–116 (2003).

89. Andrews, S. *et al.* Control of Iron Metabolism in Bacteria. in *Metallomics and the Cell* (ed. Banci, L.) 203–239 (Springer Netherlands, Dordrecht, 2013).

90. Cornelis, P. & Dingemans, J. *Pseudomonas aeruginosa* adapts its iron uptake strategies in function of the type of infections. *Front Cell Infect Microbiol* **3**, (2013).

91. Krewulak, K. D. & Vogel, H. J. TonB or not TonB: is that the question? *Biochem Cell Biol* **89**, 87–97 (2011).

92. Schaible, U. E. & Kaufmann, S. H. E. Iron and microbial infection. *Nat Rev Microbiol* **2**, 946–953 (2004).

93. Noinaj, N. *et al.* Structural basis for iron piracy by pathogenic Neisseria. *Nature* **483**, 53–61 (2012).

94. Noinaj, N., Guillier, M., Barnard, T. J. & Buchanan, S. K. TonB-Dependent Transporters: Regulation, Structure, and Function. *Annu Rev Microbiol* **64**, 43–60 (2010).

95. Clabbers, M. T. B., Gruene, T., Parkhurst, J. M., Abrahams, J. P. & Waterman, D. G. Electron diffraction data processing with DIALS. *Acta Crystallogr D Biol Crystallogr* **74**, 506–518 (2018).

96. Cadieux, N. & Kadner, R. J. Site-directed disulfide bonding reveals an interaction site between energy-coupling protein TonB and BtuB, the outer membrane cobalamin transporter. *Proc Natl Acad Sci* **96**, 10673–10678 (1999).

97. Ködding, J. *et al.* Crystal Structure of a 92-Residue C-terminal Fragment of TonB from *Escherichia coli* Reveals Significant Conformational Changes Compared to Structures of Smaller TonB Fragments*. *J Biol Chem* **280**, 3022–3028 (2005).

98. Mosbahi, K., Wojnowska, M., Albalat, A. & Walker, D. Bacterial iron acquisition mediated by outer membrane translocation and cleavage of a host protein. *Proc Natl Acad Sci* **115**, 6840–6845 (2018).

99. Sean Peacock, R., Weljie, A. M., Peter Howard, S., Price, F. D. & Vogel, H. J. The Solution Structure of the C-terminal Domain of TonB and Interaction Studies with TonB Box Peptides. *J Mol Biol* **345**, 1185–1197 (2005).

100. Ollis, A. A., Manning, M., Held, K. G. & Postle, K. Cytoplasmic membrane protonmotive force energizes periplasmic interactions between ExbD and TonB. *Mol Microbiol* **73**, 466–481 (2009).

101. Zinke, M. *et al.* Ton motor conformational switch and peptidoglycan role in bacterial nutrient uptake. *Nat Commun* **15**, (2024).

List of Publications

Related publication

Jantarit, N., Tanaka, H., Lin, Y., Lee Y.-H, Kurisu, G. Crystal structure of pectocin M1 reveals diverse conformations and interactions during its initial step via the ferredoxin uptake system. *FEBS OpenBio*. 1-15 (2024).

Unrelated publication

Sanjaya, R. E., Puspaningsih, N. N. T., Rohman, A., Rahmasari, H., Illias, R. M., Jantarit, N., Fujiyama, K., Pratama, A., Khairunnisa, F. Production and diversity analysis of cellulases from *Anoxybacillus* genus. *Biodiversitas* **25**, (2024).